UNIVERSITY OF CALIFORNIA
Los Angeles

A Discrete Stochastic Method for Modeling Non-Conservative Plastic Dislocation Processe

A dissertation submitted in partial satisfaction of the
requirements for the degree Doctor of Philosophy
in Materials Science and Engineering

by

Cameron McElfresh

2022

ABSTRACT OF THE DISSERTATION

A Discrete Stochastic Method for Modeling Non-Conservative Plastic Dislocation Processes

by

Cameron McElfresh
Doctor of Philosophy in Materials Science and Engineering
University of California, Los Angeles, 2022
Professor Jaime Marian, Chair

Non-conservative processes play a fundamental role in plasticity and are behind important macroscopic phenomena such as creep, dynamic strain aging, loop raft formation, etc. In the most general case, vacancy-induced dislocation climb is the operating unit mechanism. While dislocation/vacancy interactions have been modeled in the literature using a variety of methods, the approaches developed rely on continuum descriptions of both the vacancy population and its fluxes. However, there are numerous situations in physics where point defect populations display heterogeneous concentrations and/or non-smooth kinetics. With this in mind, in this work we present a kinetic Monte Carlo model that discretely captures vacancy generation and transport kinetics acting in conjunction with the evolving elastic fields provided by discrete dislocation dynamics simulations. The two models are coupled via the applied stresses and stress gradients generated by dislocation structures at vacancy locations. To extend the coupled model to the treatment of large systems, we cast the entire elasto-plastic-diffusive problem within a single stochastic framework, taking advantage of a parallel kMC algorithm to evolve the system as a single event-driven process. After introducing the numerical procedure and validation, we compare the method to existing continuum formulations and examine several macroscopic phenomena including non-conservative plastic bypass of a precipitate, dipole coalescence, and vacancy trap formation.

The dissertation of Cameron McElfresh is approved.

Xiaochun Li

Jenn-Ming Yang

Yinmin Wang

Jaime Marian, Committee Chair

University of California, Los Angeles

2022

TABLE OF CONTENTS

LIST OF FIGURES

LIST OF TABLES

ACKNOWLEDGEMENTS

Thank you to my parents (Steve and Jeanne), family (Duncan, Ian, Hilary, and Leia), and girlfriend (Danielle) for the unwavering support throughout my academic career.

Thank you to the IDRE staff, Google, and stackoverflow for technical advice and along the way.

VITA

2017	B. S. in Nanoengineering, University of California, San Diego
2018	M. S. in Nanoengineering, University of California, San Diego

PUBLICATIONS

McElfresh, C., Bertin, N., Aubrey, S., Marian, J. (2022). "Dislocation Loop Vacancy Decoration and Coalescence Using a Discretized kinetic Monte Carlo Dislocation Dynamics Method". (*in revisions*).

McElfresh, C., Bertin, N., Aubrey, S., Marian, J. (2022). "A massively-parallel coupled dislocation dynamics and kinetic Monte Carlo method to study dislocation climb induced processes". *Computational Materials Science*, 209, 111332.

McElfresh, C., Cui, Y., Dudarev, S. L., Po, G., Marian, J. (2021). "Discrete stochastic model of point defect-dislocation interaction for simulating dislocation climb". *International Journal of Plasticity*, 136, 102848.

McElfresh, C., Roberts, C., He, S., Prikhodko, S., Marian, J. (2022). "Using machine-learning to understand complex microstructural effects on the mechanical behavior of Ti-6Al-4V alloys". *Computational Materials Science*, 208, 111267.

McElfresh, C., Marian, J. (2022). Fracture mechanics of tungsten disks subjected to extreme cyclic loading. (*To be determined*).

McElfresh, C.,Ghazari, A.,Ghoniem, N., Marian, J. (2022). Polycrystal plasticity-driven static recrystallization model in iron. (*To be determined*).

Ghazari, A., McElfresh, C., Dickstein, D., Nadvornick, W., Pintsuk, G., Wessel, E., ... Ghoniem, N. (2022). "Intense cyclic heating effects on thermo-fracture and thermal shock of solid tungsten and open-cell tungsten foam". *Journal of Nuclear Materials*, 565, 153730.

Ghazari, A., McElfresh, C., Dickstein, D., Marian, J., Ghoniem, N. (2021). "Effects of cyclic plasma heating on surface damage of micro-porous tungsten". *Physica Scripta*, 96(12), 124033.

Chapter 1

Introduction

Non-conservative dislocation motion is responsible for important processes in plasticity such as climb, jog-dragging, the closing of cross-kinks, among others, with significant implications for mechanical behavior such as e.g. hardening, creep, dynamic strain aging, or swelling in irradiated materials [5–13]. Generally speaking, non-conservative motion refers to a point defect-assisted process that allows a dislocation segment to leave its glide plane in the direction of its normal. This normal $\boldsymbol{n}$ is uniquely defined as $\boldsymbol{n} \equiv \boldsymbol{s} \times \boldsymbol{t}$, where $\boldsymbol{s} = \boldsymbol{b}/b$ is the slip direction ($\boldsymbol{b}$ is the Burgers vector and $b = \|\boldsymbol{b}\|$) and $\boldsymbol{t}$ is the local tangent vector defining the local direction of the dislocation line. The necessity of point defect intervention makes processes like climb only feasible either at high temperatures (via vacancies, when their thermal concentration and/or emission rate is sufficiently high), or under far-from-equilibrium conditions as for example when irradiation is involved [9, 14–16].

For a dislocation segment to undergo climb, net defect fluxes must establish themselves, implying the presence of local sub or supersaturation. In its most common manifestation, stress fields produce the concentration gradients that lead to non-conservative dislocation climb. Also, dislocations are strong sinks in situations of supersaturated vacancy concentrations [14, 17, 18], so that climb can be regarded as a process that acts to reconstitute thermal equilibrium. Due to its non-conservative nature, dislocation climb is a process by which dislocations can produce volumetric and dimensional changes in addition to slip.

Due to its intrinsically atomistic nature, studies of climb processes have been at-

tempted by direct molecular dynamics (MD) simulations (e.g. [19]) and/or lattice-based kinetic Monte Carlo (kMC) [20,21]. However, apart from exceptionally rare situations, vacancy transport at the lattice level is far too slow to be accessible to atomistic simulations in a statistically meaningful manner. Instead, mean-field continuum models, based on the adiabatic approximation, have been the preferred choice in terms of theoretical implementations of climb processes in crystal plasticity and/or dislocation dynamics models. Within these, the more popular approach has been to superimpose a chemical force on the standard elastic forces due to external and internal stresses [1,22–27]. This force is obtained by matching the work done when a dislocation segment climbs a certain distance with the free energy required to create the vacancies needed to climb that same distance. An alternative approach is to formulate the climb velocity directly from the vacancy transport equations in the presence of dislocations [28–32].

Implementations of climb in discrete dislocation dynamics (DDD) simulations by way of suitable modifications to dislocation mobilities [33, 34] have been applied successfully in many scenarios [1,29,30,32,35,36]. Several drag-based climb approaches for DDD simulations have been developed and employed in the recent years. Dislocation climb was coupled with bulk vacancy diffusion in a simplified two-dimensional (2D) DDD investigation by Keralavarma *et al.* [29]. Rajaguru *et al.* developed a 2D DDD model that considered both the simplified analytical solution for the climb velocity of an infinite edge dislocation and a pipe-diffusion contribution [31]. Ghoniem *et al.* developed a thermodynamically-consistent method for interacting three-dimensional (3D) dislocation loops in which climb was further facilitated via a point defect absorption contribution [37]. Bako *et al.* proposed an expression for a segment's climb velocity that incorporated the local vacancy concentration as the governing factor [1]. This approach has been used to study the coarsening of vacancy loops in aluminum with respect to time and vacancy saturation. Mordahei *et al.* implemented dislocation climb by bulk diffusion in aluminum by solving for the local vacancy flux [25] and has since applied the approach to study loop coarsening and annihilation in irradiated microstructures [38–40]. Recently, Gu *et al.* demonstrated a Green's function formulation for climb with a

simplified numerical discretization for application in 3D DDD [26]. Gao *et al.* introduced a climb approach using 3D DDD for a nickel-based superalloy with a modified "local" and "mesoscale" vacancy concentrations to simulate γ-phase channels [41]. Niu *et al.* developed a method to solve for the vacancy-driven low-temperature climb velocity of curved dislocation segments in 3D DDD using a Robin boundary condition [42] and demonstrated its good agreement with experiments and atomistic simulations [43]. Liu *et al.* introduced a model for core-diffusion-based climb of curved dislocation segments in 3D DDD using a variational principle [44] and demonstrated the ability to accelerate it using a finite element discretisation method [45]. Breidi *et al.* implemented a 3D DDD method for climb of arbitrarily shaped dislocation segments that considers bulk diffusion using a Green's function formulation and the self-climb using the solution for a pure prismatic loop [46].

These approaches are all formulated at the continuum level, which – while thermodynamically consistent and numerically efficient – disregard local fluctuations in stress and defect concentrations. These fluctuations are especially important under heterogeneous conditions, when spatially-complex dislocation structures and/or defect distributions (e.g. as during irradiation [47, 48]) exist. Since vacancies are discrete particles, they are highly sensitive to these local variations of stress and presence of other defects. Thus, understanding how they evolve, taking into account such fluctuations, and studying how sensitive climb processes are to spatial heterogeneities is of relevance in many cases.

Therefore, the objective of this work is to develop an efficient method to discretely simulate non-conservative creep processes. The document is divided into sections that align with major bodies of work - followed by brief closing statements on future extensions of the framework. In Chapter 2 we develop the underlying theory for superimposing a kMC module tasked with simulating vacancy diffusion onto a microstructural simulator based on DDD. The DDD module is tasked with updating dislocation structure morphology and stress fields. As such, the kinetic module and the DDD simulator are coupled together by the underlying stress fields in the simulation volume. We apply the model to the simple case of a single edge

dislocation to study effective climb rates as a function of temperature and vacancy concentration for isolated dislocations, as well as to study a dislocation overcoming a precipitate lock via climb.

In Chapter 3 we implement the kMC/DDD model in a massively-parallel computing framework to enable large-scale simulations of the types of processes discussed above. First, we develop and implement modifications to parallelize the kMC/DDD model, by recasting the elasto-plastic-diffusive problem within a single stochastic framework. The new approach results in an efficient and scalable discrete model amenable to perform large-scale simulations, e.g. for simulating loop raft formation during recovery of damaged metals. Second, this new implementation is used and its predictions compared to three existing DDD vacancy-coupled climb methods, namely, (i) climb via balancing vacancy flux [25,49], (ii) Green's function formulation for climb [26], and (iii) discretized diffusion transport climb [50].

In Chapter 4, we employ the developed model to study dislocation loop coalescence in bcc Mo that requires a collaborative climb/glide response. Additionally, we examine the interaction of vacancies and prismatic loops and discuss the formation of vacancy traps and rings around the perimeter of the loops that affect how coalescence takes place. We then show excellent agreement with *in situ* experimental observations of loop coalescence under irradiation.

In Chapter 5 we briefly discuss extensions to the developed DDD/kMC model and highlight physical phenomena that could be cast in the same (or similar) discretized elasto-plastic framework.

Chapter 2

Discrete Stochastic Vacancy Model

2.1 Underlying theory

2.1.1 Kinetic model for point defect diffusion

According to transition state theory [51, 52], the diffusion coefficient for vacancies hopping in an isotropic medium follows an Arrhenius expression of the following type:

$$D(T) = zfb^2\nu(T) \tag{2.1}$$

where z is the coordination number of the lattice in question ($z = 8$ for bcc crystals), f is a correlation factor, b is the crystallographic jump distance ($b = a_0\sqrt{3}/2$ for bcc crystals, a_0 is the lattice parameter) and $\nu(T)$ is the temperature dependent jump frequency of the form

$$\nu(T) = \nu_0 \exp\left(-\frac{\Delta H_m}{kT}\right) \tag{2.2}$$

where ν_0 is an attempt frequency, k is Boltzmann's constant, and ΔH_m is the vacancy migration enthalpy. In the low-stress limit, ΔH_m depends on stress $\boldsymbol{\sigma}$ via a mechanical work coupling:

$$\Delta H_m(\boldsymbol{\sigma}) = \Delta E_m^0 - \boldsymbol{\sigma} : \boldsymbol{\Omega}_{\text{act}}$$

where ΔE_m^0 is the migration energy of a vacancy in a solid subjected to no stress, and $\boldsymbol{\Omega}_{\text{act}}$ is the activation volume tensor defined as the difference between the relaxation volume tensors at the saddle point and at an equilibrium position. Parameters ν_0, ΔE_m^0, and $\boldsymbol{\Omega}_{\text{act}}$ are routinely computed using first principles methods [53].

Another, and often more significant, effect of stress on the diffusion of defects results from the fact that the enthalpy of formation of a defect at an equilibrium position in the lattice depends on the local stress through:

$$H_f(\boldsymbol{\sigma}) = E_f^0 - \boldsymbol{\sigma} : \boldsymbol{\Omega}_f \tag{2.3}$$

where E_f^0 is the defect formation energy and $\boldsymbol{\Omega}_f$ is the formation volume tensor [53, 54]. It must be noted, however, that in most cases it is the relaxation, and not the formation, volume of a defect that enters the equations of elasticity, since it is the relaxation of the lattice around a defect that determines its elastic interaction with other defects and dislocations. As such, the relaxation volume tensor provides a tensorial measure of global deformation of the material due to the presence of a defect in it [55].

The relaxation and formation volume tensors, $\boldsymbol{\Omega}$ and $\boldsymbol{\Omega}_f$, are related to one another via $\boldsymbol{\Omega}_f = \pm\frac{1}{3}\Omega_a \boldsymbol{I} + \boldsymbol{\Omega}$, where Ω_a is the atomic volume, and the sign of Ω_a depends on the nature of the defect, vacancy $(+)$ or self-interstitial $(-)$ [56]. For vacancies, the first term in the above relation is positive, since in order to form an individual vacancy in the bulk of the crystal, it is necessary to deposit an atom onto its surface, hence increasing the total volume of the material by one atomic volume Ω_a. Conversely, the formation of a self-interstitial atom involves punching a surface atom into the bulk of the material, hence reducing the apparent total volume by Ω_a[1]. The second term, $\boldsymbol{\Omega}$, entering the formula for $\boldsymbol{\Omega}_f$, is the relaxation volume tensor [53, 54], describing the lattice relaxation effects. Elements of the relaxation volume tensor of a point defect can be readily evaluated using first-principles calculations [53, 54].

Note that in the context of studies of radiation damage, the *formation* volumes of defects rarely enter the equations for the experimentally observed quantities. That is because, under irradiation, vacancies and self-interstitial defects are formed

[1] See for example Figure 14.10 from [57]

in pairs, and this results in the cancellation of terms $\pm\frac{1}{3}\Omega_a \boldsymbol{I}$ in the definition [53] of the formation volume tensor $\boldsymbol{\Omega}_f$ above. Also, one should recognize the difference between the volumetric swelling of a material, which is a quantity given by the sum of formation volumes of all the defects, and lattice strain, measured for example by X-ray diffraction. Lattice strain is a measure of relaxation of the lattice, and it therefore depends on the *relaxation* volumes of defects, as illustrated for example by the observed negative lattice strain resulting from the accumulation of vacancies in metals [58].

The trace of the relaxation volume tensor $\mathrm{Tr}\,(\boldsymbol{\Omega}) = \Omega_{kk} = \Omega_{11} + \Omega_{22} + \Omega_{33}$ gives the total relaxation volume of a defect Ω_{rel}, which, depending on its sign (negative or positive), provides a measure of the total elastic contraction or expansion of the lattice due to the presence of the defect in the material [59]. For a vacancy, the relaxation volume tensor is isotropic [59], namely $\Omega_{ij} = \frac{1}{3}\delta_{ij}\Omega_{\mathrm{rel}}$, where δ_{ij} is Kronecker's delta. Since the trace of the identity tensor $\mathrm{Tr}(\boldsymbol{I}) = \delta_{kk} = \delta_{11} + \delta_{22} + \delta_{33} = 3$, we find $\mathrm{Tr}(\boldsymbol{\Omega}) = \frac{1}{3}\Omega_{\mathrm{rel}}\mathrm{Tr}(\boldsymbol{I}) = \Omega_{\mathrm{rel}}$. In terms of atomic volume, we can express the relaxation volume tensor as [53, 54]:

$$\boldsymbol{\Omega} = \Omega_a \boldsymbol{\varepsilon}_v \tag{2.4}$$

where $\boldsymbol{\varepsilon}_v$ is a diagonal strain tensor with identical components $\varepsilon_v = (\boldsymbol{\varepsilon}_v)_{11} = (\boldsymbol{\varepsilon}_v)_{22} = (\boldsymbol{\varepsilon}_v)_{33}$ equal to:

$$\varepsilon_v = \frac{\Omega_{\mathrm{rel}}}{3\Omega_a} = \frac{\theta_v}{3}$$

with θ_v being the relative local lattice contraction around a vacancy (typically around -20% [53, 54]). With this, assuming that the relaxation volume of a defect is isotropic, eq. (2.3) becomes:

$$H_f = E_f^0 - \frac{1}{3}\sigma_{ij}\delta_{ij}\left(\Omega_{\mathrm{rel}} \pm \Omega_a\right) = E_f^0 - \sigma_{jj}\left(\Omega_{\mathrm{rel}} \pm \Omega_a\right) = E_f^0 + p\left(\Omega_{\mathrm{rel}} \pm \Omega_a\right) \tag{2.5}$$

where, as above, '+' refers to vacancies and '−' to self-interstitials, and $p = -\frac{1}{3}\mathrm{Tr}\,(\boldsymbol{\sigma}) = -\frac{1}{3}\sigma_{kk} = -\frac{1}{3}(\sigma_{11} + \sigma_{22} + \sigma_{33})$ is the hydrostatic pressure [60]. Note that in the above equations we use the Einstein convention where repeated indeces imply summation. The energy of a defect at an equilibrium position in the lattice depends on the stress as follows [61, 62]:

$$E = E^0 - \frac{1}{3}\sigma_{ij}\delta_{ij}\Omega_{\mathrm{rel}} = E^0 - \frac{1}{3}\sigma_{kk}\Omega_{\mathrm{rel}} = E^0 + p\Omega_{\mathrm{rel}}. \tag{2.6}$$

In the approximation where both the relaxation and activation volume tensors of a defect are assumed to be isotropic, the diffusion tensor is also isotropic [62, 63]. This justifies the drift-diffusion equation approach developed below.

2.1.2 The drift-diffusion equation

Vacancy transport is governed by the so-called the drift-diffusion (or advection-diffusion) equation:

$$\frac{\partial C}{\partial t} = D\nabla^2 C - \boldsymbol{u} \cdot \nabla C \tag{2.7}$$

where C is the defect concentration, $\boldsymbol{u}$ is the average drift velocity (a three-dimensional vector), ∇ is the gradient operator, D is the diffusion coefficient, and ∇^2 is the Laplacian. The first term on the right-hand side of eq. (2.7) represents drift due to the bias in the probability of moving in a preferred direction and the second term describes ordinary isotropic three-dimensional diffusion. For walkers centered at the origin, the above equation has the following solution in one dimension [64, 65]

$$C(\boldsymbol{x}, t) = \frac{1}{(4\pi D t)^{1/2}} \exp\left\{-\frac{(\boldsymbol{x} - \boldsymbol{u}t)^2}{4Dt}\right\} \tag{2.8}$$

where t is the time and $\boldsymbol{x}$ is the position vector. Useful time-dependent statistics of this process are the mean location $m(\boldsymbol{X}_t)$ (first moment of the $C(\boldsymbol{x}, t)$ distribution) and the mean squared displacement (MSD) $m(R_t^2)$ (second moment, with $R_t = |\boldsymbol{X}_t|$), defined as:

$$m(\boldsymbol{X}_t) = \int \boldsymbol{x} C(\boldsymbol{x}, t) d\boldsymbol{x} \tag{2.9}$$

$$m(R_t^2) = \int |\boldsymbol{x}|^2 C(\boldsymbol{x}, t) d\boldsymbol{x} \tag{2.10}$$

The solutions to the above integrals are $m(\boldsymbol{X}_t) = \boldsymbol{u}t$ and:

$$m(R_t^2) = \boldsymbol{u}^2 t^2 + 6Dt$$

That is, the effect of the drift compared to a simple random walk process is to shift the center of the Gaussian distribution from $x = 0$ to $x = ut$ and to make the MSD depend quadratically on time (for long times) instead of linearly.

The drift term can be obtained by mapping eq. (2.7) to the general form of the diffusion equation for isotropic cubic crystals [63]:

$$\frac{\partial C(\boldsymbol{x},t)}{\partial t} = \nabla \cdot \left[D \left(\nabla C(\boldsymbol{x},t) + \frac{C(\boldsymbol{x},t)}{kT} \nabla E(\boldsymbol{x}) \right) \right] \tag{2.11}$$

where the energy gradient term reflects the variation of the energy of defects at equilibrium lattice sites. Equation (2.11) is encountered in the treatment of diffusion of particles in a potential energy field $E(\boldsymbol{x})$, where the right-hand side of the equation equals the divergence of the defect flux. Comparing the second terms in the r.h.s. of eqs. (2.7) and (2.11) gives the expression for the drift velocity $\boldsymbol{u}$ is:

$$\boldsymbol{u} = -\frac{D}{kT} \nabla E(\boldsymbol{x}) \tag{2.12}$$

Inserting eq. (2.6) into the above expression results in the drift velocity being proportional to the gradient of the pressure:

$$\boldsymbol{u} = \frac{D\Omega_{\text{rel}}}{3kT} \nabla \text{Tr}\left(\boldsymbol{\sigma}(\boldsymbol{x})\right) = -\frac{D\Omega_{\text{rel}}}{kT} \nabla p(\boldsymbol{x}) \tag{2.13}$$

In the above expression, we have neglected the variation of the diffusion coefficient with spatial coordinates. This variation is associated with the change of shape of the strain field of a vacancy during its transition across a saddle point [53], and it adds an extra term, quadratic in stress, to the right-hand side of eq. (2.13). We have also neglected the dependence of the relaxation volume on stress, and retained only the term linear in elastic field (see [66]). With this, equation (2.13) can be expressed in explicit Cartesian form as:

$$u_i = \frac{D\Omega_{\text{rel}}}{3kT} \frac{\partial \sigma_{kk}}{\partial x_i}, \tag{2.14}$$

where $\sigma_{kk} \equiv \text{Tr}\left(\boldsymbol{\sigma}\right)$.

It is important to note that eq. (2.13) is strictly valid only when $\boldsymbol{u}$ is independent of the vacancy location, which is not the case here. However, as we demonstrate in the Section B.1, the exact solution of eq. (2.7) (i.e., with spatially-dependent $\boldsymbol{u}$) can be satisfactorily approximated by eq. (2.13) within the timescales of vacancy diffusion, thus justifying its use throughout the rest of the paper.

2.1.3 Vacancy production/elimination mechanisms

Vacancy absorption

Once a vacancy or a number of vacancies N_i reaches a given dislocation segment i of length ℓ_i, the following volume balance can be written:

$$N_i \Omega_a = \ell_i h_i \left(\boldsymbol{t}_i \times \boldsymbol{b}_i \right) \cdot \boldsymbol{n}_i$$

where h_i is the climb distance along the normal direction $\boldsymbol{n}_i$, $\boldsymbol{b}_i$ and $b_i = |\boldsymbol{b}|$ are the Burgers vector and its modulus, and $\boldsymbol{t}_i$ is the segment direction. This results in a climb jump of magnitude:

$$h_i = \frac{N_i \Omega_a b_i}{\ell_i \left| \boldsymbol{t}_i \times \boldsymbol{b}_i \right|^2} \tag{2.15}$$

where we have used that $\boldsymbol{n} = (\boldsymbol{t} \times \boldsymbol{b})/b$. Note that h_i is undefined for screw dislocations, as is commonly the case in this type of models [1, 23].

Thermal vacancy emission

After Friedel [67], the rate of emission of vacancies from dislocations can be written as:

$$\dot{C} = q\nu(T) \left(1 - \frac{C}{C_0} \right) \tag{2.16}$$

where q is a geometric factor, $\nu(T)$ is the vacancy jump rate (refer to eq (2.2)), and $C_0 = \exp\left(-\frac{H_f}{kT}\right)$ is the equilibrium vacancy concentration (H_f is the vacancy formation enthalpy, eq. (2.5)).

Expression (2.16) is nonlocal, i.e., it is enforced in a global sense (as defined by C_0). However, vacancy emission from a dislocation segment is highly local in that it is strongly influenced by the local stress and vacancy concentration. Consequently, the above equation can be adapted to give the local emission from a given dislocation segment of length ℓ surrounded by a number of vacancies N in a volume around the segment. Further, here we take the approach that the emission rate is zero for purely screw segments and maximum for pure edge segments. With

this, we can write:

$$\dot{N}_i = \left(\frac{2\pi\ell_i}{b_i}\left(1 - \frac{\boldsymbol{t}_i \cdot \boldsymbol{b}_i}{b_i}\right)\right)\nu(T)\left(1 - \frac{N_i}{\rho_a V_i \exp\left(-\frac{H_f}{kT}\right)}\right) \tag{2.17}$$

where N_i is the number of vacancies contained in a volume $V_i = \pi R^2 \ell_i$ around dislocation segment i. The stress $\boldsymbol{\sigma}$ in this volume is taken to be the local stress (from sources other than the self-stress) at the dislocation segment's location, $\boldsymbol{r}_i$. In principle, R is arbitrary but it should be sufficiently small for this approximation to be valid. Note that in most cases, this will result in zero vacancies in this volume, meaning that the rate of insertion will generally be positive[2]. To avoid repeated emission/reabsorption cycles, we place the emitted vacancies at a random location within the simulation box while displacing the dislocation segment along the negative sense of $\boldsymbol{n}_i$ by an amount consistent with the emitted volume of vacancies (eq. (2.15)).

Instead of eq. (2.16), a more consistent expression of the vacancy emission rate needed to maintain a global vacancy concentration is obtained by integrating eq. (2.17) over the entire simulation volume V[3]:

$$\dot{C}_v = \frac{2\pi V \rho_d}{b}\nu(T)\left(1 - \frac{C_v}{\exp\left(-\frac{H_f(\boldsymbol{\sigma}_{\text{ext}})}{kT}\right)}\right) \tag{2.18}$$

where ρ_d is the total dislocation density and C_v is the global vacancy concentration. Once a vacancy is emitted using this expression a random segment is selected and displaced by one climb distance h. Emission-dominated conditions lead to 'downward' climb, i.e. along the direction of the tensile region of the stress field of an edge dislocation, while absorption dominated climb takes place 'upwards', or towards the compressive semi-plane.

[2]To introduce a stochastic variability in the insertion rate (accepting cases where the vacancy concentration might be higher than the equilibrium concentration, or rejecting cases where the vacancy concentration might be lower than the equilibrium concentration), the second '1' in eq. (2.17) is replaced with a Gaussian defined by $N(1, kT/E_f^0)$.

[3]Summation of all segments over V yields: $\sum_i \ell_i = \rho_d V$

2.1.4 Connection to elasticity and climb mobilities

The climb velocity of a given segment $\boldsymbol{v}_c^i$ points along the direction of $\boldsymbol{n}_i$ and is connected to the climb forces as:

$$\begin{aligned} \boldsymbol{v}_c^i &= v_c^i \, \boldsymbol{n}_i \\ v_c^i &= M_c \left(f_i^{\text{el}} + f_i^{\text{os}} \right) \end{aligned} \tag{2.19}$$

where $M_c \equiv M_c(T, p, C_v)$ is a scalar-valued function representing the climb *mobility*, $f_i^{\text{el}} = [(\boldsymbol{\sigma}_i \cdot \boldsymbol{b}_i) \times \boldsymbol{t}_i] \, \boldsymbol{n}_i$ is the climb contribution of the Peach-Koehler force, while f_i^{os} is the chemical force, often referred to as 'osmotic' force, which in linearized form can be expressed as [1, 25]:

$$f^{\text{os}} = \frac{bkT}{\Omega_a} \left(1 - \frac{C_0}{C_v} \right) \tag{2.20}$$

We will use these expressions to reconcile the results obtained in Section 2.2.3 with the elastic formulation of DDD.

2.1.5 Material parameters

We use bcc Fe as our model system in this work. Point defects in iron have been extensively studied experimentally and computationally over the past several decades and a very accurate numerical database exists from which to get the parameters used here [53, 54, 68–76]. They are given in Table 2.1.

Table 2.1: Material parameters for bcc Fe employed in this work.

Parameter	Symbol	Value	Units
Boltzmann's constant	k	8.615×10^{-5}	$\text{eV}\cdot\text{K}^{-1}$
Correlation factor	f	0.78	-
Burgers vector's modulus	b	0.25	nm
Attempt frequency	ν_0	10^{12}	Hz
Vacancy migration energy	ΔE_m^0	0.60	eV
Atomic volume	Ω_a	0.77	b^3
Vacancy relaxation volume	Ω_{rel}	θ_v	Ω_a
Vacancy formation volume	Ω_f	$1 + \theta_v$	Ω_a
Vacancy volumetric strain	θ_v	-0.2	-
Vacancy formation energy	E_f^0	1.7	eV
Capture radius	R	2.0	b

2.2 Results

Next we apply the method described in the previous section to the calculation of climb velocities for edge dislocations in Fe. The solution procedure and the numerical details of the simulations are discussed in depth in B.2. First we carry out a set of self-consistency verification checks to ensure the correctness of the model, followed by production runs to calculate climb velocities as a function of temperature, pressure, and global vacancy concentration.

2.2.1 Self-consistency checks

We begin by testing the evolution of the mean square displacement, $\langle r^2 \rangle$, of vacancies diffusing in an isotropic medium versus vacancies moving in the stress field near the core of an edge dislocation. The results for 200 independent tests (one single vacancy placed at random in a 2D square box) are shown in Figure 2.1 with error bars. The evolution of $\langle r^2 \rangle$ in each case displays the expected dependence with time described in Sec. 2.1.2. The diffusivity used was 1.0×10^{-9} m^2·s^{-1} ($\sim$300 K in Fe), which correlates well with the values of 8.6×10^{-10} and 1.3×10^{-9} m^2·s^{-1} displayed in Fig. 2.1 for biased and unbiased diffusion, respectively.

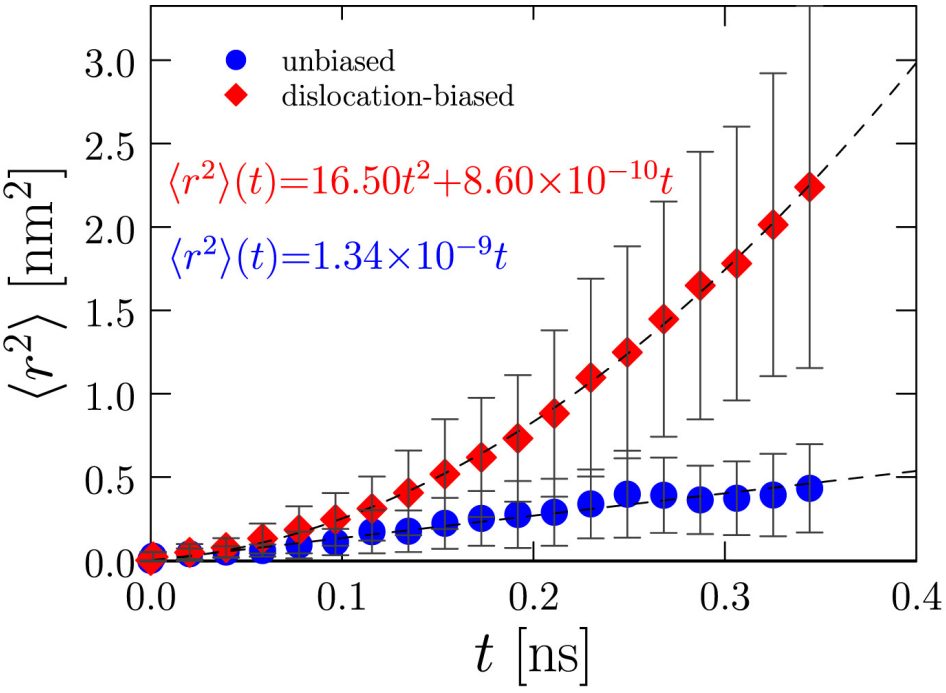

Figure 2.1: Time evolution of the mean square displacement, $\langle r^2\rangle$, of vacancies diffusing in an isotropic medium undergoing an *unbiased* random walk (blue circles) and for vacancies moving in the stress field of an edge dislocation (*biased* random walk, red diamonds). Linear and quadratic least-squares fits are shown for each case. The vacancy diffusivity employed corresponds to a temperature of 300 K. The error bars originate from five independent stochastic runs.

While tracking the evolution of $\langle r^2\rangle$ is useful to verify the solution of eq. (2.7), the mean square displacement is an integrated measure that does not give information about the trajectories of migrating vacancies. To check whether vacancy trajectories are consistent with the drift velocity derived in Sec. 2.1.2, we plot in Figure 2.2 the generic trajectories of vacancies against the backdrop of the (isotropic elastic) stress field of an edge dislocation (shown as a color contour plot) and vector (2.14). The figure contains results for the σ_{xx} and σ_{yy} components of the stress, as well as for the $\frac{\partial\sigma_{kk}}{\partial x}$ and $\frac{\partial\sigma_{kk}}{\partial y}$ components of (2.14) (Figs. 2.2(a) and 2.2(b)). The vacancy trajectories are clearly seen to follow a biased walk as dictated by the existing stress gradients. The tests performed in Figs. 2.1 and 2.2 verify the model of Secs. 2.1.1 and 2.1.2 at the local level and gives us confidence to apply it for calculations of dislocation climb in realistic line geometries.

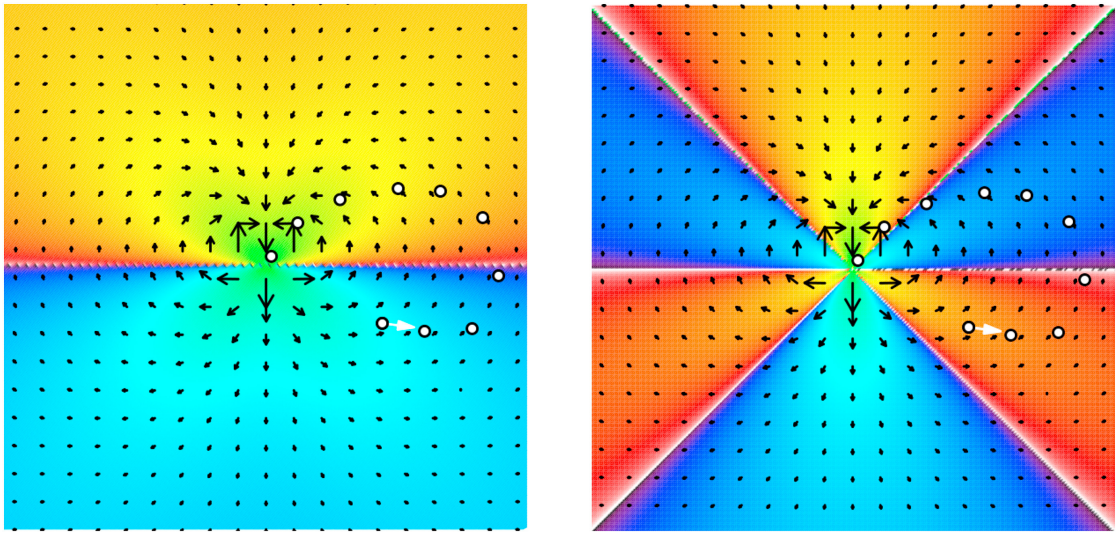

Figure 2.2: Stress and stress-gradient maps for an edge dislocation showing: (a) a contour plot of σ_{xx} (red: tensile, blue: compressive, arbitrary units) and the directional field of the $\frac{\partial \sigma_{kk}}{\partial x}$ component of vector (2.14) (shown with arrows); (b) Corresponding plot for σ_{yy} (red: tensile, blue: compressive, arbitrary units) and $\frac{\partial \sigma_{kk}}{\partial y}$. The trajectories of vacancies initially located at the point marked by the white arrow are highlighted using circles. The vacancy paths are seen to follow the direction of the stress gradient.

2.2.2 Dislocation climb calculations

Single dislocation behavior

Next, we systematically study dislocation climb in the ternary parametric space of pressure p, temperature T, and vacancy concentration C_v. To obtain climb velocities, we track the dislocation position normal to the glide plane as a function of time until steady state is reached and a linear relation is established between the two. We then calculate the climb velocity, v_c, as the slope of this linear relationship, as shown in the example in Figure 2.3. The graph shows the position of a 100-nm edge dislocation segment obtained from two independent measurements: (i) one according to eq. (2.15) (labeled 'vacancies absorbed') and (ii) another from the overall dislocation position ('center of mass'). As the figure shows, both approaches are equivalent and result in a climb velocity of 4.62×10^{-4} m·s^{-1}. This value of v_c corresponds to a temperature of T =1000 K, a pressure of $p = -100$ MPa (tensile),

with an equilibrium vacancy concentration $C_v \equiv C_0(p, T)$. A direct feature of our model is that h evolves with t in a discrete manner, with clear jumps (e.g. at 15, 26, 35, and 52 ns) correlating with vacancy absorption/emission events. This has a manifestation in the dislocation line morphology. Figure 2.4 shows the dislocation structure at the end of the simulation shown in Fig. 2.3. Vacancies are shown as small cyan spheres. The dislocation line displays a number of jogs consistent with the steps seen in Fig. 2.3. The shaded horizontal plane marks the original glide plane, while the shaded region normal to the glide plane marks the slipped climb area.

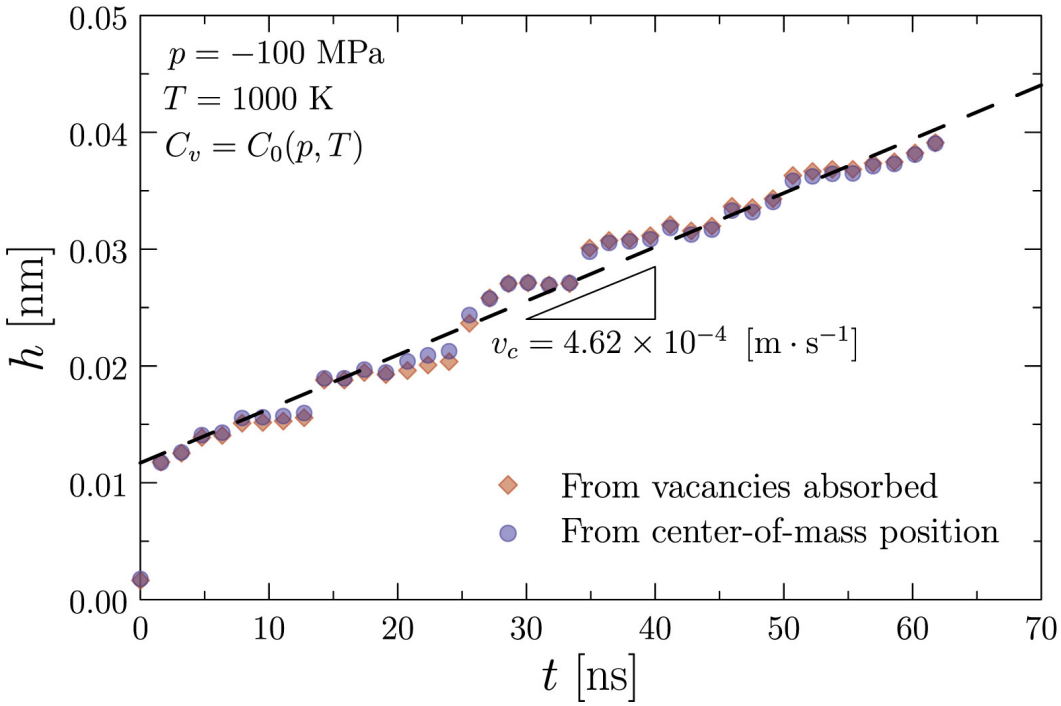

Figure 2.3: Dislocation position along the glide plane normal direction h as a function of time t at a temperature of 1000 K and a pressure of -100 MPa (tensile) and equilibrium vacancy concentrations. The graph shows the position obtained from two independent measurements: according to eq. (2.15) (labeled 'vacancies absorbed') and from the overall dislocation position ('center of mass'). The resulting climb velocity is extracted from a linear fit to the data points in steady state.

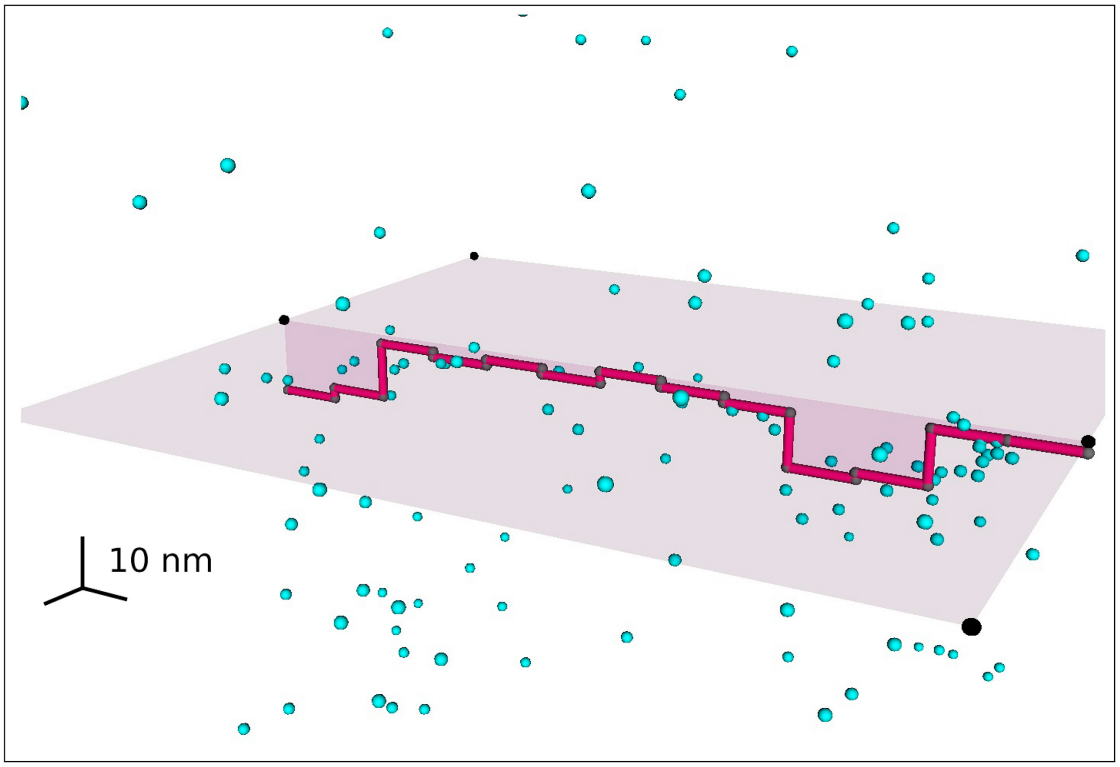

Figure 2.4: Dislocation structure after one microsecond at 1000 K and a pressure of -100 MPa with $C_v = C_0(T, p)$. Vacancies are shown as small spheres. The dislocation line displays a number of jogs originating from local vacancy emission (and/or absorption) events. The height of the jogs is commensurate with the Δh jumps displayed in Fig. 2.3, which are approximately 0.1 Å(single vacancy absorption/emission event). The shaded horizontal plane marks the original glide plane. The shaded region normal to the glide plane marks the slipped climb area.A scale marker for all three Cartesian directions is shown for reference.

Dislocation climb as a function of temperature, pressure, and vacancy concentration

We repeat the procedure described in the previous to obtain the fundamental climb velocity dependencies as a function of T, p, and C_v. The results are given in Figure 2.5, where a sequence of plots is shown with the net climb velocities of edge dislocation segments with lengths ranging between 50 to 500 nm under different combinations of temperature, pressure, and vacancy concentration. The temperature and the pressure set the equilibrium vacancy concentration C_0 according to eq. (2.16), which at, e.g., -100 MPa and 1000 K (conditions in Fig.

2.3) is 2.45×10^{-9}. A multiplication factor is then applied to C_0 as to artificially increase the vacancy concentration to nonequilibrium levels to study its effect on v_c. Dislocation climb velocities are calculated as in Fig. 2.3, with each data point representing the average of five statistically independent simulations. The error bars displayed correspond to the standard deviations for each condition. Each row of figures shows the climb velocity as a function of a primary variable and two secondary variables. In the top row, the primary dependency is on temperature, while secondary dependencies are on pressure (colors) and global vacancy concentration (left to right). In the middle row the primary dependency is on pressure, with secondary dependencies on global vacancy concentration (colors) and temperature (left to right). Finally, the bottom one contains the relationship of the climb velocity with the global vacancy concentration, along with secondary dependencies on temperature (colors) and pressure (left to right). In all curves, dashed lines correspond to climb velocities using eq. (2.18) for vacancy emission, i.e. when the vacancy concentration is enforced in a 'global' way irrespective of the stress state at each of the dislocation segments. Conversely, continuous lines indicate that the velocities have been calculated under local conditions (with vacancy emission defined by eq. (2.17)).

Inspection of the results reveals the following general trends:

(i) As indicated earlier, velocities obtained enforcing global vacancy emission tend to be positive (shaded gray region in Fig. 2.5's plots), while local climb velocities are strongly negative. This points to regimes governed by vacancy absorption and emission, respectively.

(ii) The results are practically insensitive to pressures in the -100-to-100-MPa range.

(iii) The climb velocities have a clear exponential dependence on temperature.

(iv) The total vacancy concentration has an incremental effect on climb velocities, with higher vacancy concentrations resulting in higher values, both positive and negative. In the case of global vacancy emission, a larger C_v results in a higher rate of vacancy absorption and therefore faster positive climb

velocities[4]. Enforcing the global vacancy concentration, however, also results in an enhanced emission rate as the differential vacancy concentration around dislocation segments (global minus local) remains positive, keeping eq. (2.18) active for a longer time, leading to faster negative climb.

[4]Maintaining a constant vacancy supersaturation in globally acts as an inexhaustible vacancy source, with vacancies constantly being replenished as they disappear due to their interactions with dislocations.

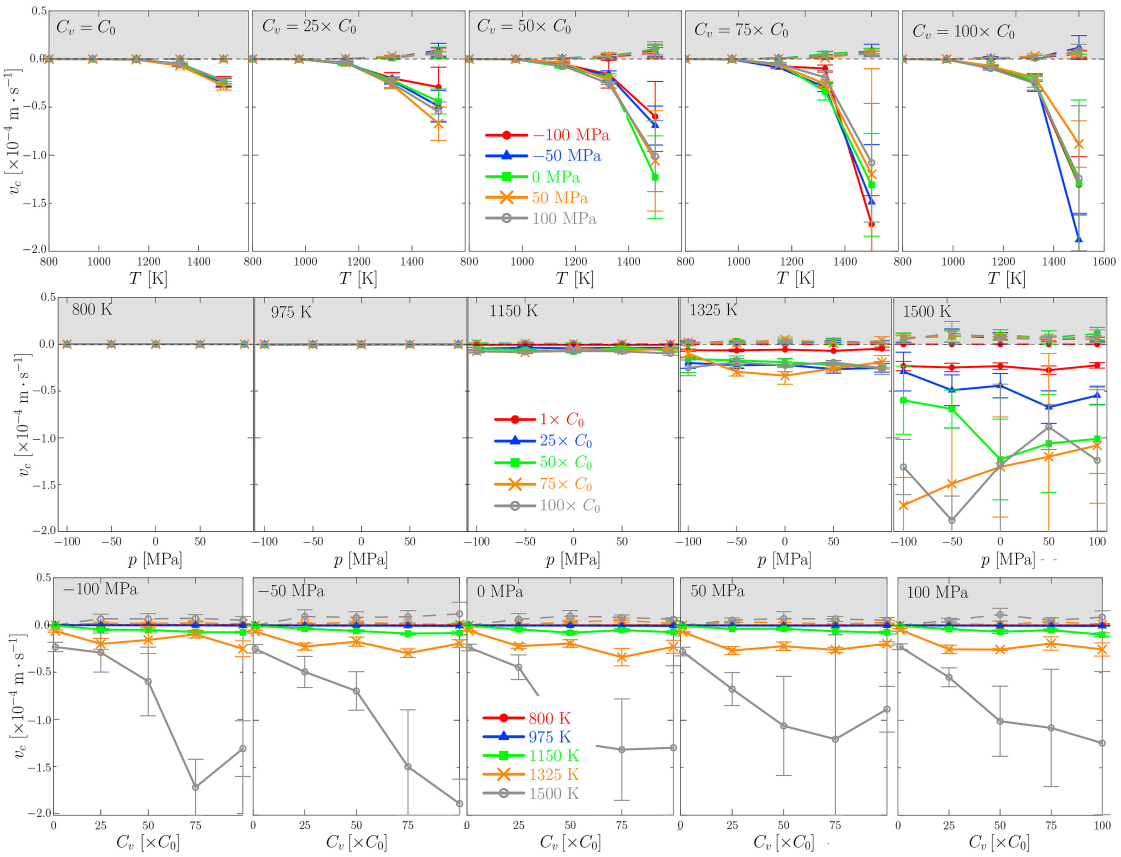

Figure 2.5: Sequence of plots showing the net climb velocities of edge dislocation segments with lengths ranging between 50 to 500 nm under different combinations of temperature, pressure, and vacancy concentration. The temperature and the pressure set the equilibrium vacancy concentration C_0 according to eq. (2.16). Then a multiplication factor is applied to C_0 so as to artificially increase the vacancy concentration to nonequilibrium levels. The average position of the entire dislocation line is then tracked with time and a climb velocity is extracted. Each row of figures shows the climb velocity as a function of a primary variable and two secondary variables. Top row: the primary dependency is on temperature; secondary dependencies are on pressure (colors) and global vacancy concentration (left to right). Middle row: primary dependency on pressure; secondary dependencies on global vacancy concentration (colors) and temperature (left to right). Bottom row: primary dependency on global vacancy concentration; secondary dependencies on temperature (colors) and pressure (left to right).

To further understand the processes that control the kinetic evolution in the simulations, it is useful to analyze the time step distribution of events. A representative set results is shown in Figure 2.6, where we have separated the histogram

into a δt-spectrum associated with vacancy diffusion/absorption events (shown in red), and another one corresponding to vacancy emission events (in blue). It can be seen that diffusion/absorption is governed by much faster time scales than vacancy emission. The average of the blue histogram is approximately 3.0 ps, while that of the orange histogram is almost three orders of magnitude higher, ≈ 0.72 ns. These averages are both consistent with eqs. (2.1)-(2.2) and (2.17) at the conditions of the simulation.

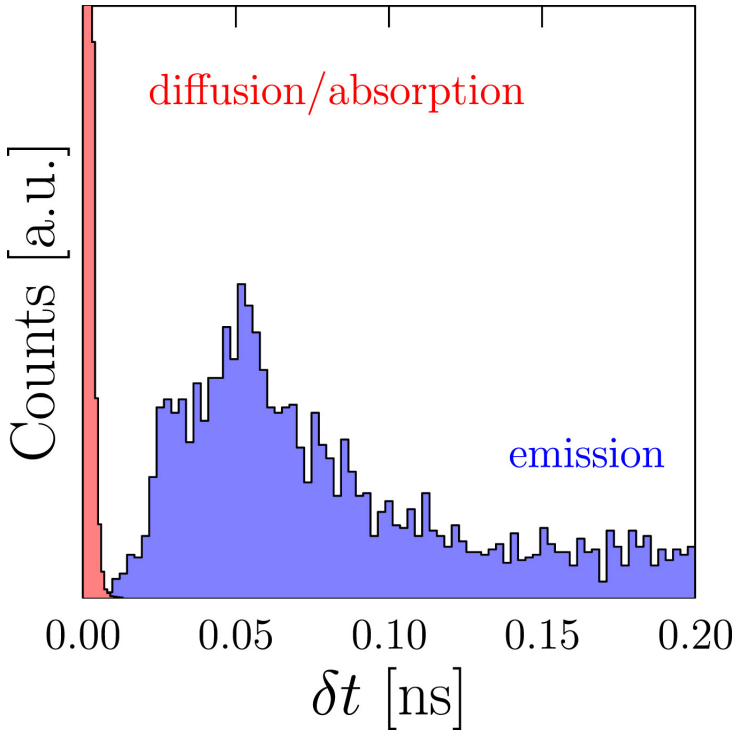

Figure 2.6: Histogram of time steps in a general climb simulation at 1000 K. The red histogram (shorter timescales) represents the spectrum of δt associated with vacancy diffusion/absorption, while the blue one (longer time steps) represents vacancy emission events. The large spread in the distributions gives an idea of the range of stress spatial variations found in the computational domain.

The large spread in the vacancy emission distribution gives an idea of the wide range of stress spatial variations found in the computational domain. In contrast, vacancy diffusion is defined by a much narrower spectrum. The clear separation of scales between both time distributions results in a numerically-stiff system, which makes it amenable to certain speedup procedures that can increase

the computational efficiency [77–80]. In fact, the histogram displayed in the figure points to the causes behind the relatively high computational cost in some of the studied cases. The actual CPU cost of the simulations in Fig. 2.5 is discussed in B.2.3 and shown in Figure B.13.

2.2.3 Climb mobility functions

We can now use the results from Section 2.2.2 to parameterize climb mobility functions to be used in *parametric* dislocation dynamics simulations. The climb contribution to the mobility of a dislocation segment i in DDD is given by eqs. (2.19) in Section 2.1.4. In those equations f^{el} and f^{os} represent two distinct driving forces for dislocation climb:

(i) The existence of non-glide elastic forces, represented by f^{el}, breaks the local vacancy equilibrium at the nodal or segment level, resulting in an imbalance that is resolved by stimulating vacancy diffusion into or out of the dislocation core. As such, these forces can produce climb even in the absence of a *global* vacancy supersaturation. A well-known example of this interaction is climb-induced bypass of precipitates or inclusions blocking dislocations in hardened alloys at high temperatures. While global thermodynamic equilibrium may exist, hydrostatic elastic forces created by the precipitates on dislocations distort local equilibrium facilitating vacancy-assisted climb.

(ii) Complementarily, dislocations can climb in the absence of elastic forces when the global vacancy concentration is far-from-equilibrium e.g. as in quenched metals or irradiation conditions, both of which can produce high vacancy supersaturations. This driving force is represented by f^{os}. Note that, as shown in C.1, stress gradients confer a mechanical bias to the osmotic force that is not captured in standard theories of dislocation climb.

The model presented here naturally captures both driving forces. Indeed, the so-called 'global' emission model numerically represents f^{os}, while the 'local' model represents f^{el}. Fortunately, emission-dominated conditions lead to 'downward' climb, i.e. along the direction of the tensile region of the stress field of an edge

dislocation, while absorption dominated climb takes place 'upwards', or towards the compressive semi-plane. As such, osmotic and stress-induced climb work in opposite directions, which allows us to separate their contribution.

Next, we apply the data in Fig. 2.5 (dashed lines) to eq. (2.20). The ratio of v_c and f^{os} gives the climb mobility, which we show in Figure 2.7(a) as a function of inverse temperature and C_v[5].

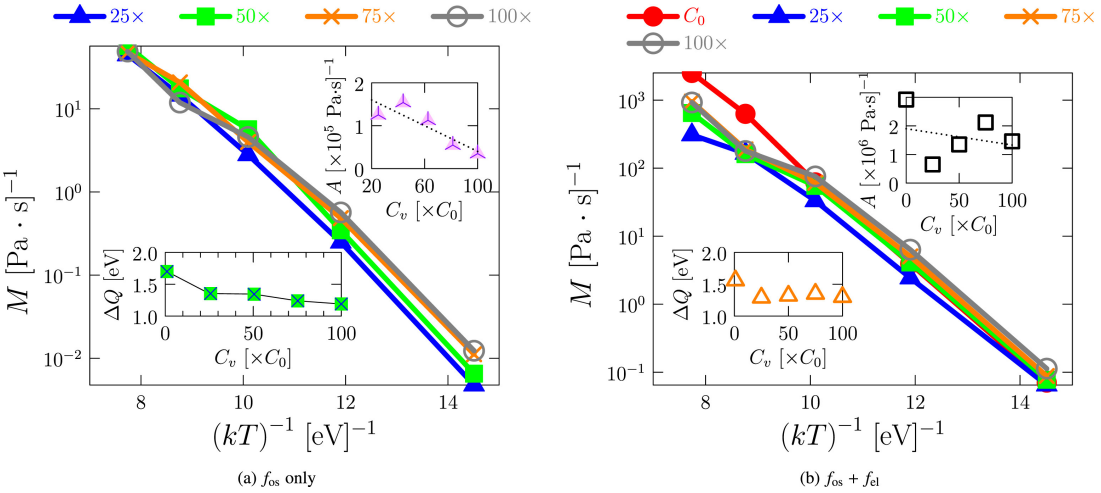

Figure 2.7: Inverse temperature dependence of M_c for several nonequilibrium vacancy concentrations (given as a multiplier of the vacancy concentration $C_0(T,p)$). The lower and upper insets in both graphs show the activation energies and pre-factors for each curve, respectively, assuming an Arrhenius expression.

The results show that even after accounting for the linear temperature dependence of f^{os} (eq. (2.20)) M_c consistently displays an Arrhenius form of the type:

$$M_c(T, C_v) = A\left(\frac{C_v}{C_0}\right)\exp\left(-\frac{\Delta Q}{kT}\right) \tag{2.21}$$

where A is a pre-factor that depends on the C_v/C_0 ratio and ΔQ is an activation energy. The dependence of ΔQ on C_v is shown in the lower inset to Fig. 2.7(a), where a weak decline from 1.7 to 1.2 eV can be appreciated. This correlates well with vacancy nucleation –characterized by an activation energy of 1.7 eV– playing a decreasingly important role as the global vacancy concentration increases. The dependence on the ratio $y = C_v/C_0$ is less clear (upper inset) but can be

[5]Note that no driving force exists when $C_v = C_0$ and so the climb velocity is nominally zero.

approximated reasonably well by a linear relation (shown as a dotted line on the upper figure inset):

$$A(y) = 1.9 \times 10^5 - 1.5 \times 10^3 y \;\; [\mathrm{Pa}^{-1}\ \mathrm{s}^{-1}] \tag{2.22}$$

The above mobilities pertain to simulations under the action of chemical forces alone. When elastic forces act in conjunction with these chemical forces, we get the (negative) climb velocities given in Fig. 2.5. From these, as in eq. (2.21), a mobility can be extracted:

$$M_c = \frac{v_c}{f^{\mathrm{el}} + f^{\mathrm{os}}}$$

The only stress component conducive to climb is the diagonal component along the glide direction (i.e. $\boldsymbol{n}\times\boldsymbol{t}$, usually taken as σ_{xx}). However, while this component can be prescribed via the applied stress, local stresses due to jogs in the dislocation line can also contribute to the elastic climb force (recall Fig. 2.4). These are difficult to quantify, however, due to their highly local and fluctuative nature, which means that it is difficult to specify f^{el} with precision. If we go strictly by the applied force, the results of the analysis using the same tools as for eq. (2.20) are shown in Figure 2.7(b). As in Fig. 2.7(a), the mobilities follow an Arrhenius evolution with temperature, characterized by the corresponding activation energies and pre-factors. The lower inset in Fig. 2.7(b) shows that the activation energies are not unlike those for the case with no elastic forces, ranging between 1.5 and 1.3 eV. The pre-factors (upper inset in Fig. 2.7(b)), however, are approximately one order of magnitude higher than their 'chemical' counterparts. We attribute this difference to localized and fluctuating elastic climb forces that develop owing to the discrete nature of our model. These pre-factors do not exhibit a clear trend with C_v, showing almost a concentration-independent behavior:

$$A(y) = 1.9 \times 10^6 - 5.7 \times 10^3 y \;\; [\mathrm{Pa}^{-1}\ \mathrm{s}^{-1}] \tag{2.23}$$

Note that in the temperature range studied here, climb mobilities range from approximately three to four orders of magnitude smaller than glide mobilities at low temperatures, to comparable values at 1500 K (e.g., for Fe, refs. [81, 82]).

2.2.4 Application: dislocation climb over a spherical precipitate

We finish the Results section with a more practical application of the method. It is known that one of the mechanisms of dislocation-based creep is climb over precipitates that exert a force on dislocations greater than the glide force. Here, we simulate such a process by considering a spherical precipitate 4 nm in radius with an associated volumetric field characterized by stresses $\sigma_{rr} \propto 1/r^3$ [83]. The dislocation is then driven towards the precipitate by glide with a force insufficient to cut or loop around it. Aided by the volumetric force and by temperature, the dislocation can then climb by vacancy emission and circumvent the precipitate, continuing its glide. The simulations are conducted with a modified version of the `DDLab` code that includes spherical inclusions [83] and to which we add the kMC module developed here. A sequence of snapshots showing this process, together with the number and position of the emitted vacancies is shown in Figure 2.8. Note the relative large local concentration of vacancies along the climb path.

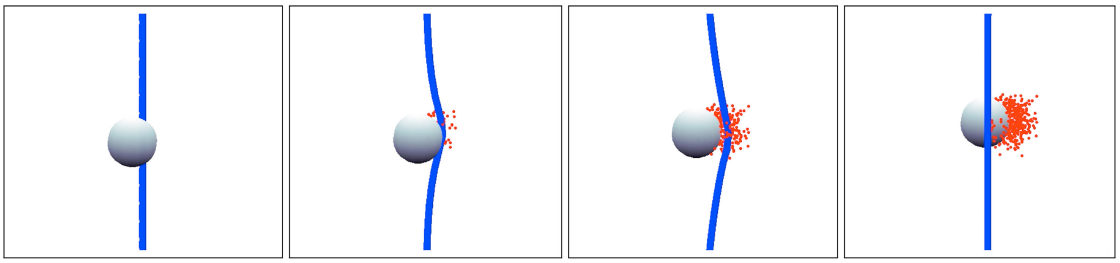

Figure 2.8: Sequence of snapshots of an edge dislocation undergoing climb over a spherical precipitate in equilibrium conditions. The applied stress produces a force only along the glide direction that is insufficient to curve the dislocation around the precipitate on the glide plane. The images show the vacancies emitted while the dislocation climbs.

Additional analysis is given in Figure 2.9 where the dislocation configuration at the point of maximum climb is provided. The color background in the figure represents the intensity of the radial stress caused by the precipitate in the matrix (in arbitrary units). The black dashed line represents the original glide plane (the equatorial plane of the precipitate), while the superimposed curve gives the number

of vacancies emitted as a function of distance to the precipitate's outer radius. The combined action of the line tension, the glide force, and the precipitate stress field shape the dislocation line into an arced configuration as shown in the figure. Note that the timescale is arbitrary but the glide mobilities are about four orders of magnitude larger than climb mobilities.

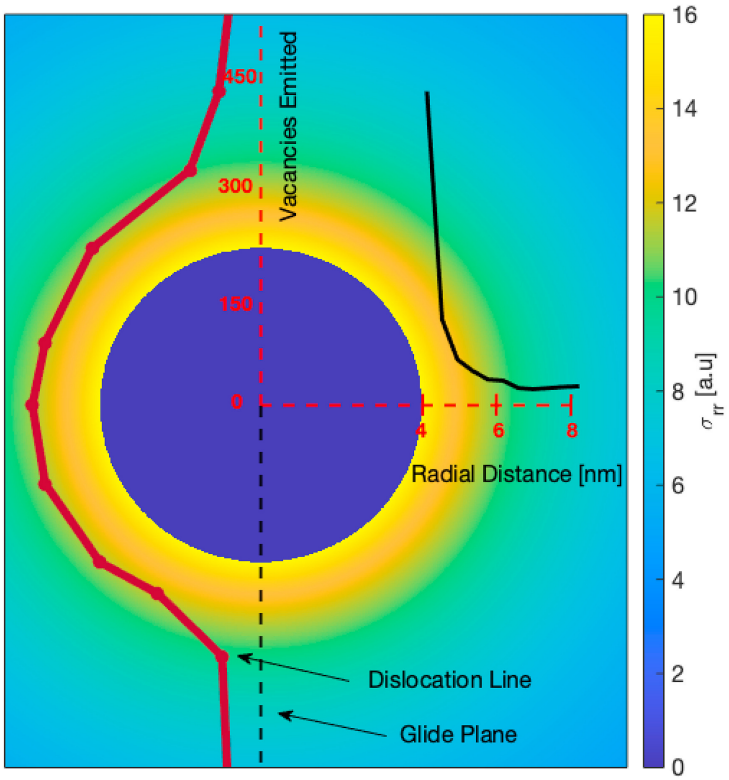

Figure 2.9: Dislocation configuration at the point of maximum climb during simulations of temperature-enabled precipitate bypassing by an edge dislocation. The precipitate has spherical shape with a radius of 4 nm. The color background represents the intensity of the radial stress caused by the precipitate in the matrix (in arbitrary units). The black dashed line represents the original glide plane (the equatorial plane of the precipitate), while the superimposed curve gives the number of vacancies emitted as a function of distance to the precipitate's outer radius.

These can be regarded as direct simulations of elementary creep mechanisms on time scales much longer than those associated with glide.

2.3 Discussion

2.3.1 The need for discreticity and stochasticity

First we justify the need for works such as the present one. Vacancy emission and diffusion are both thermally-activated processes, while dislocation network evolution is driven by elastic forces. However, while dislocation climb involves the conjunction of both phenomena, they typically act on very different length and time scales. Moreover, point defect processes are intrinsically stochastic in that they are driven by thermal fluctuations. As such, kMC is the pertinent method to study them, whereas DDD is the preferred tool to simulate dislocation dynamics. This work combines both techniques in a self-consistent way, i.e. (i) DDD resolves the elastic fields created by the dislocation structure, (ii) the kMC module evolves the vacancy subpopulation embedded in these fields, and (iii) dislocation-defect processes alter the dislocation substructures, giving rise to updated elastic fields. To our knowledge, the only prior work where kMC was linked to DDD was that by Ghoniem et al. [84] to study defect decoration of dislocation loops. Our approach considers a drift on vacancy diffusion created by stress fields, which leads to an expression governed by stress gradients. This problem has been considered by several authors in the past [62, 85], albeit using a different approach to the one presented here.

Another thing worth emphasizing of this work is its discrete nature. Studies where the point nature of defects is directly accounted for are rare in the plasticity and DDD community. Direct atomistic calculations can only cover limited length and time scales [20, 86], often too small or too short for steady state defect fluxes to occur. Mesoscopic models are better equipped to deal with the combination of small length scales and long time scales, but they can suffer from numerical stiffness. A model of dislocation climb based on elementary jog kinetics has been recently proposed [42]. These are examples that discreticity and elasticity can be merged with relative high efficacy. Our method is a demonstration that defect generation, absorption, and diffusion can be treated in a point-like manner in conjunction with discrete dislocation dynamics.

It is important to note, however, that some relevant vacancy-related mechanisms are not captured by the present model. We do not consider pipe diffusion (diffusion along the dislocation line), which is known to be of importance in certain cases [87–90]. As well, vacancy clustering is not a feature of our approach, although atomistic studies have revealed conclusively that small vacancy clusters are unstable and have a short lifetime in bcc metals at the high temperatures explored here [91–93]. Finally, our results pertain to bulk material grains, without considering the effects of grain boundaries, which are known to be very effective vacancy sources/sinks and could alter the local and global vacancy supersaturation limits compared to those in ideal conditions.

2.3.2 Climb dynamics

Climb takes place under the action of two distinct forces, see eq. (2.19). The osmotic force is characterized by vacancy absorption due to the existence of a vacancy supersaturation and, as such, results in 'upwards' climb (along the direction of the compressive half-plane). Elastic climb, on the other hand, activates itself via vacancy emission and thus leads to climb in the direction of the tensile half-plane of the edge component of a dislocation. This elastic force clearly represents a mechanical bias conveyed by the stress at each point. The osmotic force, while in principle not a bias in the thermodynamic sense, is influenced by the stress gradient via the drift term in eq. (2.14), which can also be regarded a mechanical bias (although a second order one, see B.3). In this sense, our approach differs from the classical one in that locality is a feature of both $\boldsymbol{f}^{\mathrm{el}}$ and $\boldsymbol{f}^{\mathrm{os}}$, not just of $\boldsymbol{f}^{\mathrm{el}}$ [1, 22–25, 94].

Indeed, the classical treatment of dislocation climb suggests that the osmotic force scales with the vacancy supersaturation level. However, as our approach reveals, at the local level (near each dislocation segment), the local concentration is often zero, so that the driving force for vacancy emission is almost independent of the global vacancy concentration. As well, stress induced climb is seen to clearly dominate over chemical climb because the mechanical bias that controls vacancy emission (local stresses) is dominant over drift effects brought about by stress

gradients that control vacancy absorption.

2.3.3 Mobility functions

Mobility functions relate forces (stresses) and dislocation velocities and thus are an essential constitutive input to DDD simulations. For climb, it is generally impractical to simulate vacancy-dislocation coevolution in the manner done here, or as in molecular dynamics simulations. Hence, the present simulations should be seen as an intermediate step linking vacancy kinetics with dislocation dynamics, providing a general-purpose mobility functions with dependencies on the relevant state variables of the problem. Several authors have derived climb mobilities of the type [1, 25, 94, 95]:

$$M_c = \frac{2\pi D_v \Omega_a C_0}{kTb^2 \sin^2\theta \ln(r_\infty/r_0)} \tag{2.24}$$

obtained by linearizing the exponential term containing the mechanical work done by the elastic force (D_v is the vacancy diffusivity, and r_∞ and r_0 are the standard elastic integration limits around a dislocation). θ represents the dislocation character, with $\sin\theta = 1$ for edge dislocations. The application of this expression in DDD simulations has been tested in depth [96] showing that it can work qualitatively for situations such as prismatic loop expansion and 'raft' microstructure formation. Our expression, by contrast, emanates from elementary vacancy processes such as lattice diffusion, emission, and absorption, and includes spatial and time fluctuations intrinsically. A comparison of both mobilities in the $800 < T < 1500$ K interval is provided in Figure 2.10. An obvious difference is that, in our treatment, the mobility function itself depends on the vacancy supersaturation C_v/C_0, whereas eq. (2.24) does not. The most important difference to note, however, is how much faster the present mobilities are compared to the classical ones represented by eq. (2.24) (between two to three orders of magnitude, respectively, at high and low temperatures). We again rationalize this in terms of the local nature of vacancy absorption/emission, which is not captured by classical models based on homogeneous vacancy concentrations and smooth defect fluxes into or out of dislocation segments. Further studies are recommended to establish the correct time scale of climb in bcc metals.

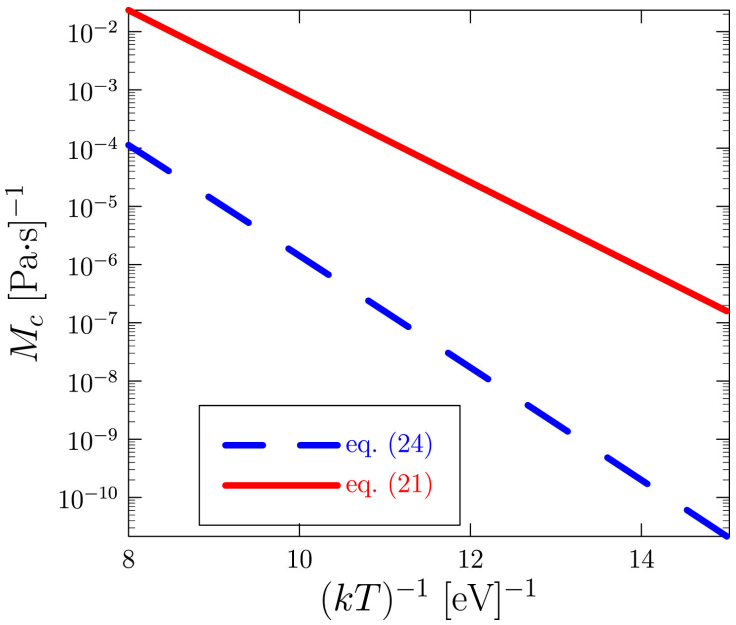

Figure 2.10: Comparison between eqs. (2.21) (present climb mobility expression, dashed blue) and (2.24) (expression by Bako et al. [1], red continuous).

The final expression for the climb velocity for general use in DDD simulations is:

$$\boxed{v_c = A(y)\exp\left(-\frac{\Delta Q(y)}{kT}\right)\left[\frac{kT}{\Omega_a}\left(\frac{y-1}{y}\right)-\sigma_{xx}\right]b\sin\theta} \tag{2.25}$$

where $y = \frac{C_0}{C_v}$, $\Delta Q(y) \approx 1.3$ eV and $A(y)$ given by eqs. (2.22) and (2.23), σ_{xx} is the corresponding component of the local stress tensor at segment i, $\boldsymbol{\sigma}(\boldsymbol{r}_i)$, and $\theta = \cos^{-1}\left(\frac{\boldsymbol{b}\cdot\boldsymbol{t}}{b}\right)$.

2.4 Conclusions

We separate our conclusions into those relevant for the theory of plasticity and those that are technical in nature. Our main physical conclusions are:

- Stress gradients control vacancy diffusion in the presence of dislocation elastic fields. This results in a drift on vacancy transport that steers defects towards dislocation cores, conferring a mechanical bias to an otherwise 'chemical' process.

- Climb is dominated by vacancy emission even when the background vacancy concentration is much higher than the equilibrium one. This is because local vacancy conditions control the overall kinetics, as captured in our approach, whereas classical treatments assume smooth vacancy fluxes from homogeneous defect concentrations.
- Climb velocities might be much faster than otherwise believed when one uses the classical theory of climb. Again, a consequence of local vacancy-dislocation interactions.

Our main technical conclusions are:

- We have developed a discrete stochastic model of vacancy evolution in the presence of arbitrary elastic fields furnished by DDD methods. Vacancy kinetics include emission, diffusion, and absorption, rigorously coupled to underlying dislocation fields, while absorption/emission events change the dislocation microstructure which is updated in time and, with it, the elastic fields.
- The method enables the calculation of dislocation climb mobility functions as a function of temperature, pressure, and vacancy concentration, to be directly used in parametric DDD simulations. The calculated climb mobilities are over 100× larger than those from previous derivations.
- Preliminary calculations of dislocation bypassing of spherical precipitates demonstrate that the method is capable of simulating physical processes conducive to high-temperature creep.

B.1 Validation of the Drift-Diffusion Expression via convergence to the Classical Analytical Vacancy Concentration Solution

In this section, we carry out a numerical analysis of the spatially-dependent drift-diffusion equation and compare its solutions with the spatially-independent

analytical solution employed to obtain the results shown in the main body of this work.

B.1.1 Derivation of the vacancy diffusion equation

We start from Fick's second law applied to the field-dependent vacancy concentration $c(\boldsymbol{r})$:

$$\frac{\partial c(\boldsymbol{r})}{\partial t} = \nabla_{\boldsymbol{r}} \cdot (D_v(\boldsymbol{r})\ \nabla_{\boldsymbol{r}} c(\boldsymbol{r})) \tag{B.26}$$

where $D_v(\boldsymbol{r})$ is the position-dependent vacancy diffusivity, $\boldsymbol{r} = (x, y, z)$, and $\nabla_{\boldsymbol{r}} = \left(\frac{\partial}{\partial x}\boldsymbol{i}, \frac{\partial}{\partial y}\boldsymbol{j}, \frac{\partial}{\partial z}\boldsymbol{k}\right)$. Expanding the above equation:

$$\frac{\partial c}{\partial t} = \nabla_{\boldsymbol{r}} D_v \cdot \nabla_{\boldsymbol{r}} c + D_v \nabla^2_{\boldsymbol{r}} c \tag{B.27}$$

where we have dropped the explicit dependence on $\boldsymbol{r}$ for ease of notation. We consider thermally-activated vacancy diffusion, i.e.:

$$D_v(\boldsymbol{r}, T) = D_0 \exp\left(-\frac{E_m(\boldsymbol{r})}{kT}\right)$$

where the spatial dependence of D_v is implicit in the migration energy E_m (D_0 is a temperature independent pre-factor). In fact, E_m can be unfolded into a constant part and a spatially-dependent part:

$$E_m(\boldsymbol{r}) = E_m^0 + E(\boldsymbol{r})$$

from which we can rewrite the diffusivity $D_v(\boldsymbol{r}, T)$ as:

$$D_v(\boldsymbol{r}, T) = D_0 \exp\left(-\frac{E_m^0}{kT}\right) \exp\left(-\frac{E(\boldsymbol{r})}{kT}\right) = D_v^0(T) \exp\left(-\frac{E(\boldsymbol{r})}{kT}\right) \tag{B.28}$$

Inserting this expression into eq. (B.27), we arrive at:

$$\frac{\partial c}{\partial t} = D_v^0 \left(\nabla^2_{\boldsymbol{r}} c - \frac{\nabla_{\boldsymbol{r}} E(\boldsymbol{r})}{kT} \nabla_{\boldsymbol{r}} c\right) \tag{B.29}$$

Equation (B.29) can be regarded as a drift-diffusion equation, $\partial c/\partial t = D_v \nabla^2_{\boldsymbol{r}} c - \boldsymbol{u} \cdot \nabla_{\boldsymbol{r}} c$, with drift velocity:

$$\boldsymbol{u} = D_v^0 \frac{\nabla_{\boldsymbol{r}} E(\boldsymbol{r})}{kT}$$

Assuming that vacancies interact only with the hydrostatic part of the stress field, we can write:

$$E(\boldsymbol{r}) = -\frac{\Omega_0}{3}\sigma_{kk}(\boldsymbol{r}) = p(\boldsymbol{r})\Omega_0 \tag{B.30}$$

where $p(\boldsymbol{r}) = -\frac{1}{3}\mathrm{Tr}\left(\boldsymbol{\sigma}(\boldsymbol{r})\right)$ is the local pressure. Given that the relaxation volume of a vacancy is negative $\Omega_0 < 0$, equation (B.30) shows that vacancies prefer segregating towards points in a material where hydrostatic pressure is high.

Substituting the pertinent terms in equation (B.29) leads to the final governing equation:

$$\frac{\partial c}{\partial t} = D_v^0\left(\nabla_{\boldsymbol{r}}^2 c - \frac{\Omega_0}{kT}\nabla_{\boldsymbol{r}} p(\boldsymbol{r}) \cdot \nabla_{\boldsymbol{r}} c\right) \tag{B.31}$$

where we recall that D_v^0 is a the temperature-dependent part of the vacancy diffusivity.

B.1.2 Elastic stresses

Assuming isotropic elasticity, the pressure created by a perfect edge dislocation segment i with Burgers vector $\boldsymbol{b}^{\mathrm{e}}$ lying on glide plane $\boldsymbol{n}$ at a point $\boldsymbol{r}'$ is:

$$p_i(\boldsymbol{r}') = \frac{\mu b^{\mathrm{e}}}{3\pi}\left(\frac{1+\nu}{1-\nu}\right)\frac{\boldsymbol{n}\cdot\boldsymbol{r}'}{|\boldsymbol{n}\cdot\boldsymbol{r}'|^2 + |\boldsymbol{r}'\cdot\boldsymbol{s}'|^2} = \frac{\mu b^{\mathrm{e}}}{3\pi}\left(\frac{1+\nu}{1-\nu}\right)\frac{\sin\theta'}{r'} \tag{B.32}$$

where $\boldsymbol{s} = \boldsymbol{b}^{\mathrm{e}}/b^{\mathrm{e}}$ (*slip* direction) and $\boldsymbol{n}$ are unit vectors, and $b^{\mathrm{e}} = \|\boldsymbol{b}^{\mathrm{e}}\|$. Here

$$\boldsymbol{r}' = \boldsymbol{r} - \boldsymbol{r}_i, \quad r' = \|\boldsymbol{r}'\|, \quad \theta' = \arctan\frac{x'}{y'}$$

where $\boldsymbol{r}_i$ indicates the edge dislocation position and $\boldsymbol{r}$ is a generic spatial point. The spatial gradient of p_i in cylindrical coordinates is:

$$\nabla_{\boldsymbol{r}'} p_i(\boldsymbol{r}') = \frac{\mu b^{\mathrm{e}}}{3\pi}\left(\frac{1+\nu}{1-\nu}\right)\left[-\frac{\sin\theta'}{r'^2}, \frac{\cos\theta'}{r'}, 0\right] \tag{B.33}$$

Next, we assume for simplicity only a radial dependence of c, i.e., $c(r)$. We simplify eq. (B.31) to:

$$\frac{\partial c}{\partial t} = D_v^0\left(\frac{\partial^2 c}{\partial r^2} + \frac{\mu b^{\mathrm{e}}\Omega_0}{3\pi kT}\sum_i \frac{f(\theta_i)}{(r-r_i)^2}\frac{\partial c}{\partial r}\right) \tag{B.34}$$

where $f(\theta')$ is an intensity factor (≤ 1) due to each dislocation segment. Further, we take $f(\theta) = 1$ for convenience and assume that the summation is dominated by the term defined by $r_i \approx 0$ (i.e., very close to the dislocation segments):

$$\frac{\partial c}{\partial t} \approx D_v^0 \left(\frac{\partial^2 c}{\partial r^2} + \frac{\mu b^e \Omega_0}{3\pi kT} \frac{1}{r^2} \frac{\partial c}{\partial r} \right) \tag{B.35}$$

B.1.3 Finite difference solution in one dimension

The discretized version of eq. (B.35) taking finite differences is:

$$c_j^{n+1} = a_1 c_{j+1}^n + a_2 c_j^n + a_2 c_{j-1}^n \tag{B.36}$$

with:

$$a_3 = \frac{D_v^0 \delta t}{\delta x^2}, \quad a_2 = a_3 \left(\frac{\mu b^e \Omega_0}{3\pi kT} \frac{\delta x}{x_j^2} - 2 \right), \quad a_1 = a_3 \left(1 - \frac{\mu b^e \Omega_0}{3\pi kT} \frac{\delta x}{x_j^2} \right)$$

In eq. (B.36) j and n are sub(super) indices representing spatial and temporal points on a x-t grid with resolution δx and δt, respectively. For structured meshes, where $x_j = j\delta x$, the coefficients a_1 and 2 can be simplified to:

$$a_1 = a_3 \left(1 - \frac{\mu b^e \Omega_0}{3\pi kT} \frac{1}{j x_j} \right), \quad a_2 = a_3 \left(\frac{\mu b^e \Omega_0}{3\pi kT} \frac{1}{j x_j} - 2 \right)$$

where j represents a position in the spatial mesh.

parameter	units	value
μ	eV Å^{-3}	0.749
b^e	Å	2.73
Ω_0	Ω_a	-0.37
Ω_a	Å^3	15.7
k	eV K^{-1}	8.615×10^{-5}
E_m^0	eV	1.6
D_0	m^2 s^{-1}	10^{-6}
T	K	1400

Table B.2: Material parameters for Mo. The value of the shear modulus in GPa is 120.

The relevant solutions are found for a 1D spatial grid subjected to a 'left' boundary condition represented by a concentration delta:

$$c(0;0) = c_0$$

We use iron as model material, described by the properties in Table B.2.

Next, we aim to check whether the standard solution for constant drift velocity used in the main text can be taken as a satisfactory approximation of the exact solution for a spatially-drift given by eq. (B.36). The standard solution in one dimension is written as:

$$c(x,t) = \frac{1}{\sqrt{4\pi D_v^0\, t}} \exp\left(-\frac{(x-ut)^2}{4D_v^0 t}\right) \tag{B.37}$$

where t is the time elapsed. The approximation between both is considered to be satisfactory if the two solutions are sufficiently close to one another within the timescale of vacancy jumps. Figure B.11 shows realizations of eqs. (B.36) and (B.37) at 1400 K at the firs point of substantial overlap, which takes place at a time of 1.4×10^{-15} s. Thereon, both profiles maintain a substantial level of spatial overlap, which can be used to justify the use of the analytical solution. Figure B.12 shows a histogram of the sampled time steps from the coupled DDD/kMC technique, revealing simulated δt in the range of 10^{-13} to 10^{-10} s, i.e., several orders of magnitude greater than the $\approx 10^{-15}$ s necessary to converge. We take this as direct verification that eq. (B.37) represents a good approximation to the exact solution of the vacancy diffusion equation with spatially-dependent drift over the timescale of vacancy jumps.

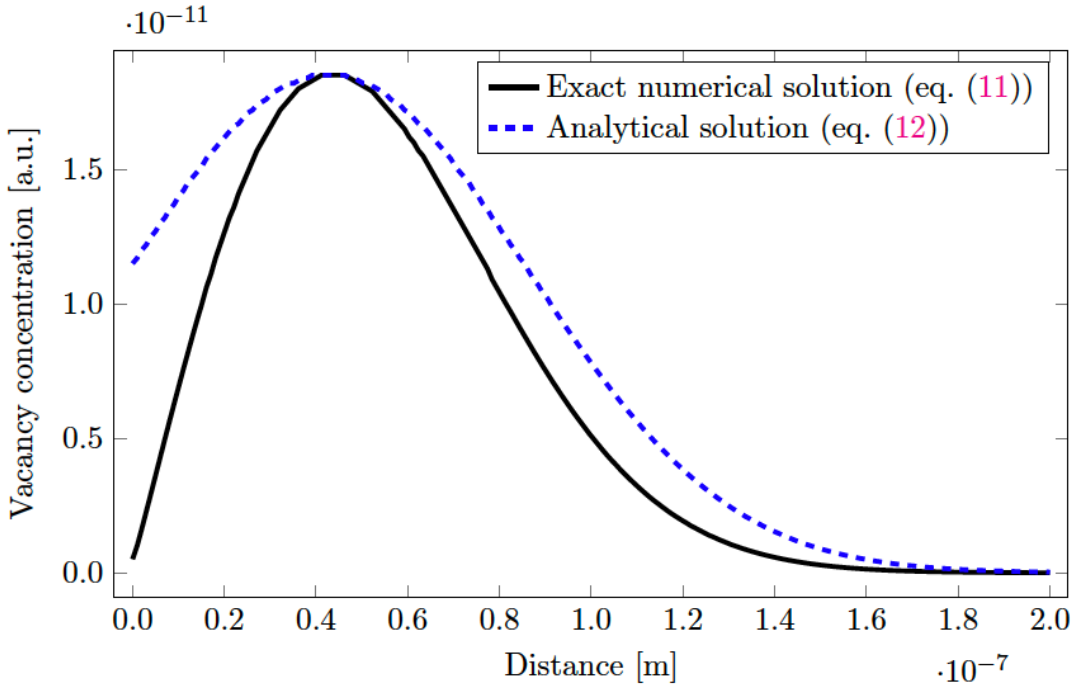

Figure B.11: Convergence of the finite difference (solid black line) and the analytical solution (dashed blue line) at 1400 K and $t = 1.4 \times 10^{-15}$ s.

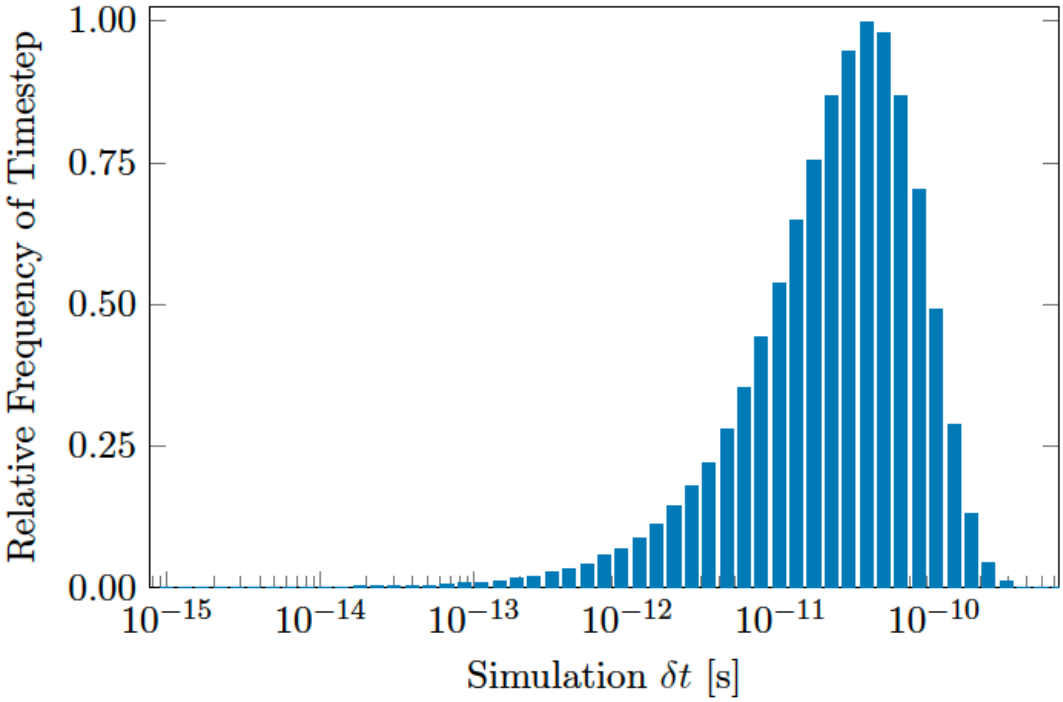

Figure B.12: Histogram of sampled timesteps from the DDD/kMC coupled method at 1400 K.

B.2 Numerical solution procedure

The challenge in solving eq. (2.14) using expression (2.8) is that δx_i and u_i have an implicit relationship. That is, to compute u_i one needs to know δx_i, which itself is sampled from the solution to the drift-diffusion equation (2.8) which requires u_i as an input. Solving this requires running a self-consistent iterative procedure until the values of δx_i and u_i self-consistently converge.

B.2.1 The Box-Müller sampling

To sample from eq. (2.8) we use the Box-Müller approach [97], by which two random samplings z_1 and z_2 are generated using:

$$z_1 = \sqrt{-2\ln\xi_1}\cos(2\pi\xi_2)$$

$$z_2 = \sqrt{-2\ln\xi_1}\sin(2\pi\xi_2)$$

where ξ_1 and ξ_2 are two uniformly distributed random numbers in the $(0, 1]$ interval. From this, the jump steps obtained are:

$$(\delta x_i)_{1,2} = u_i \delta t + z_{1,2}\sqrt{2D\delta t} \tag{B.38}$$

Note that δt is an input to the sampling procedure, but it is *a priori* unknown. This means that it also should be determined self-consistently (iteratively).

B.2.2 Numerical algorithm

Next, we present the recursive algorithm used to integrate the transport equations.

Algorithm 1 Numerical procedure to solve the vacancy elasto-diffusion model.

Initialize: TOL, `maxiter`, t_{TOT}.
for $n = 1$, `maxiter` **do**
  Initialize: $\delta t = \delta t^{n-1}$, $\delta t' = 0$.
  Initialize/update: R_{TOT}
  Initialize/update: $N, M \rightarrow$ DDD lib.
  while $|\delta t - \delta t'| >$ TOL **do**
    for $ivac = 1, N$ **do**
      Get: $\mathbb{R}^3$ point $\boldsymbol{P}(ivac)$
      Get: stress tensor $\boldsymbol{\sigma}(\boldsymbol{P}) \leftarrow$ DDD lib.
      Calculate: $\nabla_{\boldsymbol{x}}\text{Tr}(\boldsymbol{\sigma})$ vector at $\boldsymbol{P}$ as indicated in eq. (14).
      for $j = 1, 3$ **do**
        Select: trial jump step δx_j.
        while $|\delta x_j - \delta x'_j| >$ TOL **do**
          Calculate u_j from δx_j and $\partial \sigma_{kk}/\partial x_j$ using eq. (14).
          Using u_j and δt, sample $\delta x'_j$ from Gaussian distribution (8).
        end while
        Calculate reaction rate: r_j^{ivac} as: $r_j^{ivac} = \left(2D/\delta x'_j\right)^2$
        $R_{\text{TOT}} = R_{\text{TOT}} + r_j^{ivac}$
      end for
    end for
    for $idisl = 1, M$ **do**
      Resolve all vacancy absorption instances and update nodal network (refer to eq. (15)) $\leftrightarrow$ DDD lib.
      Calculate vacancy emission rate r_{idisl} according to eq. (17).
      $R_{\text{TOT}} = R_{\text{TOT}} + r_{idisl}$
    end for
    Sample $\delta t'$ from Poisson distribution: $\delta t' = (R_{\text{TOT}})^{-1} \ln \chi$ (χ is a uniform random number).
  end while
  Sample event from uniform distribution R_{TOT} using binary search tree.
  Execute event: $\begin{cases} \text{- Displace vacancy along each directions by amount } \delta x_j,\ j = 1, 2, 3 \\ \text{or} \\ \text{- Insert vacancy in box} \end{cases}$
  $t_{\text{TOT}} = t_{\text{TOT}} + \delta t'$
  $n = n + 1$
end for

where N and M are, respectively, the number of vacancies and dislocation segments in the simulation box at any give time step. In this fashion, the DDD method acts as a library linked to the main workflow loop, from which information is passed bidirectionally. These links are highlighted in red color in the algorithm. Basically, algorithm (1) consists of two `for` loops nested within a `do-while` loop. Each of the `for` loops is tasked with computing event rates due to vacancy diffusion (first loop) and vacancy emission (second loop), respectively. As such, one runs over all vacancies while the other runs over all dislocation segments. The `do-while` loop ensures the self-consistency of the $\delta x \equiv \delta x'$ condition.

B.2.3 Computational cost

To assess the computational cost of the simulations conducted here (which follow algorithm (1)), we calculate the ratio of CPU time to simulated (physical) time as a function of pressure, temperature, and vacancy concentration. We find that temperature is overwhelmingly the dominant parameter, with pressure and vacancy concentration having only a minor impact on CPU time. An example is shown in Figure B.13, where the ratio of CPU time to simulated time for local and global vacancy emission implementations is given as a function of simulated temperature and pressure (with $C_v = C_0$). Temperature is seen to exponentially increase the CPU cost, while pressures up to ± 100 MPa have little to no effect on the computational efficiency. The local treatment of vacancy emission adds a cost factor of approximately $100\times$ to the simulations compared to the global implementation. This approximately scales with the number of dislocation segments in the simulation box, so that a local treatment of emission incurs in an extra cost associated with a linear sweeping over all dislocation segments. This knowledge can guide further simulation campaigns when CPU time is of the essence.

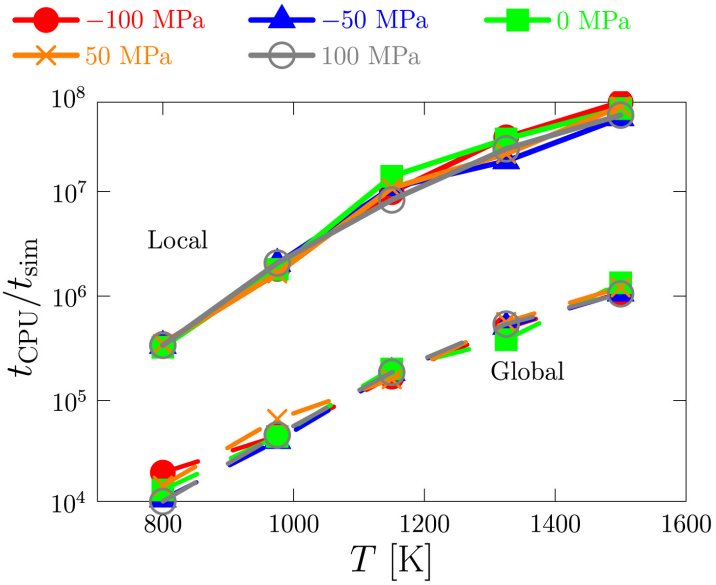

Figure B.13: Ratio of CPU time to simulated time for local and global vacancy emission implementations as a function of simulated temperature and pressure (with $Cv = C_0$).

B.3 Second-order stress effects on the osmotic force

Starting from the general expression for the osmotic force in eq. (2.20):

$$f^{\mathrm{os}} = \frac{bkT}{\Omega_a} \log \frac{C_v}{C_0} \tag{B.39}$$

one can refer C_v and C_0 to the *local* and *remote* concentrations near a dislocation core, such that the logarithmic term is expressed as $\log\left(C_{\mathrm{local}}/C_{\mathrm{remote}}\right)$. This converts the spatial uniformity of C_v and C_0 to the level of proximity to a dislocation where stress gradients can be felt by vacancies.

C_{local} and C_{remote} can be replaced by their time dependent solutions (see eq. (2.8)):

$$C_{\mathrm{local}}(\boldsymbol{x}, t) = \frac{1}{(4\pi D t)^{1/2}} \exp\left\{-\frac{(\boldsymbol{x} - \boldsymbol{u}t)^2}{4Dt}\right\}$$

and

$$C_{\mathrm{remote}}(\boldsymbol{x}, t) = \frac{1}{(4\pi D t)^{1/2}} \exp\left\{-\frac{\boldsymbol{x}^2}{4Dt}\right\}$$

Here we have assumed that vacancies near dislocations cores feel stress gradients and are subjected to a drift, while far away from them they do not. Inserting the above expressions into eq. (B.39) and operating:

$$f^{\mathrm{os}} = \frac{bkT}{\Omega_a}\log\frac{C_{\mathrm{local}}}{C_{\mathrm{remote}}} = \frac{bkT}{\Omega_a}\log\frac{\exp\left\{-\frac{(\boldsymbol{x}-\boldsymbol{u}t)^2}{4Dt}\right\}}{\exp\left\{-\frac{\boldsymbol{x}^2}{4Dt}\right\}} = \frac{bkT}{\Omega_a}\left[\frac{-(\boldsymbol{x}-\boldsymbol{u}t)^2+\boldsymbol{x}^2}{4Dt}\right] = \frac{bkT}{\Omega_a}\frac{\boldsymbol{u}\boldsymbol{x}}{2D} \tag{B.40}$$

where second order terms in time have been discarded. Replacing $\boldsymbol{u}$ by its expression in eq. (2.14), and assuming that $\|\boldsymbol{x}\| \approx \delta x$:

$$\boldsymbol{u} \approx \frac{D\Omega_a}{3kT}\nabla \mathrm{Tr}(\boldsymbol{\sigma}) \tag{B.41}$$

leads to:

$$f^{\mathrm{os}} \approx \frac{b^2}{3}\frac{\partial \sigma}{\partial x} \tag{B.42}$$

where it has been further assumed that the vacancy diffusion length is on the order of the Burgers vector's modulus.

Using the steady-state solution of the drift-diffusion equation leads to the same expression, assuming perfect vacancy absorbance at the dislocation core, and a uniform remote vacancy concentration of C_0, i.e. [61]:

$$C^{\mathrm{core}}(x) = C_0\left(\frac{\exp\left\{\frac{ux}{D}\right\}-1}{\exp\left\{\frac{u\ell}{D}\right\}-1}\right)$$

Accordingly, the osmotic force becomes:

$$f^{\mathrm{os}} = \frac{bkT}{\Omega_a}\left(1-C^{\mathrm{core}}/C_0\right) \approx \frac{bkT}{\Omega_{\mathrm{rel}}}\left(\frac{\exp\left\{\frac{ux}{D}\right\}-1}{\exp\left\{\frac{u\ell}{D}\right\}-1}\right) = \frac{bkT}{\Omega_a}\left(1-\frac{ux/D}{\exp\left\{\frac{u\ell}{D}\right\}-1}\right) \tag{B.43}$$

where we have used a first-order expansion of the exponential, $x \equiv \delta x \approx 0$, and ℓ is a screening distance. This results in the expression:

$$f^{\mathrm{os}} = \frac{bkT}{\Omega_a}\frac{u}{D}\left(\ell - \delta x\right) \tag{B.44}$$

which is identically equivalent to eq. (B.42) when $\delta x \approx b$ and $\ell \approx 2b$, both reasonable values for both parameters. This shows that when stress gradients are operative, the osmotic force is also subjected to a mechanical bias.

Chapter 3

Parallelization of Discrete Stochatic Vacancy Model

The basis for the method developed here is the model for dislocation climb proposed by McElfresh *et al.* [50], which relies on the coupling of a discrete vacancy kinetic model with standard DDD. Below, we provide a brief description of the vacancy diffusion model and the dislocation-vacancy coupling approach. Vacancy transport is governed by the drift-diffusion equation:

$$\frac{\partial C}{\partial t} = D_v \nabla^2 C - \boldsymbol{u} \cdot \nabla C \ , \tag{3.1}$$

where C is the vacancy concentration at position $\boldsymbol{x}$ and time t, $\boldsymbol{u}$ is the drift velocity vector, D_v is the vacancy diffusivity, and ∇^2 is the Laplacian. The general solution to the above expression in 3D can be shown to be:

$$C(\boldsymbol{x}, t) = (6\pi D_v t)^{-\frac{1}{2}} \exp\left\{ -\frac{(\boldsymbol{x} - \boldsymbol{u}t)^2}{4 D_v t} \right\} \ , \tag{3.2}$$

which can be used as a 'wave function' (spatial probability distribution function) of the vacancies and sampled accordingly to generate point-wise vacancy distributions in the system. The general expression for the drift velocity of a point defect in an isotropic medium can be shown to be:

$$\boldsymbol{u} = -\frac{D_v}{kT} \nabla E(x) \ , \tag{3.3}$$

where the term $\nabla E(x)$ reflects the spatial variation of the defect's formation energy in the presence of elastic fields. For vacancies, which introduce hydrostatic lattice distortions only, the expression can be simplified to:

$$\boldsymbol{u} = \frac{D_v}{kT}\frac{\Omega_{\text{rel}}}{3}\nabla \text{Tr}(\boldsymbol{\sigma}) \ , \tag{3.4}$$

where Ω_{rel} is the vacancy relaxation volume, k is the Boltzmann constant, and $\text{Tr}\left(\boldsymbol{\sigma}(\boldsymbol{x})\right) = \sigma_{kk}$. Thus, when embedded in an elastic medium containing dislocations, the stress tensor $\boldsymbol{\sigma}(\boldsymbol{x})$ provides the local driving force in the form of a diffusion drift that depends on the gradient of its hydrostatic components. The evolution of the vacancy subsystem is then simulated by a kinetic Monte Carlo (kMC) algorithm that accounts for elastic drift effects on vacancy diffusion. In this way the vacancy transport module is self-consistently linked to the DDD module. Note however that the present kMC module does not account for vacancy-vacancy interactions, so it is not intended to capture vacancy clustering or vacancy cluster dissociation.

Diffusion of the discrete vacancies is governed by the expression in eq. (3.4). We define the vacancy diffusivity as $D_v = zfb^2\nu(T)$, where $z = 8$ is the coordination number of the bcc lattice, $f \approx 0.8$ is a correlation factor, and b is the jump distance, which is identical to the Burgers vector magnitude. The temperature dependent jump frequency is defined as $\nu(T) = \nu_0 \exp\left(-E_m/kT\right)$, where ν_0 and E_m are the attempt frequency and vacancy migration energy, k is Boltzmann's constant, and T is the absolute temperature. Here it is worth emphasizing that eq. (3.4) represents an implicit problem that necessitates a self-consistent solution for the vacancy jump distance because of the influence of the local stress gradient on the drift velocity. To solve this we set a maximum jump distance, $\delta x_{\text{vac}}^{\max}$, and randomly sample jumps until the appropriate timestep distribution conditions are met ($\delta x_{\text{vac}}^{\max}$ must satisfy a shifted Gaussian random walk) [50]. The $\delta x_{\text{vac}}^{\max}$ parameter is on the order of the Burgers vector magnitude b and is discussed in more detail in Section 3.1.3.

In addition to diffusion, vacancies can be removed from or inserted into the system by absorption and emission processes, respectively. The rates of absorption or emission of vacancies are calculated by considering a cylindrical volume around a dislocation segment i of size $V_i = \pi b_i^2 l_i$, where $b_i = \|\boldsymbol{b}_i\|$ and l_i are the magnitude

of the Burgers vector $\boldsymbol{b}_i$ and the segment length, respectively. The integer-valued expression for the local rate of emission of vacancies can then be adapted from the standard expression given by Friedel [98] as:

$$\dot{N}_i = \left(\frac{2\pi l_i}{b_i}\left(1 - \frac{\boldsymbol{t}_i \cdot \boldsymbol{b}_i}{b_i}\right)\right)\nu(T)\left(1 - \frac{N_i}{\rho_a V_i \exp\left(-\frac{H_f}{kT}\right)}\right) \ , \tag{3.5}$$

where N_i is the number of vacancies emitted, $\boldsymbol{t}_i$ is the segment's normalized line tangent, ρ_a is the atomic density, and $H_f = E_f^o - \frac{1}{3}\mathrm{Tr}(\boldsymbol{\sigma})\Omega_{\mathrm{rel}}$ is the stress-sensitive vacancy formation enthalpy. During the kMC evolution, each dislocation segment has a unique emission rate that is added to the list of event rates to sample in each kMC iteration. For a complete derivation of these expressions, the reader is referred to the original work [50].

Absorption (emission) of vacancies by a dislocation segment i results in climb along its normal direction by an amount:

$$h_i = \pm\frac{N_i \Omega_a b_i}{l_i |\boldsymbol{t}_i \times \boldsymbol{b}_i|^2} \ , \tag{3.6}$$

where Ω_a is the atomic volume. h_i is positive (negative) if vacancies are absorbed (emitted), hence the '$\pm$' sign. Absorption occurs once a vacancy diffuses within the capture radius, R_{capt}, of a segment.

As indicated in Section 1, we will compare the predictions furnished by our discrete kMC/DDD approach with other existing climb formulations. These are briefly described in C.1. It is also useful to emphasize that physical constants such as temperature and Burgers vector magnitude are shared between the vacancy and DDD procedures for physical consistency.

3.1 Parallelization of the kMC/DDD coupled approach

The vacancy-transport and emission module described in Section 3 can be directly applied to any serial three-dimensional DDD code to carry out climb-enabled

simulations. However, many modern DDD codes have been improved to take advantage of the time efficiency and scale benefits of parallelized computing [99–101]. Accessibility to large-scale simulations has the obvious benefit of exploring near-bulk systems and large-network phenomena such as strain hardening [102–104]. Thus, modifications are required to parallelize the discrete kMC vacancy transport module so that it can operate in a parallel DDD environment. The developments undertaken to achieve such an extension are explained in the following subsections.

3.1.1 Parallelization of the kMC module

Rejection-free Monte Carlo methods such as the kMC model used here are efficient algorithms for carrying out discrete event simulations. However, they are inherently serial because time evolves in a stochastic manner that makes the determination of the next timestep unpredictable. For that reason, a direct implementation of the kMC method into a parallel environment based on a spatial decomposition results in asynchronous kinetics. This presents a number of challenges associated with processor-processor communication and with event causality [105, 106]. To solve these intrinsic difficulties, Martinez *et al.* developed the *synchronous parallel* kMC (spkMC) method [78,107] that makes use of 'null' events that can be used to equalize the total rates in each spatial domain. Null events represent system 'inactivity' and thus have no effect on the kinetic evolution. For that reason, they can be flexibly used to synchronize time by defining an identical rate in all domains and advancing time by the average of the exponential distribution defined by such rate.

With this a global timestep dt_{spkMC} is thus obtained for the parallel kMC module, which can then be made consistent with the timestep in DDD in a manner that will be described later. Because the spkMC system is only handling vacancies in this application we will refer to dt_{spkMC} as δt_{vac}. The implementation of the spkMC method to evolve the vacancy climb module in `ParaDiS` is described below.

1. First, we calculate the total rate for each subdomain k as the sum of the individual vacancy diffusion, r_{ik}, and vacancy emission, r_{jk}, rates in the corresponding simulation subvolume V_k containing n_k and l_k vacancies and

dislocation segments, respectively:

$$R_k = \sum_i^{n_k} r_{ki} + \sum_j^{l_k} r_{kj} \ . \tag{3.7}$$

This is subjected to the mass and volume conservation rules:

$$N = \sum_i^K n_i, \ L = \sum_i^K l_i, V = \sum_k^K V_k \ ,$$

where N, L are the total number of vacancies and dislocation segments in the simulation volume V, and K is the total number of subdomains (processors).

2. The maximum rate, $R_{\max}$, is then defined for all subdomains as:

$$R_{\max} = \max_{k=1,..,K} \{R_k\} \ . \tag{3.8}$$

3. The null-rate for each subdomain can be calculated as:

$$r_{k0} = R_{\max} - R_k \ . \tag{3.9}$$

Thus, a null event is added to the event list in each subdomain and sampled with a probability $r_{k0}/R_{\max}$.

4. If a vacancy event is sampled, time is advanced by an amount $\delta t_{vac} \equiv R_{\max}^{-1}$ and the corresponding event is executed. Else, if a null event is sampled, the configuration of the system is left untouched but time is still evolved by the same amount $R_{\max}^{-1}$.

3.1.2 DDD and kMC timestep alignment

Instead of using a standard 'master/slave' approach to couple the DDD and kMC modules, here we opted for treating a DDD relaxation as an independent stochastic event. To do this, *a priori* knowledge of the DDD timestep is necessary as a rate input for the stochastic selector. We adopted a Heun multi-stepping time integration scheme inspired from the subcyling approach introduced in [108], and which utilizes a pre-defined timestep size, δt_{DDD}. During time-integration, dislocation nodes are evolved with no change of the topology via subsequent iterations

of size smaller than δt_{DDD} (determined by the specified error tolerance) until the full timestep is reached, after which dislocation collisions are handled using the retroactive collision algorithm [108]. The impact of δt_{DDD} on the simulations will be studied in Section 3.1.3.

The basic kMC time synchronization algorithm operates as follows:

1. Retrieve the timesteps for both the DDD and vacancy modules. Find δt_{vac} using the procedure described in Section 3.1.1. For DDD use the *a priori* assigned δt_{DDD}.

2. Convert the timesteps to rates such that $R_t^{\mathrm{DDD}} = \delta t_{\mathrm{DDD}}^{-1}$ and $R_t^{\mathrm{vac}} = \delta t_{\mathrm{vac}}^{-1}$. Select either a DDD step or a vacancy step with probabilities given by:

$$p_{\mathrm{DDD}} = \frac{R_t^{\mathrm{DDD}}}{R_t^{\mathrm{DDD}} + R_t^{\mathrm{vac}}} , \tag{3.10}$$

$$p_{\mathrm{vac}} = 1 - p_{\mathrm{DDD}} . \tag{3.11}$$

3. Execute the action that was selected to evolve the state of the system. For example, if the vacancy module was selected then each domain executes a vacancy migration, vacancy emission, or null-event (no change of state). If a DDD step is selected then evolve the positions of the dislocation segments according to the multi-stepping algorithm. Calculate all outputs for both the vacancy and DDD modules.

4. Increment the system clock by a global timestep given by:

$$\delta t_{global} = -\frac{\ln \zeta}{R_t^{\mathrm{DDD}} + R_t^{\mathrm{vac}}} , \tag{3.12}$$

   where $\zeta \in (0, 1]$ is a uniform random number. The procedure then returns to step 1 and repeats until the maximum number of iterations is reached.

A general process flow outline for the execution of DDD-coupled discretized climb model is illustrated in Figure 3.1.

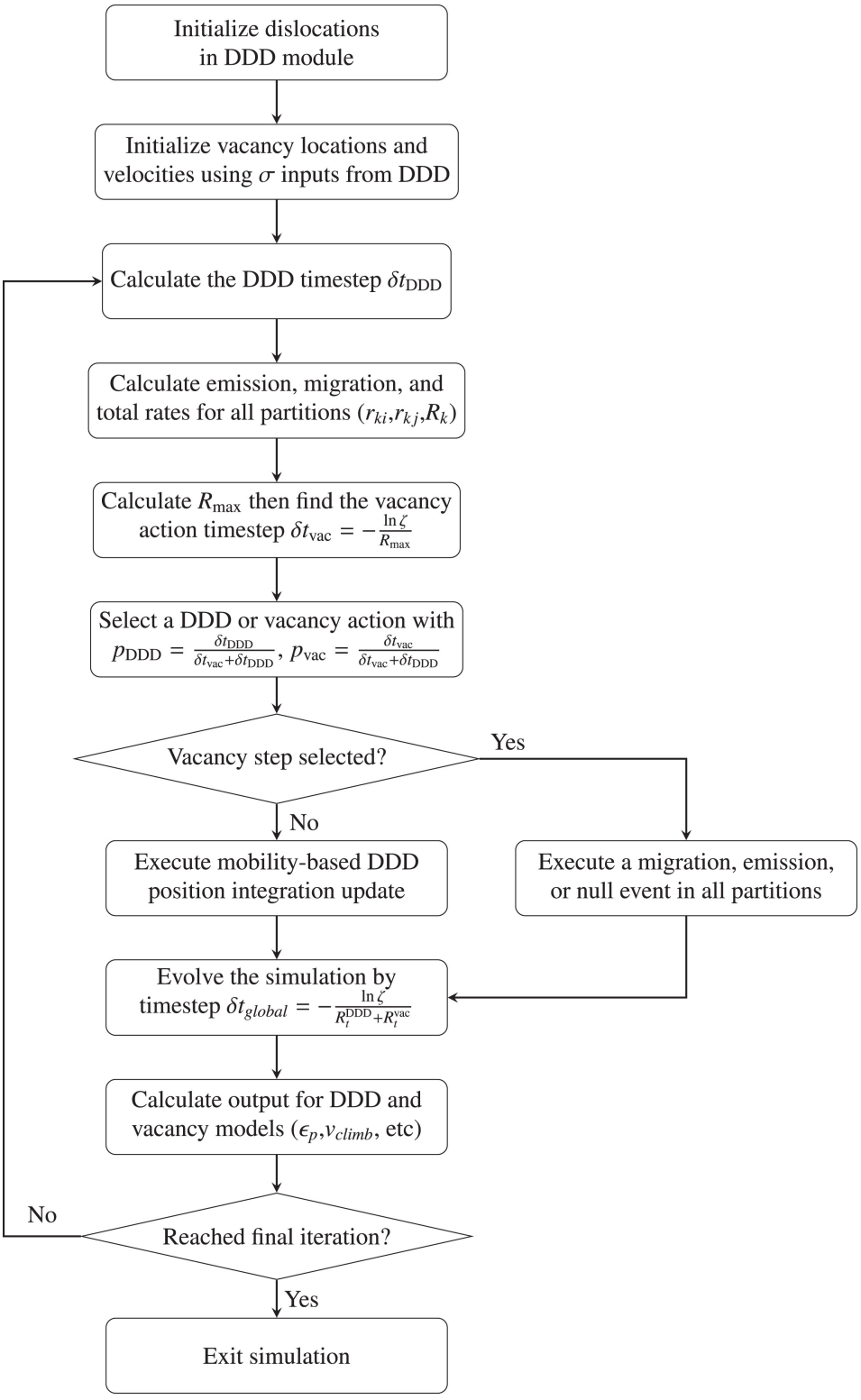

Figure 3.1: Process flow of the implementation of the parallel kMC/DDD method for discrete vacancy transport and dislocation climb.

3.1.3 Numerical analysis of the kMC/DDD coupled approach

Relationship between the DDD and kMC timesteps

The integration timestep in a DDD simulation, δt_{DDD}, is typically limited by the maximum admissible displacement distance traveled by a dislocation segment in order to properly treat dislocation segment collisions and reduce the truncation error [109]. Discussion of δt_{DDD} has a particular importance in this study because the DDD timestep must be assigned *a priori* such that during each simulation iteration it may be used as an input to the global kMC selection algorithm. To assess the consistency of our coupling approach and the effects of the magnitude of δt_{DDD}, simulations with identical starting conditions, consisting of two $40b$ prismatic loops contained in a simulation box $100b$ in size, were run for 40,000 iterations using fixed δt_{DDD} values of 10^{-6}, 10^{-8}, 10^{-10}, and 10^{-12} s. The median vacancy rate R_t^{vac} for all simulations was 5.8×10^6 s^{-1}. An artificially high drag coefficient was used for glide to ensure the stability of the loops during the use of the larger timesteps. Histograms with normalized frequency counts of the simulation timesteps are presented in Figure 3.2(a). As expected, all timestep distributions have a log-normal distribution. The modes of the first three distributions ($\delta t_{\mathrm{DDD}} \leq 10^{-8}$ s) appear to be equispaced in the figure, suggesting a linear correlation between the DDD and the global timesteps as corroborated by eq. (3.12). The subsequent decrease in average global timestep above $\delta t_{\mathrm{DDD}} = 10^{-8}$ s can be attributed to the fact that, as the DDD timestep approaches the value given by the inverse of the vacancy rate, the global timestep converges to the latter (which is unaffected by the DDD timestep). This effect is captured in Figure 3.2(b) (with an additional data point for $\delta t_{\mathrm{DDD}} = 10^{-5}$ s). A linear correlation between the global and DDD timesteps is clearly established up to $\delta t_{\mathrm{DDD}} = 10^{-8}$ s, after which the global timestep converges to the value set by the inverse of R_t^{vac}, i.e., $\approx 1.7 \times 10^{-7}$ s. These results show that vacancy events (diffusion/emission events) effectively set an upper limit on the timestep of the entire simulation with a value equal to the inverse of R_t^{vac}.

It is important to emphasize that while δt_{DDD} influences the frequency of se-

lection between the dislocation dynamics and vacancy steps, the overall kinetics of simulation remains the same. In other words, given the same total simulation time, we expect, on average, the same microstructural evolution for reasonable values of δt_{DDD}. To demonstrate this, simulations using two $20b$ loops in a $100b$ cube were evolved to 2.0 ms of simulation time using δt_{DDD} values of 10^{-6}, 10^{-8}, and 10^{-10} s. Figure 3.2(c) gives a histogram of the vacancy event rates in each case, demonstrating the absence of any kinetic bias when δt_{DDD} is varied. Moreover, the total number of vacancy events (integral of each histogram) executed is roughly the same in all cases. In the graph, the R_t^{vac} values have been partitioned between diffusion dominated and emission dominated events to illustrate that the emission rates are typically orders of magnitude larger than the diffusion rates.

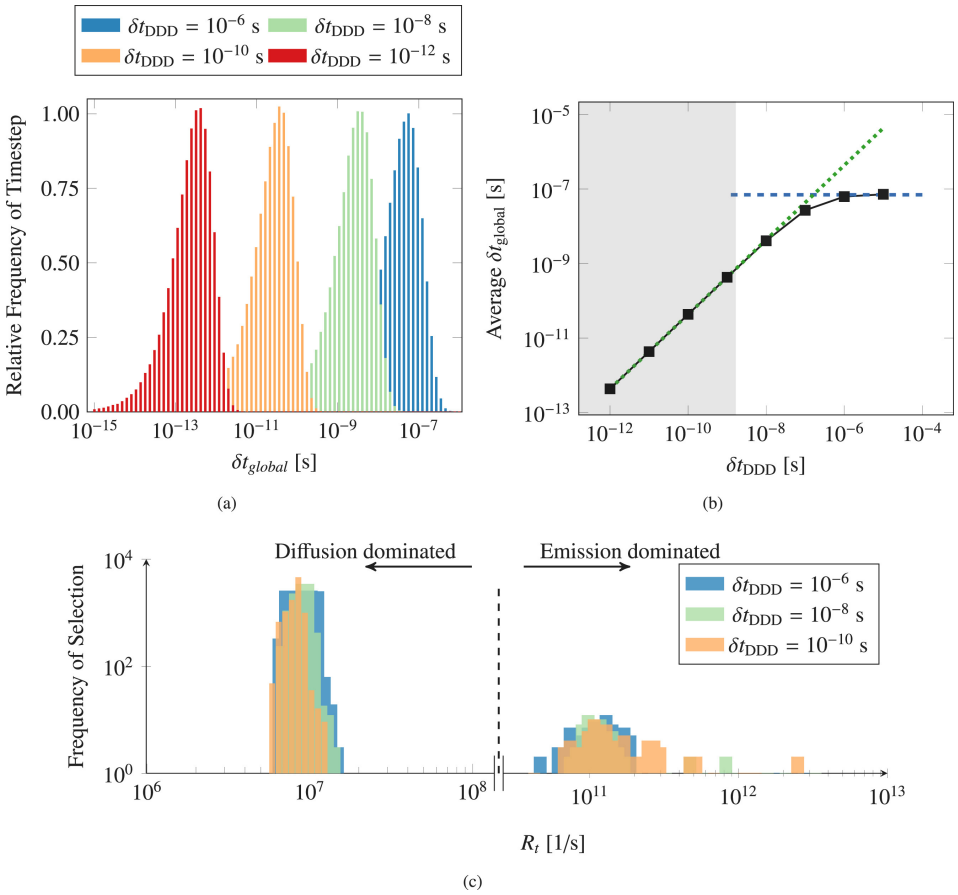

Figure 3.2: (a) Relative frequency of the global timestep selected in the joint kMC/DDD model for various $\delta t_{\text{max}}^{\text{DDD}}$ values. (b) Average simulation timestep as a function of δt_{DDD}. The blue dashed line illustrates the convergence of the timestep to being vacancy-dominated. The green dotted line illustrates the kMC timestep progression if no vacancies were present. Each simulation was run for 40,000 iterations with two $40b$ loops in a $100b$ cubic box. The gray shaded box indicates the typical range of acceptable δt_{DDD} to avoid collision and truncation errors. (c) Histogram displaying the frequency in occurrence of different R_t^{vac} values when a vacancy step is selected for δt_{DDD} values of 10^{-6} s (blue), 10^{-8} s (green), and 10^{-12} s (orange). All simulations we performed using an identical starting condition of two loops in a $100b$ cubic box at 1200 K. All simulations were run for an equivalent simulation time length of 2.0 ms.

As well, by virtue of eq. (3.10), it is expected that, as δt_{DDD} increases, the likelihood of sampling and executing vacancy events will grow accordingly. This increase can be quantified in terms of the vacancy event ratio (i.e., the proportion of iterations in which a vacancy event is selected rather than a DDD event) and

its dependence on δt_{DDD}. The results are given in Figure 3.2(b) (on the right-side axis). The exponential relationship displayed by the ratio of vacancy events as a function of δt_{DDD} is a consequence of eq. (3.10) gradually converging to the expression $p_{\text{vac}} = \frac{1}{1+1/\delta t_{\text{DDD}}}$, i.e., by reducing R_t^{vac} to unity.

Vacancy population subevolution

Similarly to how δt_{DDD} determines the upper limit of the kinetics for the dislocation evolution, the jump parameter $\delta x_{\text{vac}}^{\text{max}}$ and the vacancy concentration set the upper limit of the kinetics for vacancy diffusion. Mathematically:

$$R_t^{\text{vac}} < \frac{D_v}{\left(\delta x_{\text{vac}}^{\text{max}}\right)^2} \ .$$

Thus, decreasing $\delta x_{\text{vac}}^{\text{max}}$ enforces smaller vacancy jumps, and as such, higher R_t^{vac} values. It then follows that, all else being equal, $\delta x_{\text{vac}}^{\text{max}}$ decreases as the vacancy event ratio increases. This trend is displayed in Figure 3.3(a). As well, increasing the vacancy concentration has a direct positive correlation on R_t^{vac}, as shown in Figure 3.3(b).

Lastly, the effect of simulation conditions on the null event ratio (fraction of null events relative to total events) is worth studying. This is because one would ideally want to limit this ratio in order to maintain a high simulation efficiency. As Figure 3.3(c) shows, the null event ratio naturally decreases with $\delta x_{\text{vac}}^{\text{max}}$ due to a higher ratio of diffusion to emission events. A more thorough study of how the null event ratio is affected by other simulation variables is provided in C.2.

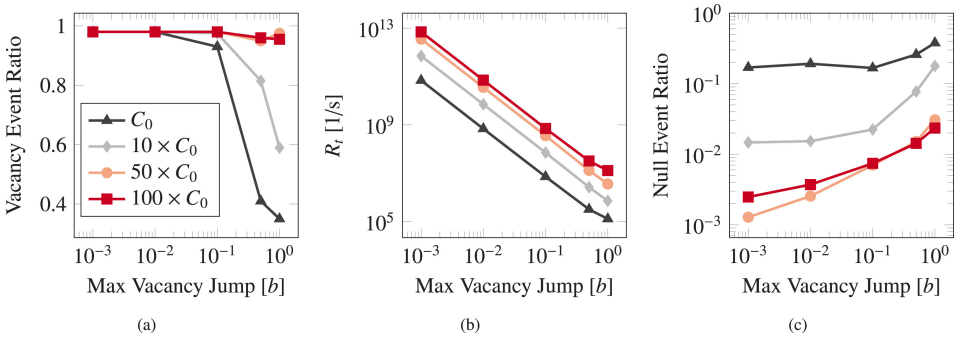

Figure 3.3: The (a) vacancy event ratio, (b) total vacancy rate, and (c) null event ratio, as a function of the maximum allowed jump distance.

3.1.4 Serial/parallel cross-verification

A demonstration of defect evolution dynamics is necessary to verify the implementation of the serial kMC algorithm [50] in a parallel setting. To this end, a simulation with five $20b$ loops in a $100b$ box was evolved using the serial method as well as the parallel code with 2, 4, 8, 16, and 27 processors. The vacancy absorption and emission rates as a function of the simulation time are given in Figure 3.4(a) and 3.4(b), respectively. Beyond an initial transient, all rates gradually converge to values within 25% of one another. This is consistent with the intrinsic accuracy furnished by the spkMC algorithm [78] of the parallel method compared to the serial ($n = 1$) case.

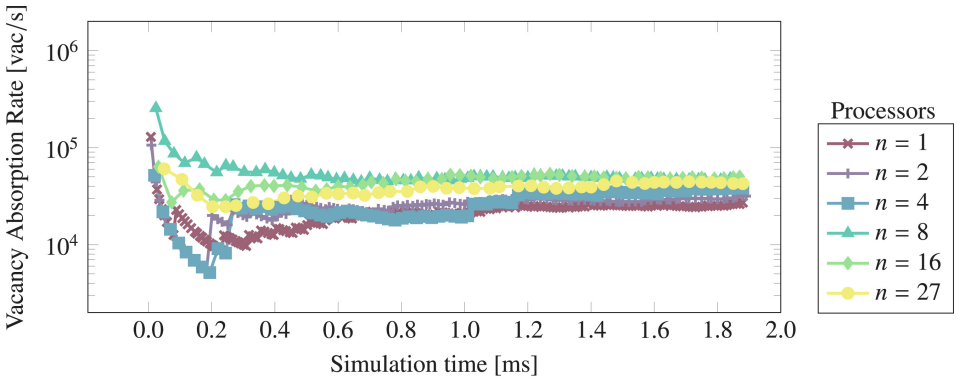

(a)

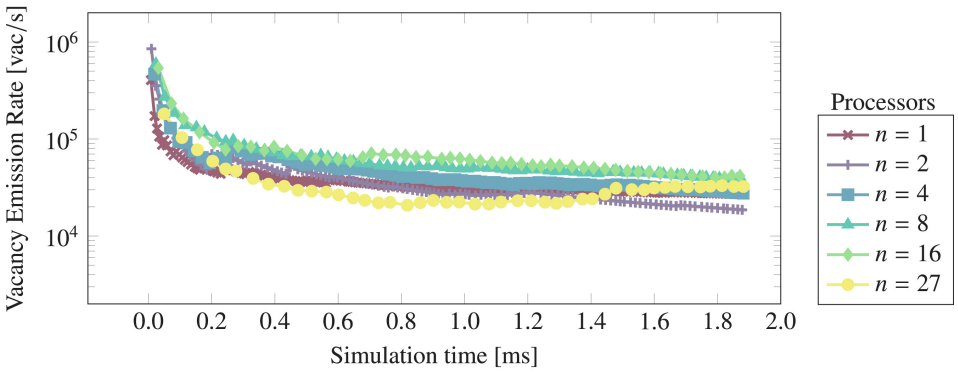

(b)

Figure 3.4: Evolving average (a) absorption and (b) emission rate as a function of time using an increasing number of processors. Both emission and absorption rates show good agreement across the serial and parallel runs. Simulations were performed with five $20b$ loops in a $100b$ cubic volume.

3.1.5 Parellel scalability

First, we examine the strong scaling behavior (i.e., same problem size simulated with increasing numbers of processors) of the kMC module as implemented here. For this test the computation time for `ParaDiS` was ignored because the scalability for the `ParaDiS` library has been well-documented elsewhere [99]. For this, a simulation was run with with 9000 vacancies and 200 loops that were $200b$ in diameter. The simulation was contained in a $200b \times 200b \times 200b$ cube. A snapshot of the simulated volume is given in Figure 3.5(a). The speedup, measured as n times the CPU time of the serial case relative to the CPU time of a case with n processors is plotted in Figure 3.5(b). The speedup follows a logarithmic increase typical of communication-limited algorithms so common in MPI-type implementations. The speedup gained by parallelization is sufficient to study larger scale samples in dislocation dynamics. A more thorough discussion of the scalability data is provided in C.2.3. It is also worth noting that the introduction of vacancies in DDD undermines `ParaDiS`'s native load-balancing scheme whereby subdomains are dynamically re-balanced as a function of computation time. A more rigorous load balancing procedure may need to be developed for the combined kMC/DDD model that considers both dislocations and vacancies (or R_t, depending on the optimization goal) of each subdomain. These improvements will be considered in future work.

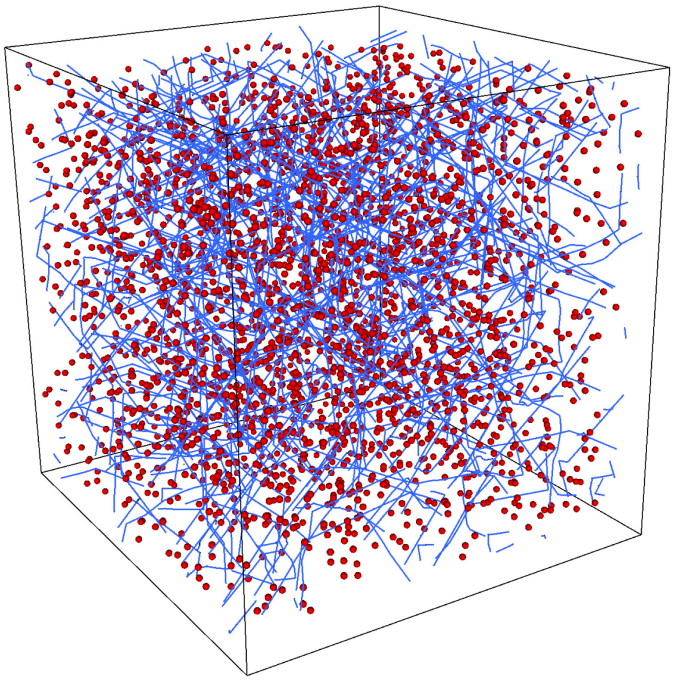

(a)

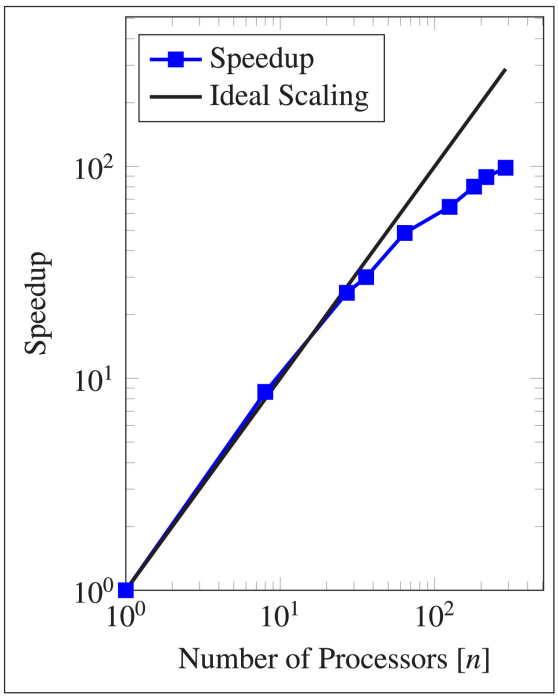

(b)

Figure 3.5: (a) Snapshot of the configuration used to measure strong scaling with both dislocation segments (in blue) and vacancies (in red) shown. (b) Speedup of the vacancy module as a function of the number of processors for a fixed simulation cubic volume $200b$ in size containing 200 dislocation loops of size $200b$ and 10,000 vacancies. The temperature was 1300 K. δt_{DDD} was set to 10^{-3}s to ensure that we were primarily probing the vacancy module execution time.

3.2 Applications and results

The approach presented in Sections 3, 3.1.1, and 3.1.2 was implemented in the `ParaDiS` code [34, 99]. All simulations were performed using bcc iron as model material. The relevant material constants used here are given in Table 3.1. Next we apply the method to a few selected scenarios that serve to demonstrate its robustness and generality. We start by comparing calculations of climb velocities with the present approach and existing models published in the literature.

Table 3.1: Material parameters for bcc Fe employed in this work.

Parameter	Symbol	Value	Units
Boltzmann's constant	k	8.615×10^{-5}	eV $\cdot$K^{-1}
Correlation factor	f	0.78	–
Burgers vector magnitude	b	0.25	nm
Atomic density	ρ_a	8.46×10^{22}	atoms/cm^3
Shear modulus	μ	52	GPa
Poisson's ratio	ν	0.29	–
Attempt frequency	ν_0	10^{12}	Hz
Vacancy formation energy	E_f^o	1.7	eV
Vacancy migration energy	E_m	0.66	eV
Atomic volume	Ω_a	0.77	b^3
Vacancy relaxation volume	Ω_{rel}	θ_v	Ω_a
Vacancy formation volume	Ω_{f}	$1 + \theta_v$	Ω_a
Vacancy volumetric strain	θ_v	-0.2	–
Capture radius	R_{capt}	3	b

3.2.1 Comparison of climb simulations with existing continuum methods

Here we compare calculations of climb velocities from several continuum approaches [25, 26]. These include the non-local Green's function formulation developed by Gu *et al.* [26], the analytical solutions by Mordehai *et al.* [25], and, when applicable, the simplified climb velocity of a circular prismatic loop under its own self stress [110] (labeled as "Numerical Solution" in the plots):

$$v_{cl} \approx \frac{\mu D_v C_0 \Omega_a}{2(1-\nu) R_{loop} kT} \ , \tag{3.13}$$

where μ and ν are the shear modulus and Poisson's ratio, R_{loop} is the radius of the loop, and $C_0 = \exp\left(-E_f^o/kT\right)$ is the vacancy concentration. The climb velocities calculated for a single prismatic loop as a function of temperature are given in Figure 3.6 at four different vacancy concentrations. As the figure shows, the data obtained with the present method is consistently two orders of magnitude lower than for the numerical and analytical cases. As well, the discrete method (this work) displays a slightly weaker temperature dependence than the continuum methods, but agrees with what was previously observed in ref. [50]. At this point, we do not judge the correctness of either approach based on this gap in quantitative agreement. Indeed, part of the purpose of this work is to demonstrate the differences in climb velocities between continuum models of vacancy diffusion and our discrete approach where fluctuations control vacancy kinetics. Interestingly, the method based on the Green's function also consistently underpredicts the results by the other continuum models. This may be also due to its nonlocal formulation, which admits fluctuations in vacancy fluxes dictated by the stress field of the dislocation configuration. We will get back to some of these issues in the Discussion section.

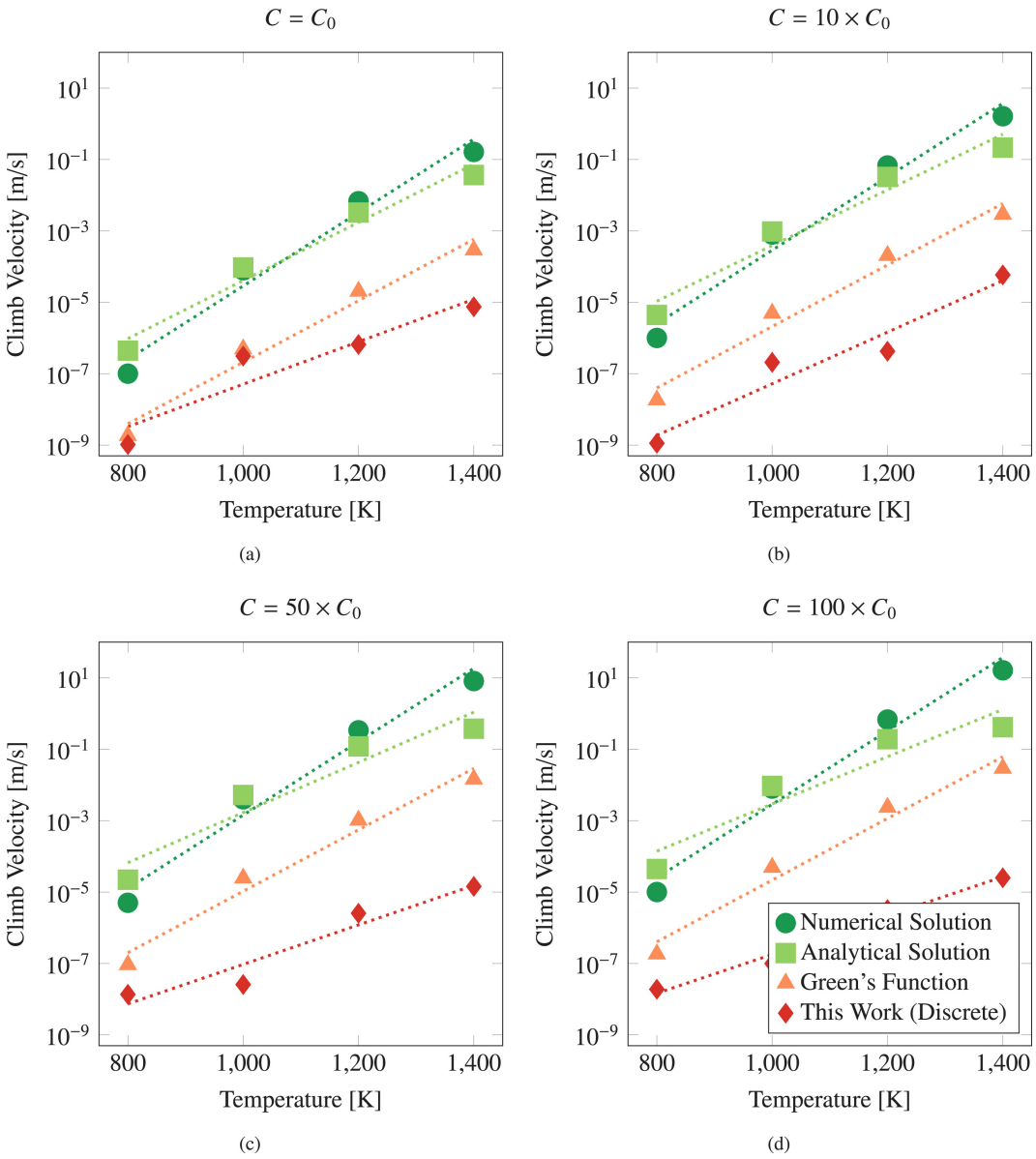

Figure 3.6: Climb velocity of a single prismatic loop obtained using the analytical method, the Green's function method, and the present discrete method. The estimation of the climb velocity given the numerical solution is also shown. The equilibrium vacancy concentration, C_0, was varied by (a) 1×, (b) 10×, (c) 50×, and (d) 100×. All simulations were performed for loops with a $30b$ radius at temperatures in the range of 800 to 1400 K.

3.2.2 Computational cost

Next we study the computational cost of the present approach relative to the continuum methods. To this end, we calculated the ratio of CPU time to simulated time, t_{CPU}/t_{sim}, for a fixed dislocation configuration of forty $30b$ loops in a $200b \times 200b \times 200b$ simulation box with varying temperatures and vacancy concentrations. A snapshot of the simulation volume at 1200 K is shown in Figure 3.7(a) along with the computational costs as a function of temperature (Figure 3.7(b)) and vacancy concentration (Figure 3.7(c)). For the discrete method, temperature has an exponential effect on computational cost while the vacancy concentration multiplier has a linear effect. Relative to the discrete method both continuum methods are temperature insensitive. The computational cost of the discrete method is comparable to that of the Green's function method at low temperatures ($\leq$ 1300 K) and low vacancy concentrations ($\leq \times 100$). However, for the problem size in question, the CPU overhead of the discrete method increases two to three-fold at the highest temperatures and vacancy concentrations.

The direct correlation between the computational cost and the number of vacancies can be attributed to the non-trivial calculations necessary for each additional vacancy including the overall rate contribution and absorption criterion (i.e., checking if vacancies are within the absorption distance). The breakdown of the normalized computational cost with increasing temperature is given in Figure 3.8. At low temperatures (fewer vacancies) inter-subdomain communication dominates the computation time. At higher temperatures the rate calculations and absorption events become the most computational intensive components.

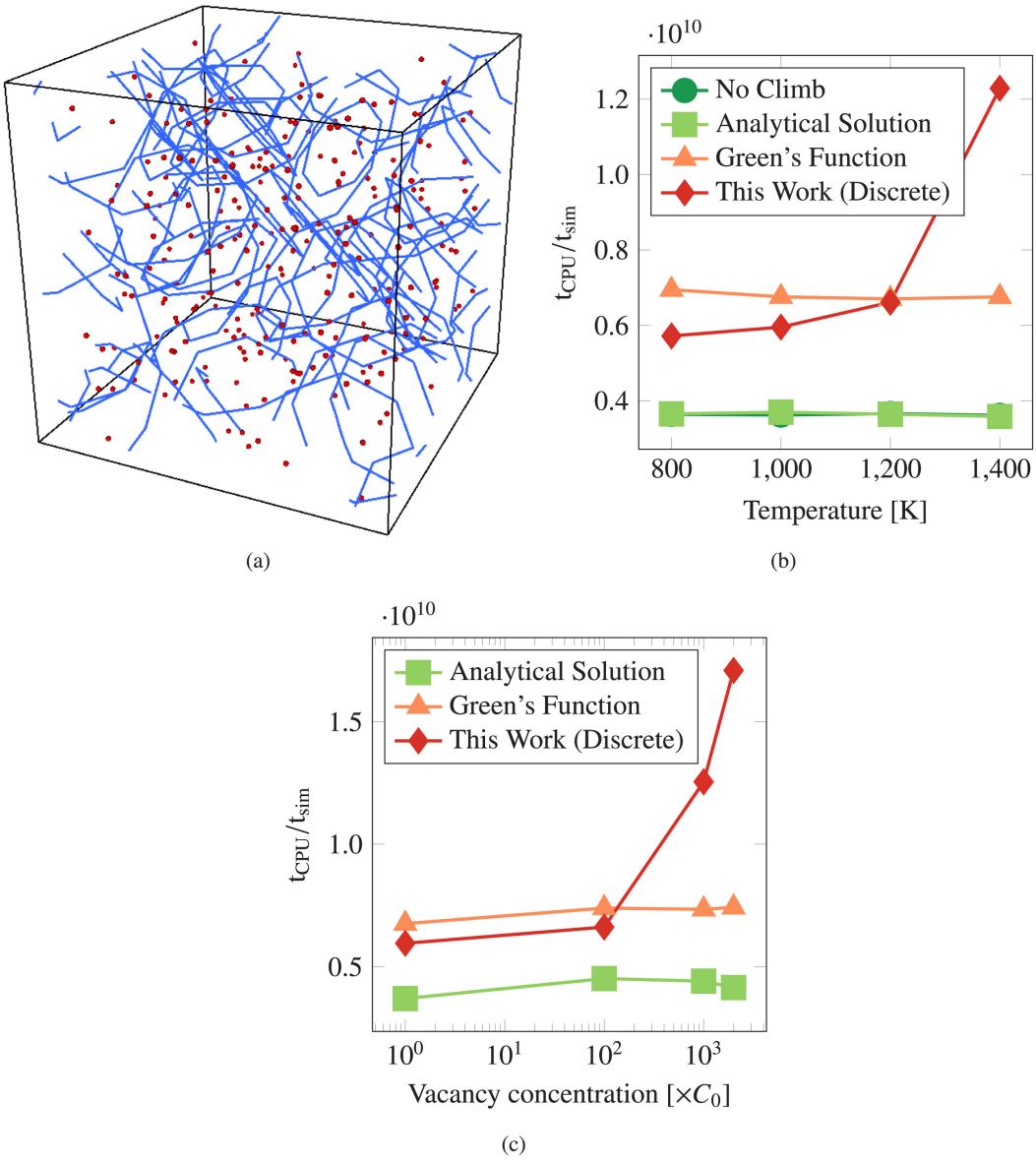

Figure 3.7: (a) Snapshot of the ParaDiS simulation volume with forty $30b$ dislocation loops (in blue) and vacancies (in red) at 1400 K. Ratio of CPU time to simulated time as a function of (b) temperature and (c) vacancy concentration for DDD simulations using the three climb methods along with a standard DDD simulation (no climb). Simulations were performed with 40 loops with a $30b$ radius and a vacancy concentration of $10 \times C_0$ for (b) and a temperature of 1000 K for (c).

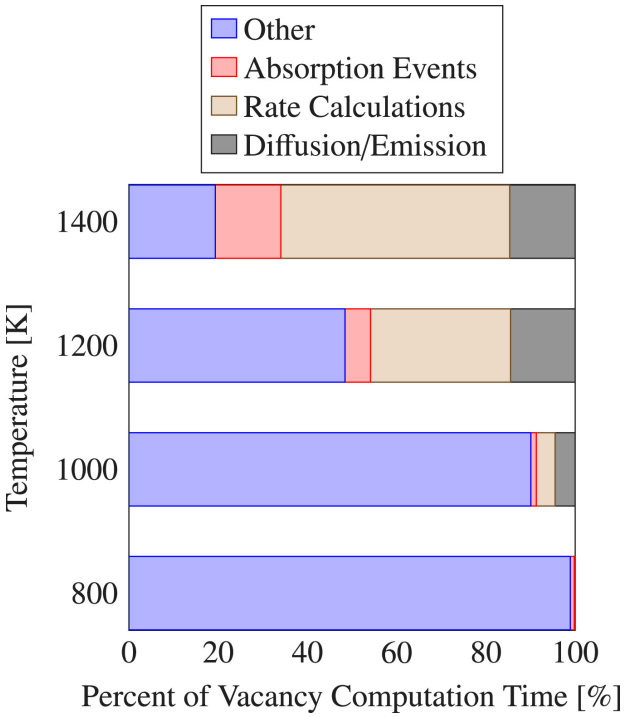

Figure 3.8: Normalized computation profile as a function of temperature. Tests were performed using 8 processors. "Other" refers to processes include initialization, null event calculations, and inter-domain vacancy transfers.

3.2.3 Applications of the discrete climb method to problems of interest in dynamic recovery

The full benefit of a discretized method of climb can be realized by application to highly local, stochastic, or spatially heterogeneous phenomena. Indeed, locally evolving point defects-dislocations structures are often dominated by jerky, stochastic movement that is difficult to capture using standard continuum solutions. To illustrate this, here we present two examples of deviation in behavior from the discrete and continuum methods that are of interest to the dynamic recovery of microstructures featuring prismatic loops. Additional areas to apply and expand the coupled defect model are discussed in Section 3.3.

Closing of a single prismatic loop

The closing of a prismatic loop provides one of the most basic, yet informative processes that can be used to compare the behavior in the discrete and continuum climb methods. An isolated prismatic loop will close via climb under its own self stress without the addition of a balancing osmotic force. Figure 3.9 shows the progress of an hexagonal $40b$-prismatic loop using both the Green's function continuum method and the discrete method. In this numerical experiment, the balancing force opposing shrinkage has been disabled: directly by explicitly turning off the osmotic forces in the continuum model, and by restricting vacancy emission in the discrete kMC/DDD method.

As the figures show, the continuum method (Figures 3.9(a)-(d)) demonstrates symmetric, smooth closure of the loop with a stable rate of change for the loop size. By contrast, the discrete method (Figures 3.9(e)-(h) results in a loop that is slightly contorted, with different sides climbing faster than others due to local variations in the vacancy population (the locations of the vacancies are shown in the figures to give a spatial reference). As well, the faster climb predicted by the continuum method agrees with what was previously observed in Section 3.2.1. To achieve the same amount of loop closure the discrete method is evolved for approximately 4 orders of magnitude longer in terms of simulated time – indicating that, in this case, the discrete approach predicts climb as a much slower physical phenomenon than in the continuum method. We note however that the discrete kMC approach only requires 16$\times$ the number of iterations of the continuum method to simulate the same amount of closure. This shows that the spkMC time integration method efficiently evolves the coupled DDD system such that large computational costs are not incurred to cover large time spans.

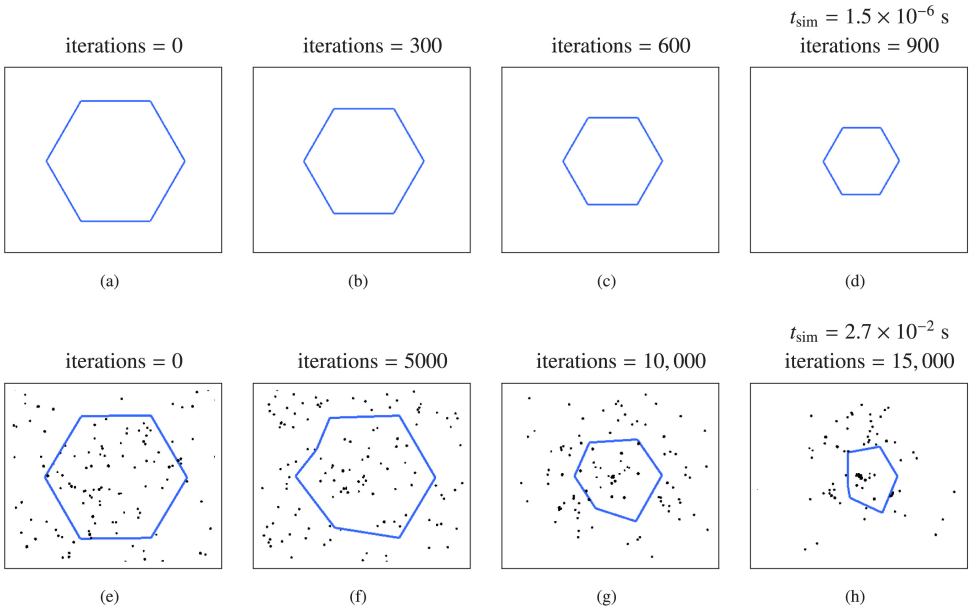

Figure 3.9: The closing of a single $40b$ prismatic loop using the (a)-(d) continuum and (e)-(h) discrete climb methods.

Discontinuous climb dynamics

The treatment of point defects as individual, discrete components of the simulation system requires that absorption and emission events are similarly executed as discrete events. Because of this, dislocation advancement through discretized climb does not necessarily occur in a smooth manner, as is modeled in the continuum methods. To further demonstrate this, Figure 3.10 provides the total area swept due to climb as a function of simulation time for an isolated loop under discrete and Green's function climb methods with a vacancy concentration of $50C_0$. The stochastic behavior of the discrete climb method are reflective of the natural local fluctuations in vacancy emission and absorption. Moreover, unlike the continuum method the discrete method can work 'against' the global driving force in the short term (i.e., by lowering the area swept out) while still satisfying the long-term thermodynamic bias of the system.

It is also useful to note that the discretized treatment of climb leads to a much higher instantaneous climb velocity during individual climb events when compared to the continuum approaches. This is visualized as the many small, yet steep fluc-

tuations in the 'distance climbed' evolution shown in Figure 3.10. The difference can be as high as 5∼6 orders of magnitude. For the most basic configurations (e.g., single loop) the continuum methods advance segments with smooth steps in space such that the instantaneous climb velocity (i.e., climb velocity measured at each simulation iteration) and long-term average climb velocity are essentially equivalent. The instantaneous metrics for discrete climb, on the other hand, can be substantially larger than the long-term average because each emission/absorption event is an instantaneous trigger associated with a discrete local jump in a segment position. This behavior is, of course, averaged out when calculating the effective climb velocity because the vast majority of simulation iterations do not involve any absorption/emission events (see Figure 3.2).

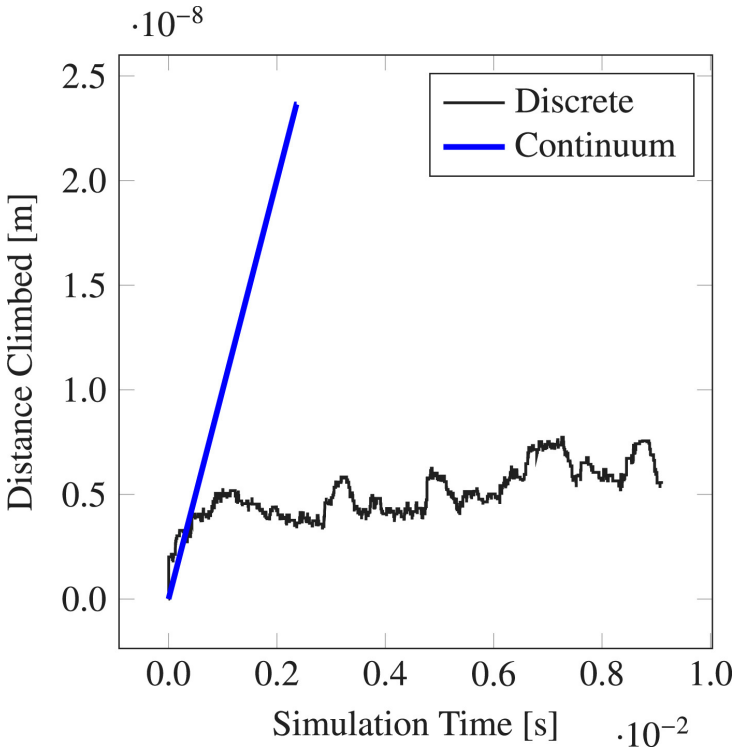

Figure 3.10: Distance climbed using the discrete method (black) and the Green's function method (blue).

Another phenomenon that is observed during discrete climb is localized burst-like events during which a segment, or neighboring segments, traverse a relatively large distance in a short period of time. An example is given in Figure 3.11, where

a segment rapidly absorbs 12 vacancies and displaces a commensurate amount. This behavior is typically driven by a segment moving in a region with a high localized concentration of vacancies and immediately absorbing them and climbing. Spatially heterogeneous point defect distributions can result from extrinsic mechanisms (e.g., irradiation damage cascades) or internal elastic/concentration gradients such that fluctuations in local plasticity can be expected. This is something that is not captured by continuum methods due to the prescribed smooth fluxes.

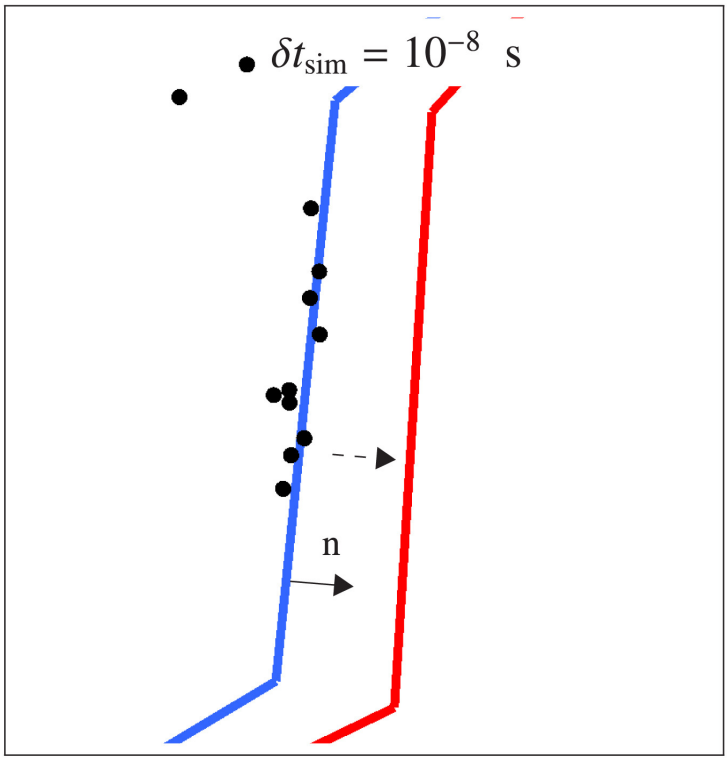

Figure 3.11: Dislocation segment before (blue,left) and after (red,right) absorbing 12 vacancies during a climb "burst" caused by a pocket of vacancies. The climb direction for the segment is denoted as n.

Vacancy decoration of dislocation loops

The treatment of vacancies as individual point defects has the benefit of being able to observe collective vacancy motion as a response to dislocation structures. The local stress fields created by dislocations are spatially complex and highly

directional such that point defect motion responds to certain dislocation features. This behavior is not captured in smooth-flux continuum approaches. By way of example, time-evolved snapshots of the vacancy population around isolated and immobilized vacancy and self-interstitial prismatic loops are given in Figures 3.12 and 3.13, respectively. A contour map of the hydrostatic stress is overlaid on the figures for reference.

For the vacancy loop, the vacancies approach the center loop on a path perpendicular to the habit plane, avoiding the tensile pressure regions around the edge of the loop. Conversely, as vacancies approach the interstitial loop they arrange themselves along a path perpendicular to the habit plane, avoiding the compressive pressure regions above and below the loop. To the best of our knowledge, spatial defect information has not been accessible through defect-coupled dislocation dynamics studies. Preferential diffusion pathways of point defects as a function of large, complex dislocation networks is a largely untapped area of study now accessible through this scalable approach. A follow-up study will purely focus on the spatial distribution and decoration of vacancies on prismatic loops.

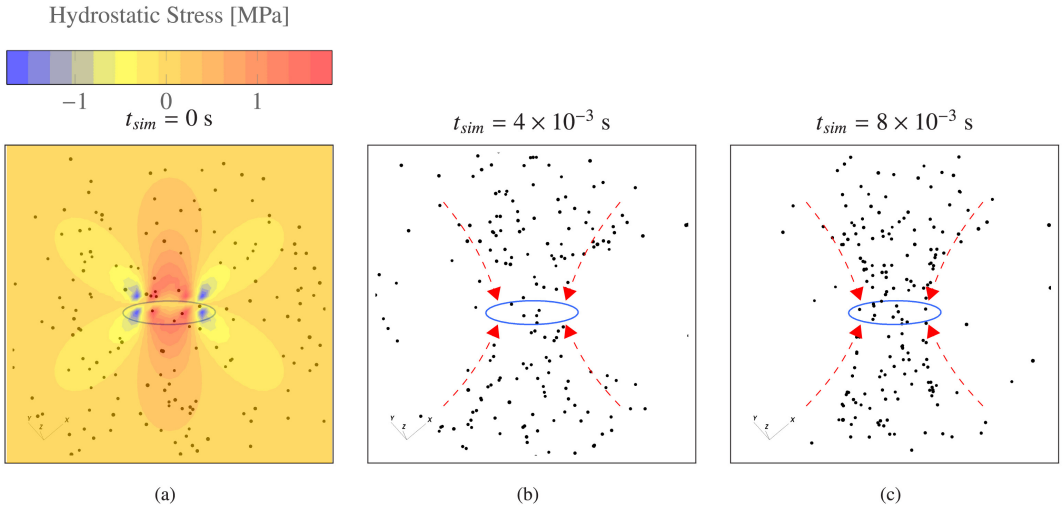

Figure 3.12: Snapshots of vacancy positions for a $20b$ immobilized vacancy loop from $t_{sim} = 0$ s to $t_{sim} = 8 \times 10^{-3}$ s. The vacancies preferentially approach the loop in a path perpendicular to the habit plane by forming a 'cone' above and below the loop.

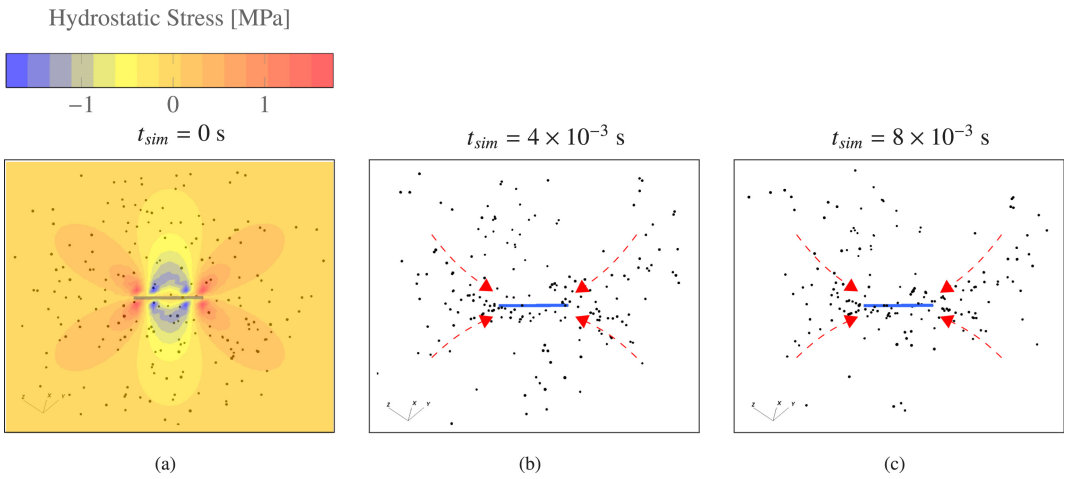

Figure 3.13: Snapshots of vacancy positions for a $20b$ immobilized interstitial loop from $t_{sim} = 0$ s to $t_{sim} = 8 \times 10^{-3}$ s. Images with a viewing angle along the habit plane.

3.3 Discussion

3.3.1 General summary of the method

The two main objectives of the present work can be summarized as follows:

1. The first is a 'numerical' objective that aims at augmenting the capabilities of parallel DDD approaches (the `ParaDiS` code in particular) by introducing a recently-developed discrete point-defect kMC module capturing vacancy diffusion in the presence of arbitrary dislocation structures. Thus, our approach is an additional step towards incorporating more complex physics within the parallel DDD framework [111], as a way to extend its range of applicability and its ability to be meaningfully connected to and calibrated against lower-scale approaches [112].

2. The second objective is 'physical' in nature, namely to demonstrate that, when applied to realistic scenarios (enabled by the numerical implementation of the method in the DDD code), discrete defect kinetics coupled to dislocation network subevolution lead to fluctuations in the vacancy event occurrences and their spatial distribution that have a crucial impact on the

system's evolution. Such considerations are merely absent from continuum methods for climb in which vacancies are represented as a smooth, continuous concentration field.

With the completion of these two objectives, we have implemented the original method developed by McElfresh *et al.* [50] into a massively parallel code platform that will allow us to explore vacancy-dislocation interactions on scales representative of real microstructures. By the same token, the implementation opens the door to non-traditional applications for large-scale DDD codes such as `ParaDiS`. We will discuss these in more depth below.

3.3.2 Comparison of discrete versus continuum vacancy-dislocation methods

It is of interest to cross-compare the present method of kMC/DDD with generic continuum treatments of elasto-diffusion, such as those discussed in C.1. From a qualitative perspective, results presented in Section 3.2 show a markedly different behavior in the evolution of the dislocation structures between both approaches. Not surprisingly, the kMC/DDD approach leads to rougher dislocation line configurations, which is a direct consequence of the discrete nature of absorption and emission events and the highly localized associated climb. The presence of these line features (i.e., jogs) which are not captured in continuum methods may have important consequences on the subsequent glide mobility of the dislocations.

From a quantitative perspective, here again significant differences are observed even for the relatively simple cases involving prismatic loops examined in this work. As best illustrated in Figure 3.10, we find that the discrete method systematically predicts average climb velocities that are several orders of magnitude lower than predictions from the continuum approaches under the same conditions. While other simulation methods may ultimately be required, it is nevertheless important to pinpoint key differences between the approaches that could explain such quantitative differences in climb velocities. One of the major differences is that continuum-based approaches rely on the assumption that the vacancy concentra-

tion is always at equilibrium with the dislocation network, i.e. that the vacancies respond instantly to the network evolution while the bulk provides an infinite and instantaneous supply of vacancies to maintain the global concentration at its equilibrium value. In contrast, the discrete approach explicitly accounts for the finite-speed diffusion of the vacancies, which must migrate through the bulk before being absorbed at the dislocation cores. As well, often times in real situations, dislocation line configurations and vacancy distributions change too fast for equilibrium even to be established. Discrete changes in line shape immediately result in a new stress distribution around the affected segments, which changes altogether the equilibrium conditions relative to other parts of the system. In those cases, a steady state may be established -understood as an average behavior taken over many local out-of-equilibrium situations, an effect which continuum methods fail to capture as well. As a result the kinetic of the defect-dislocation co-evolution is likely to be much slower than when assuming instantaneous equilibrium, which is consistent with our observations. The discrete nature of the kMC/DDD approach also allows our model to capture more subtle behaviors associated with spatially resolved discrete point defects, such as the fact that several vacancies may compete for absorption by the same dislocation segment, which may also tend to reduce the average climb velocity.

Finally, a list comparing the main features of each class of methods is provided in Table 3.2. The features perceived to be advantageous in either case (from the point of view of the findings in this work) are highlighted in red.

Table 3.2: Relation of features of defect-dislocation co-evolution methods. The features perceived to be advantageous in either case (from the point of view of the findings in this work) are highlighted in red.

Feature	Continuum	Discrete
Homogeneous defect diffusion	Yes	Yes
Fluctuations in defect concentrations	No	Yes
Fluctuations in climb dynamics	No	Yes
Treatment of emission/absorption	continuous	discrete events
Dislocation climb solver	Yes (with FEM)	Yes (stochastic)
Parallel scalable	Yes	Yes
Numerical stiffness	No	Yes [50]

3.4 Conclusion

In this work we have introduced a parallel kinetic Monte Carlo method for dislocation climb based on discretized defect diffusion coupled with discrete dislocation dynamics. The method explicitly incorporates point defects as discrete particles co-evolving in a complex dislocation network environment, whereby the local dislocation-induced stress fields dictate the vacancy diffusion while emission and absorption events are treated as discrete events governed by detailed reaction rates. We developed a global, parallel kMC time-stepping method that unifies timesteps associated with the multi-stepped dislocation dynamics and the vacancy kMC modules in a consistent fashion while maintaining the physicality of the simulations. By examining several relevant test cases of the concurrent evolution of vacancies and prismatic dislocation loop configurations, we found that our discrete approach yields markedly slower climb velocity predictions compared to existing continuum-based approaches, suggesting a strong sensitivity of the dislocation/vacancy climb kinetics to the underlying spatial distribution of the vacancy population.

C.1 Brief description of existing climb models

C.1.1 Analytical solution : Climb via balancing vacancy flux

The classical vacancy flux field $\boldsymbol{J}$ associated with a vacancy concentration c is given by Fick's first law:

$$\boldsymbol{J} = -D_v \nabla c \ , \tag{C.14}$$

where D_v is the vacancy diffusion coefficient and ∇ is the gradient operator. The time-dependent vacancy concentration can then be determined using Fick's second law:

$$\frac{\partial c(r,t)}{\partial t} = \nabla \cdot \boldsymbol{J} \ , \tag{C.15}$$

where $c(r,t)$ is the vacancy concentration field. We assume that dislocations climb slowly compared to diffusion so there is always enough time to equilibrate the local

vacancy concentration such that $\partial c/\partial t = 0$. As a result, it holds that:

$$\Delta c = 0 \ , \tag{C.16}$$

where Δ is the Laplacian. We can then consider a cylindrical tube around a straight dislocation segment with an inner radius r_d that is approximately the size of the dislocation core region and an outer radius r_∞ that is large enough to be assumed to represent the bulk [25]. These assumptions lead to the vacancy concentration boundary conditions:

$$c(r_\infty) = c_\infty \ , \tag{C.17}$$

$$c_d = c_0 e^{F_{cl}\Omega_a/bkT} \ , \tag{C.18}$$

where c_0 is the equilibrium vacancy concentration, F_{cl} is the mechanical climb force, Ω_a is the atomic volume, b is the Burgers vector magnitude, T is the temperature, and k is Boltzmann's constant. The analytical solution of eq. (C.16) that satisfies the boundary conditions is

$$c_r = c_\infty + \frac{c_\infty - c_d}{\ln\left(r_\infty/r_d\right)} \ln\left(\frac{r}{r_\infty}\right) \ . \tag{C.19}$$

The climb velocity for a single straight edge dislocation can then be obtained by assuming that each segment is a perfect vacancy sink and there is no pipe diffusion:

$$v_{cl} = \frac{2\pi D_v}{b \ln\left(r_\infty/r_d\right)} \left(c_\infty - c_o e^{-F_{cl}\Omega_a/bkT}\right) \ . \tag{C.20}$$

The climb velocity is accessible once the vacancy flux into each segment's cylindrical volume has been appropriately solved for. Further explanation of this approach is detailed in refs. [25] and [49]. This formulation is of course only valid for infinite straight dislocations, a limitation which served as a motivating factor for the development of the Green's function approach to handle arbitrary dislocation configurations [26].

C.1.2 Green's function formulation

A brief description of the vacancy-coupled climb solution proposed by Gu *et al.* is provided here. The authors refer the reader to work outlined in refs. [15, 26] for

further detail. The Green's function formulation originates from a similar treatment of a dislocation as a vacancy source or sink coupled with climb in an infinite medium, in which the time-dependent vacancy concentration can be described as:

$$\frac{\partial c}{\partial t} = D_v \Delta c - h\delta(\Gamma) \ , \tag{C.21}$$

where the climb parameter h corresponds to the product bv_{cl}, $\delta(\Gamma)$ is the Dirac delta function, and Γ represents all dislocation segments in the system. Boundary conditions can be set by assuming a fixed vacancy concentration at an infinite distance in the bulk and slow climb relative to diffusion (i.e., $\partial c/\partial t = 0$), resulting in:

$$D_v \Delta c = h\delta(\Gamma) \ , \tag{C.22}$$

$$c(r_\infty, t) = c_\infty \ . \tag{C.23}$$

It is then assumed that the vacancy concentration remains constant across all emission and absorption fluxes in the system (i.e., vacancies are not created or destroyed). This can be demonstrated by integrating eq. (C.21) across the entire simulation volume V:

$$\frac{d}{dt}\int_V c\, dV = D_v \int_{\partial V} \frac{\partial c}{\partial n} dS - \int_\Gamma h dl = 0 \ , \tag{C.24}$$

where the right hand side of the expression originates from the inclusion of eq. (C.22). The application of Green's function formalism provides the solution to the eq. (C.22) boundary value problem as:

$$c(x,y,z) = -\frac{1}{4\pi D_v}\int_\Gamma \frac{h(x_1,y_1,z_1)}{\sqrt{(x-x_1)^2+(y-y_1)^2+(z-z_1)^2}} dl + c_\infty \ . \tag{C.25}$$

To further simplify the solution, it is assumed that the local vacancy distribution at the tube of radius r_d satisfies local conditions consistent with eq. (C.18) and a cutoff angle is employed that considers screw and near-screw effects, resulting in an integral equation for all points along a dislocation:

$$-\frac{1}{4\pi D_v}\int_\Gamma \frac{h(x_1,y_1,z_1)}{\sqrt{(x-x_1)^2+(y-y_1)^2+(z-z_1)^2+r_d^2}} dl + c_\infty = c_0 e^{g\Omega_a/bkT}|_{x,y,z} \ , \tag{C.26}$$

where g is the mechanical climb force that considers the dislocation character. The expression can be solved numerically for the segment climb velocity by evaluating the right-hand side of the equation with respect to each DDD node and expressing the left-hand side as a function of the climb velocity, using a quadrature formula [15]. This gives a final system of equations as:

$$\sum_{j=1}^{N} \alpha_{ij} h^j = 4\pi D_v \left(c_\infty - c_o e^{-g^i \Omega_a / kT} \right) \ , \tag{C.27}$$

where α_{ij} is a matrix of quadrature coefficients that depends on the nodes positions. Ultimately, climb velocity for all segments can be extracted by first solving the system of equations laid out in eq. (C.27) for each segment's h value and then compensating for dislocation character, $v_{cl} = h/b_e$, where b_e is the edge component of the Burgers vector.

C.2 Additional model validation data

C.2.1 Effect of temperature on null event ratio

Figure C.14 shows the null event ratio as a function of simulation time for four different simulation temperatures. All simulations begin with a transitory period during which segments emit vacancies to equilibrate their local volumes with the equilibrium vacancy concentration. The null event ratio then stabilizes to a value that is inversely dependent on temperature. The reason behind this inverse temperature dependence is that at higher temperatures, there are more vacancies in the simulations (C_0 increases exponentially with T). As such, the fluctuations in the number of vacancies in a given subdomain (as a result of inter-domain diffusion) are smaller, which does not result in large imbalances in vacancy count across subdomains.

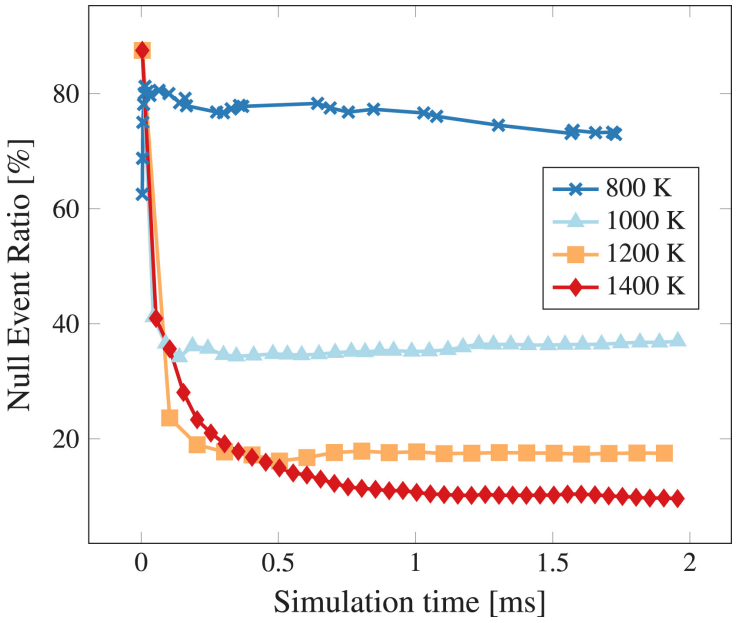

Figure C.14: The cumulative average frequency of null-rate events for a simulation with a single 50b loop and 8 subdomains.

C.2.2 Evolution of the vacancy population across parallel domains

Figure C.15 shows a series of plots illustrating the evolution of R_t^{vac} from each subdomain as simulations progress (left column of plots), and the normalized vacancy concentration of each subdomain as a function of time (right column). Consistent with Figure C.14, increasing the temperature clearly results in smaller relative fluctuations in R_t^{vac} across subdomains, leading also to a decrease in the null event ratio. It is useful to note that in this study the subdomain volumes are fixed and identical for all processors.

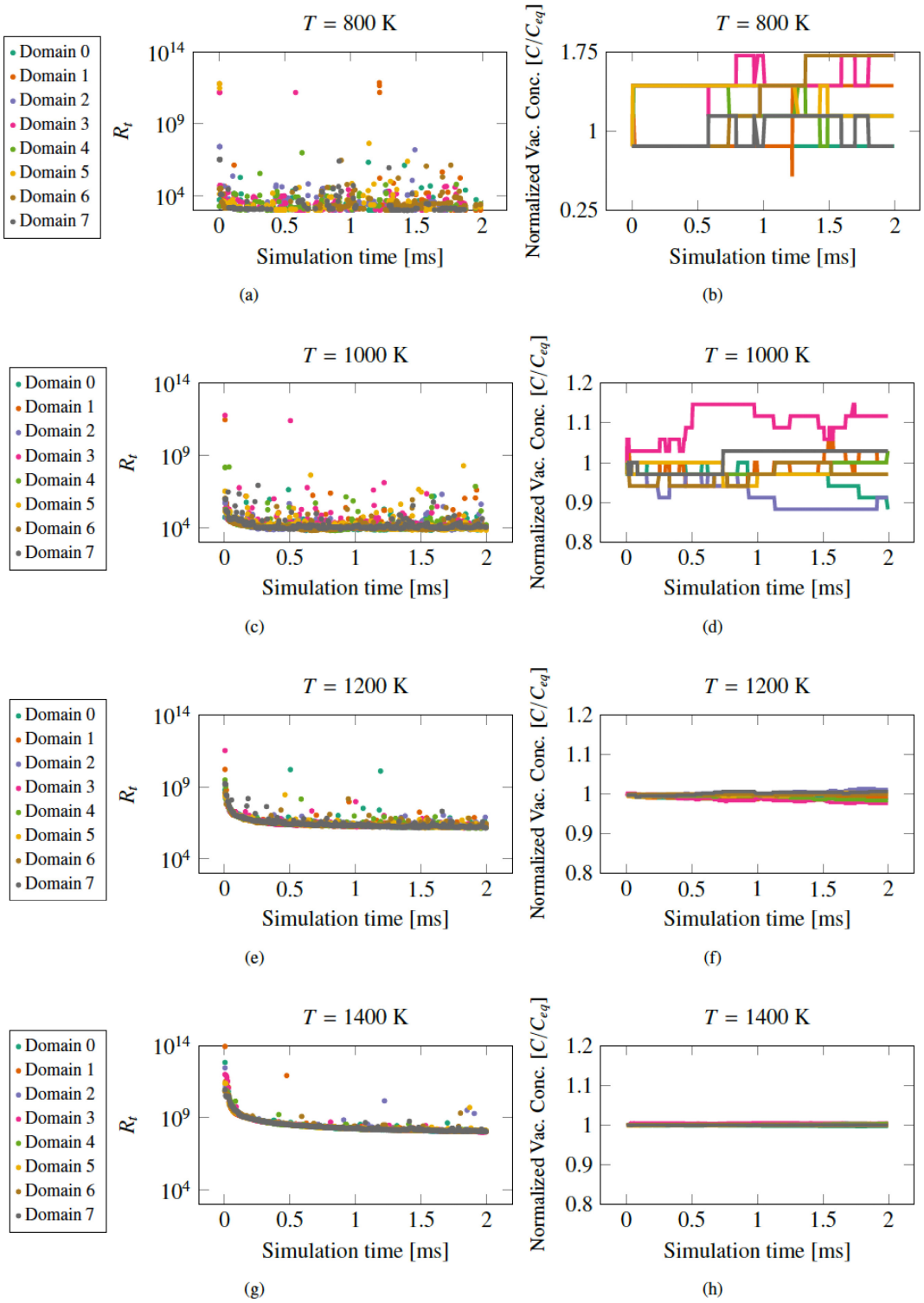

Figure C.15: The total rate (R_t) and normalized vacancy concenrtation in each subdomain as a function of simulation time at 800 K (a) (b), 1000 K (c) (d), 1200 K (e) (f), and 1400 K (g) (h). The inter-domain variation in R_t decreases with temperature which agrees with the correlation of null rate frequency and temperature shown in Figure C.14.

C.2.3 Additional scalability data

Additional details of the scalability test for a configuration made of 200 loops of $200b$ diameter and 10,000 vacancies are provided here. The system was simulated for 100 iterations during which we recorded the execution time of the different processes of the DDD and vacancy modules. The total and normalized computation times of each of the processes are shown in Figure C.16(a) and C.16(b), respectively. Figure C.16(c) shows the percentage time allocation between the DDD code and vacancy code. For this system we find that the communication processes in `ParaDiS` take up an increasingly large portion of the total computation time as the number of processors are increased. Within the DDD communication processes the most costly functionalities were found to be the dispatch of the nodal velocities and ghost nodes. Ghost nodes are dislocation nodes that are not native to a subprocessor's physical domain but are in its immediate surrounding domains. The `ParaDiS` DDD code overall takes up an increasingly large portion of the total computation time, increasing from 35% with the serial implementation to to 90% when using 288 processors. The normalized computational cost of the subprocesses in the vacancy code are shown in Figure C.16(d). Within the vacancy code, the rate calculation is the most computationally intensive process due to the querying of the local stress gradient using `ParaDiS`'s native stress calculation functions. The calculation of the local stress gradient consumes roughly 90%-99% of the processes time. These results indicate that in large-scale simulations the scalability of the coupled kMC/DDD approach is likely to be limited by the scalability of the DDD module.

The strong scaling behavior of the combined kMC/DDD module as implemented in this study is also provided for completeness. For this, two simulation sizes were examined in serial and with then with 2 to 52 processors in parallel. Case #1 consisted of 3000 vacancies and 128 loops and case #2 consisted of 9000 vacancies and 200 loops. All loops were $200b$ in size and contained in a $200b \times 200b \times 200b$ volume. The speedup as a function of the number of processors is plotted in Figure C.17. The speedup deteriorated rapidly after 52 processors for this magnitude of problem size.

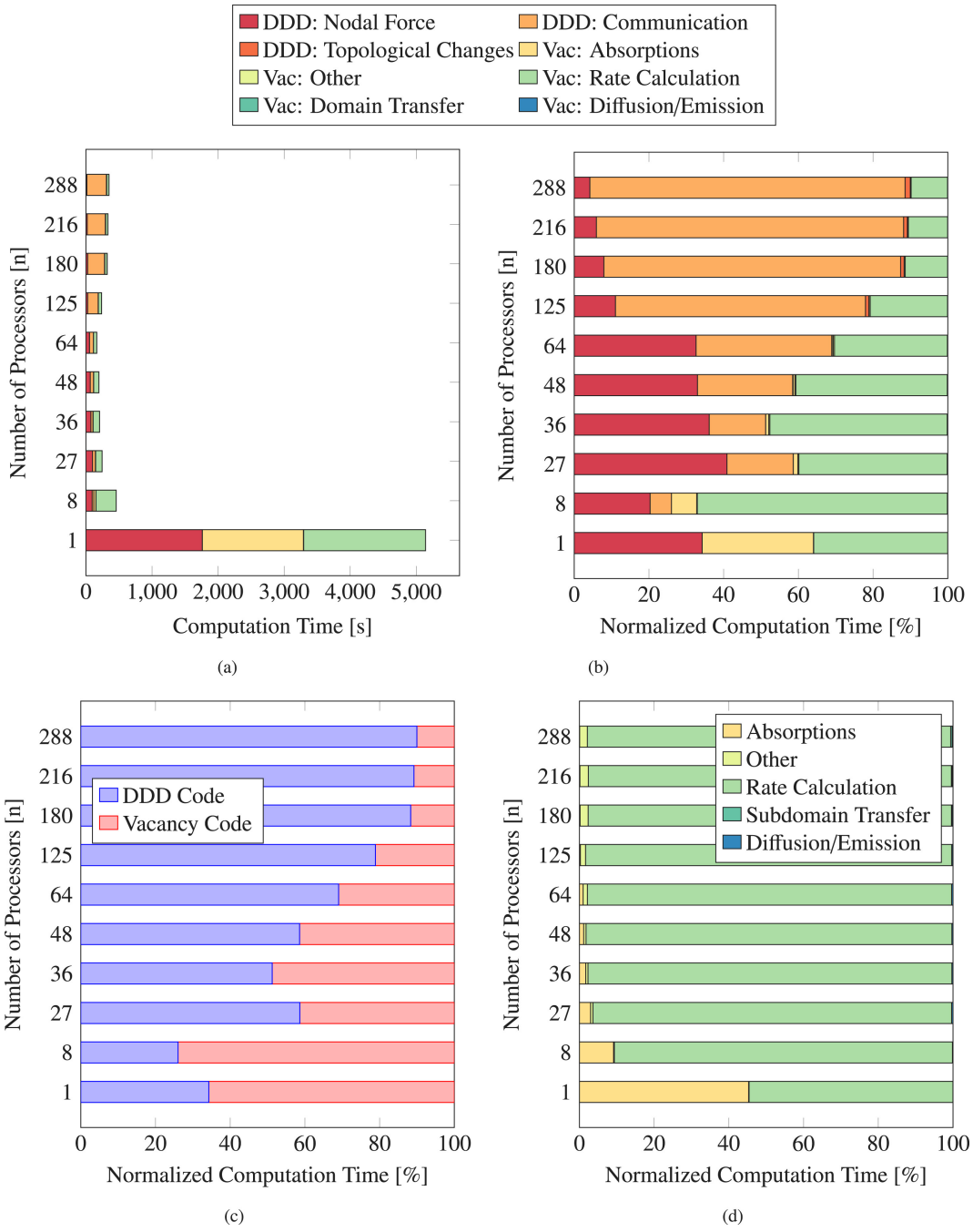

Figure C.16: (a) Total computation time for all vacancy and DDD processes. (b) Normalized computation time for all DDD and vacancy module processes. (c) Percentage of total computation time between the DDD and vacancy related code. (d) Normalized computation time for the subprocesses in the vacancy code only.

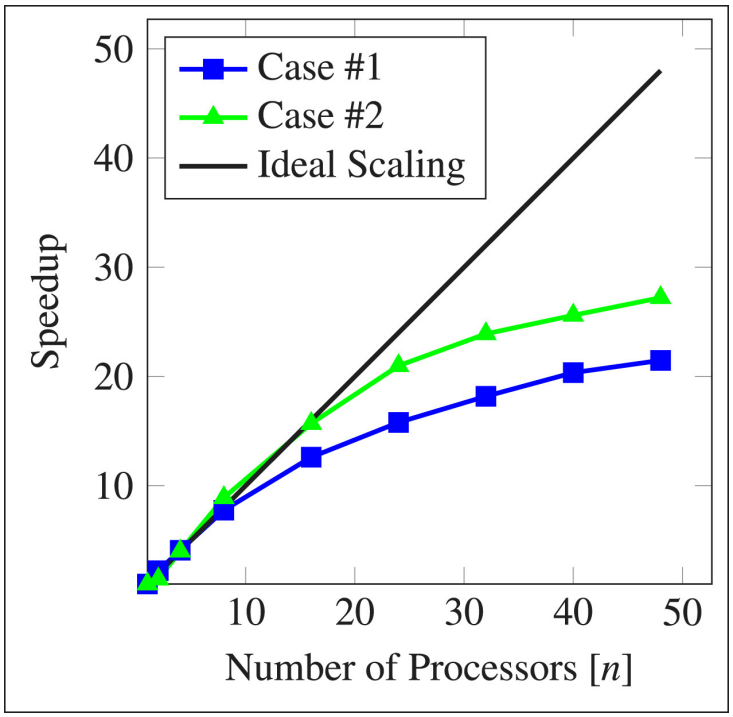

Figure C.17: Speedup of the vacancy module as a function of the number of processors for a fixed simulation cubic volume of $200b$ in size. Case #1 contains 3000 vacancies and 128 dislocation loops while case #2 contains 9000 vacancies and 200 dislocation loops. All loops were of size $200b$. The temperature was set to 1200 K. δt_{DDD} was set to 10^{-3} s to ensure that the that we were primarily probing the vacancy module.

Chapter 4

Coalescence dynamics of prismatic dislocation loops due to vacancy supersaturation

4.1 Theory and Models

In the following examples, we simulate Mo single crystals defined by the material parameters listed in Table 4.1. To avoid numerical incompatibilities associated

Table 4.1: Material parameters for Mo used in the present simulations [3, 4].

Parameter	Symbol	Units	Value
Lattice parameter	a_0	nm	0.317
Atomic density	ρ_a	m^{-3}	6.45×10^{28}
Atomic volume	Ω_a	b^3	0.77
Relaxation volume	Ω_{rel}	Ω_a	-0.37
Vac formation energy	H_f	eV	3.0
Vac migration energy	E_m^0	eV	1.6
Attempt frequency	ν_0	Hz	10^{12}
Burgers vector	b	nm	0.27

with merging deterministic (DD) and stochastic (kMC) integration algorithms, we cast the entire elasto-plastic-diffusive problem within a single stochastic framework, taking advantage of a parallel kMC algorithm to evolve the system as a single event-driven process. The coupled model has been implemented into the

massively-parallel `ParaDiS` code [99–101] using a synchronous parallel kMC algorithm [78, 107].

4.2 Results: vacancy ring formation

Our first finding of significance is that vacancies flowing into a hexagonal prismatic loop[1] do not get immediately absorbed but instead become trapped at an offset distance from the dislocation segments. This is illustrated in Figure 4.1, which shows three instantaneous time snapshots (at $t = 0$, 40, and 80 ms) of the interaction between vacancies and a $40b$ hexagonal dislocation loop at 1400 K in thermal conditions (no vacancy supersaturation).

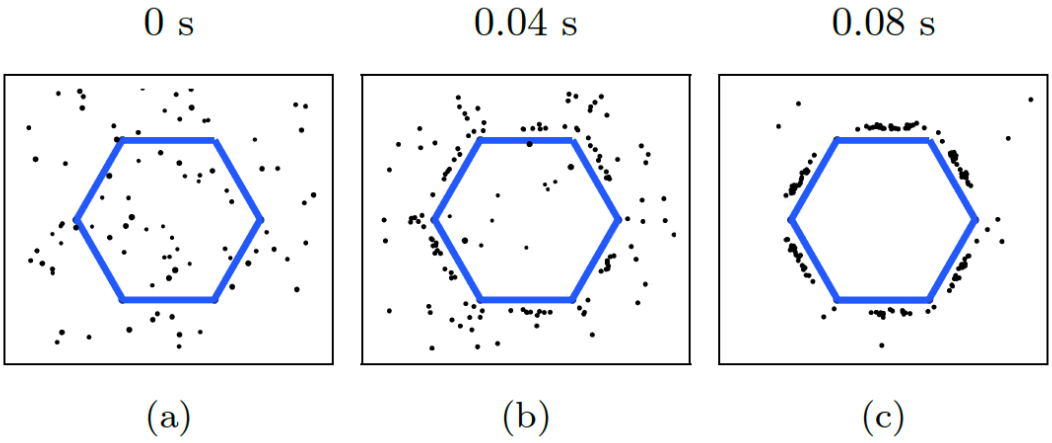

Figure 4.1: Snapshots of vacancy clusters forming around an immobilized vacancy prismatic loop with a core width of $4b$. The simulation was performed with a $40b$ loop at 1400 K.

As the figure shows, vacancies are seen to form a ring outside the loop's perimeter, eventually clustering along the edges of the hexagon. Indeed, inspection of the radial stress field of the loop reveals the existence of a barrier against point defect absorption at an offset distance from the loop segments. This barrier is an intrinsic feature of the stress field of an isolated prismatic loop, and is shown in

[1] In bcc metals, prismatic loops adopt a hexagonal shape whose edges are oriented along ⟨112⟩ directions [113].

Figure 4.2 by a continuous black line. The near-core local hydrostatic stress minima exist as a result of the use of the non-singular elasticity theory in the DD implementation employed here [114]. More details on this implementation can be found in refs. [34, 114, 115]. It is important to note that this type of structure is not fully-relaxed because our method does not capture inelastic effects such as vacancy clustering and/or interactions with dislocation cores that might disrupt it and take it towards more stable configurations. Thus, it is more appropriate to refer to these trapped clusters as being in a transient configuration that may not be representative of the ground state of the loops.

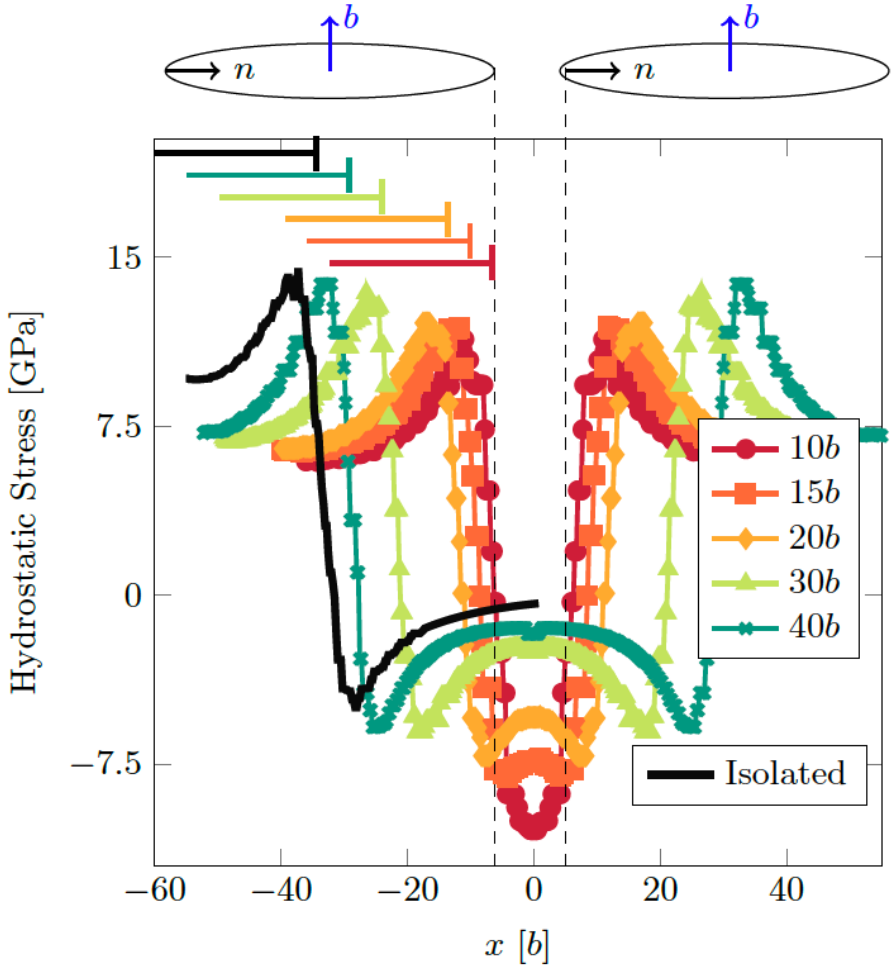

Figure 4.2: Hydrostatic stress as a function of x-coordinate between two $40b$-diameter vacancy loops at various loop separations. The $x = 0$ value corresponds to the midpoint between the loops' closest points. The two loops drawn above the figure correspond to a separation of $10b$. Also shown overlaid in black is the hydrostatic stress profile of an isolated loop.

Additionally, we have discovered that, rather than approaching the loop from outside the glide cylinder [2], vacancies are funneled through the inner boundaries of the compressive stress cone created by the loop, thereby avoiding encountering the barrier altogether. This is shown in Figure 4.4, which includes three snapshots of the spatial distribution of thermal vacancies around a stationary $40b$-diameter

[2]The *glide cylinder* or *glide prism* is the quadric surface created by extending each of the loop's edges (or the entire perimeter in the case of a circular loop) to infinity along the Burgers vector's direction.

loop at 1400 K, where the color map indicates the value of Tr($\boldsymbol{\sigma}$)) in GPa. In this fashion, vacancies can become trapped without having to overcome the stress barrier for the isolated loop shown in Figure 4.2. Indeed, vacancies are accelerated into the loop's perimeter due to the extremely-high pressure gradient indicated in the figure. Climb is thus made feasible only after vacancies are able to escape this trap, which is itself and thermally activated process. For completeness, similar evidence of vacancy clustering behavior on the inside of interstitial prismatic loops is provided in the Figure 4.3.

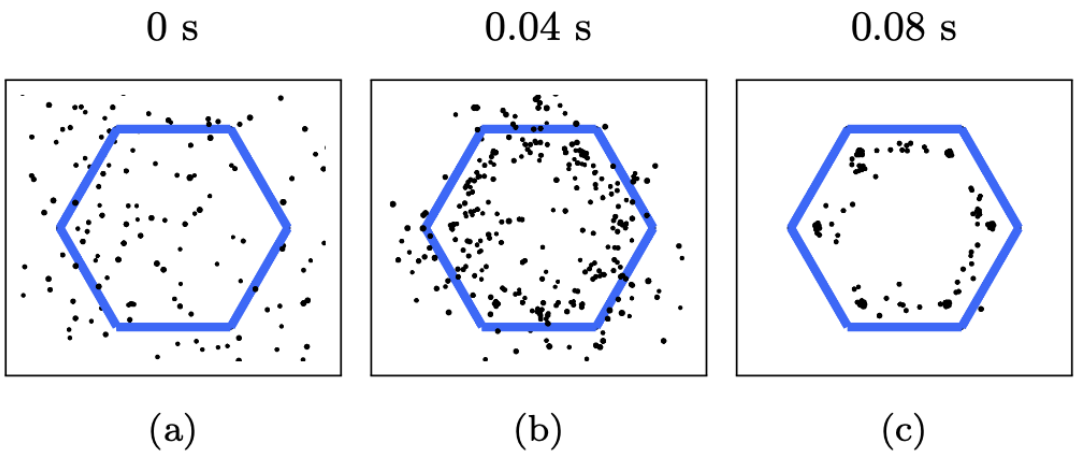

Figure 4.3: Snapshots of vacancy clusters forming around an immobilized interstitial prismatic loop with a core width of 4b. The simulation was performed with a 40b loop at 1400 K.

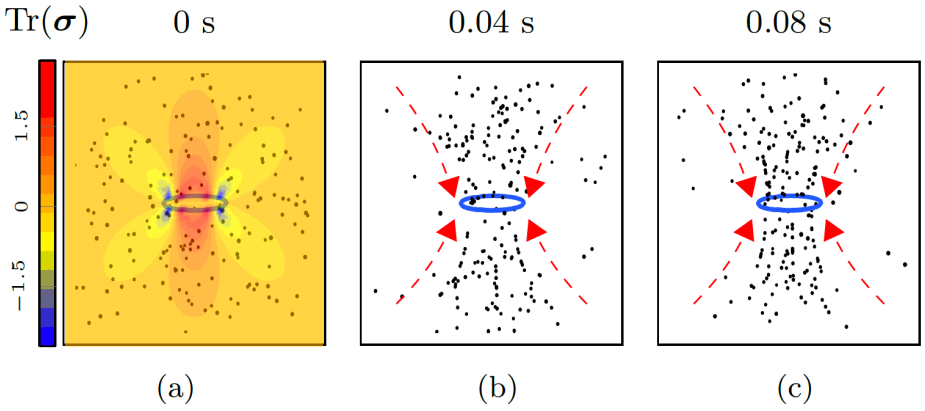

Figure 4.4: Kinetic evolution of the vacancies around a 40b-diameter loop at 1400 K. The initial vacancy distribution is shown in (a). The color bar indicates the value of Tr($\boldsymbol{\sigma}$) in GPa. The vacancies approach the loop in the fashion indicated by the red arrows in (b) and (c), i.e., following the inner boundaries of the compressive stress lobes created by the loop.

4.3 Results: loop coalescence mechanism

The stress profile shown in Figure 4.2 substantiates the behavior observed in Figure 4.1, i.e., that vacancies can arrange themselves into a ring outside an isolated loop's perimeter. As mentioned earlier, this actually hinders climb, as vacancies are thermodynamically trapped at an offset distance from the actual loop segments. However, when two prismatic dislocation loops approach one another, whether by climb or glide, the situation drastically changes. As Figure 4.2 illustrates for a pair of 40b-diameter circular loops, the two stress minima corresponding to the two isolated defects gradually merge with one another, giving rise to a single combined pressure minimum. Most importantly, however, this joint minimum results in an abundance of vacancies trapped in the gap between the loops. Figure 4.2 shows the shape of the pressure profile at various distances between the two defects. As the loops approach, the shared stress minimum deepens as it is sandwiched between the opposing segments. The stress gradient associated with such process is seen to increase as well, leading to a strong driving force for vacancy agglomeration in that region, as illustrated in Figure 4.5. Furthermore, we have seen that an

enhanced accumulation of vacancies in the common interaction zone intensifies the attractive force between the loops, resulting in coalescence even in conditions where both glide and climb are required to bring the process to completion.

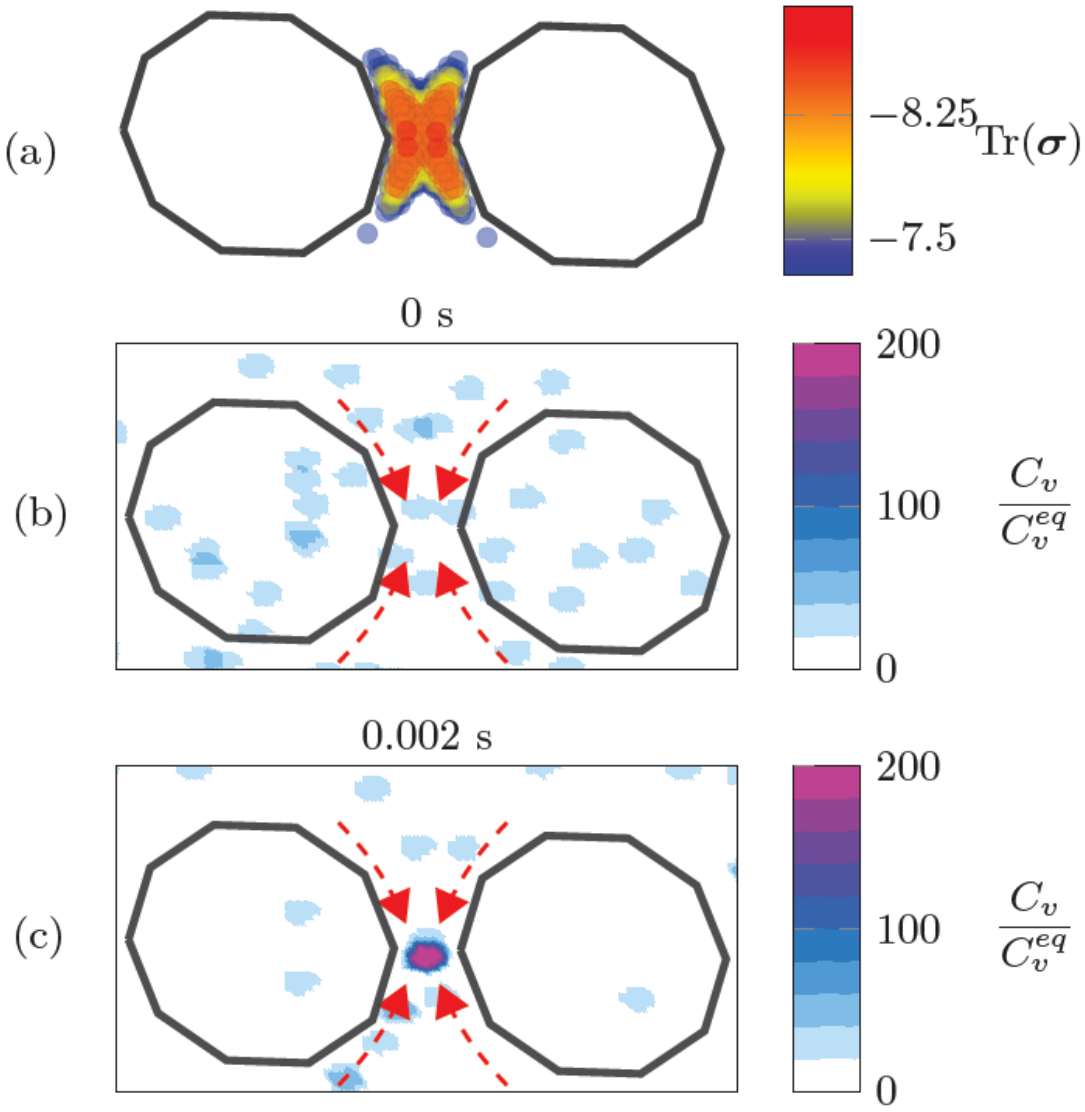

Figure 4.5: (a) Hydrostatic stress map for two 60b-diameter vacancy loops separated by 10b. The color bar indicates the value of Tr($\boldsymbol{\sigma}$) in GPa. Local vacancy concentration at (b) $t = 0$ and (c) 0.002 s. Red dashed arrows mark the vacancy approach path to the pressure trap shared between the loops.

The coalescence process is studied in the simulations presented in Figure 4.6,

where two elongated interstitial loops with non-overlapping glide cylinders are placed at an offset distance of $10b$ from one another. While the loops here are simulated with Fe as the base material for direct comparison to experimental results of irradiated Fe in ref. [2], we expect the simulated behavior to be qualitative the same in other bcc metals. The relevant physical parameters that were used for Fe were $a_0 = 0.286$ nm, $H_f = 1.7$ eV, $E_m^0 = 0.68$ eV, $b = 0.25$ nm, $\Omega_a = 0.80b^3$, and $\Omega_{\text{rel}} = -0.2$. The offset separation, d_v, is along the 'vertical' direction in the figure and is overcome by glide, while the glide cylinders are brought into contact by climb along the 'horizontal' direction, d_h. We then let the loops evolve under no external applied stress and we track d_v and d_h. The results are shown in Figure 4.6(a) where both distances are seen to decrease monotonically to zero. The angle θ representing the ratio of the glide and climb distances (as $\theta = \tan^{-1}(d_h/d_v)$) is also included in the figure. The process is eminently elastic, as demonstrated by the good agreement between our time-dependent evolution and Kroupa's expression to describe climb-mediated annihilation of two pure edge dislocations [116]:

$$\frac{1}{2}\left(\frac{h}{bK}\right)^2 \approx \frac{1}{2}\left(\frac{h_0}{bK}\right)^2 - \frac{2D_v c_j}{b^2 K}t \tag{4.1}$$

where h is the dipole width (here equivalent to d_h), K is a temperature-dependent material parameter, c_j is the density of jogs on the dislocation, t is time, and h_0 is the initial climb offset at $t = 0$. As the figure shows, the offset angle remains practically constant during the coalescence process.

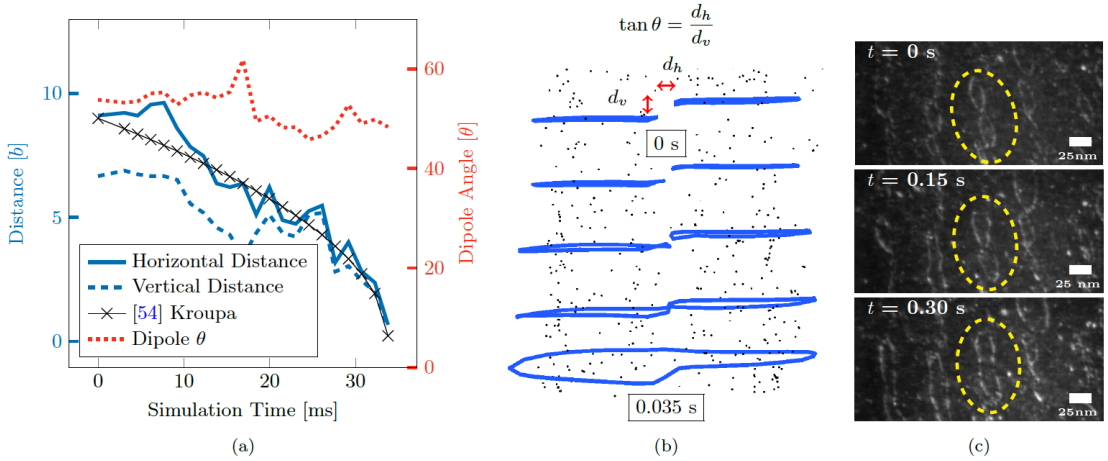

Figure 4.6: (a) Horizontal (in blue, solid) and vertical separation (in blue, dashed) between an interstitial prismatic loop dipole and the corresponding dipole angle (in red, dotted, right axis) as a function of simulation time. The dipole angle remains relatively constant as the loops climb and glide towards one another and eventually annihilate the dipole. (b) Snapshots of the interstitial loop dipole shrinking and eventually coalescing under combined climb-glide mechanics. (c) Coalescence process of two irradiation loops in pure Fe at 300°C (from ref. [2], reproduced with permission). 25 nm equals approximately $100b$ in Fe.

Figure 4.6(b) shows several snapshots of the coalescence simulations. The loops expand via climb while also gliding towards one another to bridge the separation d_v. However, climb outpaces glide and in the end a jog of magnitude $\approx d_v$ is left in the coalesced structure. The simulated process is remarkably similar to *in situ* transmission electron microscopy (TEM) observations of prismatic loop coalescence in irradiated Fe at 300°C [2], as displayed in Figure 4.6(a). While the origin of the loops differs, once formed the kinetics of coalescence seen in the experiments matches what our simulations predict. This is a very encouraging sign that adds confidence to our models. Additionally, we note that the loop configuration in Figure 4.6(b) was constructed as an arbitrary dipole but allowed to evolve freely. Both the kinetics and final configuration may strongly depend on the type of multiloop metastable configuration that the dislocations adopt, but a detailed examination is reserved for future work [117].

4.4 Summary

Our first finding of significance is the existence of a stress minimum around a prismatic loop that can create an elastic trap for point defects at an offset distance on the order of 2-5b from the actual loop segments. This trap is located outside the perimeter for vacancy loops (inside for self-interstitial loops). While a sizable kinetic barrier exists to access this minimum when approaching the loop from its habit plane, we find that vacancies take advantage of a 'cone' of favorable (compressive) stress gradients to approach the loops and become trapped there. The significance of this is that, for isolated loops, vacancies are not immediately absorbed by the dislocation segments, which is the common assumption to formulate osmotic forces that balance prismatic loops against climb. A more detailed investigation of the influence of vacancy cluster formation and inelastic interactions between the vacancies and dislocation cores is needed to capture the ultimate fate of these structures, but is presently beyond the scope of this paper.

Second, we find that in a coalescence process between two prismatic loops belonging to non-overlapping glide cylinders, the stress traps belonging to each loop merge and intensify. This actually favors climb, as a relatively large concentration of vacancies is funneled to that region, creating extra chemical force for absorption. Coalescence is thus directly driven by elastic forces that bring the loops in line via glide, and indirectly through climb (chemical) forces that expand their glide cylinders until contact is established and coalescence takes place. We find a remarkable qualitative agreement with *in situ* TEM observations of similar processes in irradiated Fe. None of these effects can be practically studied via direct atomistic simulations –as the configurational space and the relevant timescales are simply far too large to be explored rigorously–, or with continuum methods because they fail to capture the fine details of the interactions between point defects and dislocation segments, including fluctuations.

Chapter 5

Future Work

Though this method was originally developed for modeling vacancies, the framework developed can be easily generalized to explore other point defect phenomena that are difficult to capture with continuum solutions. As formulated and implemented, the method provides a great deal of flexibility. For instance, a first order approach to model self-interstitial atoms (SIA) kinetics would be to simply adjust the defect parameters D_v, E_m, Ω_{rel} and capture radius accordingly. Since SIA are known to display peculiar migration behavior, however, such as non-isotropic diffusivity and being sensitive to trigonal stresses, some physics adjustments would be needed in order to correctly formulate the diffusion-drift equation and the defect-dislocation interaction criteria (emission, absorption, pinning, etc.). Pipe diffusion could similarly be explored through careful treatment of the degrees of freedom of the defects near segments. Though the physics of the point defect transport and interaction may change, the underlying backbone of the parallelized defect-coupled dislocation dynamics model would remain similar.

As well, the extension of the method to substitutional solute-dislocation effects is attainable through some slight modifications in the treatment of the diffusion behavior and defect-dislocation relationships. Most notably, by the addition of a pinning and de-pinning mechanic for gliding dislocation segments as they become locked by solute atoms. A similar kMC method was demonstrated by Zhao *et al.* [118], however, by applying the developed kMC/DDD framework here we would immediately have access large-scale simulations of complex dislocation networks.

Such modifications would enable the study of solute hardening and dynamic strain ageing, for example.

Another interesting application of the framework would be the inclusion of multi-atom formation mechanics for bi-,and tri-vacancy or interstitial clusters. The formation and dissolution of multi-atom clusters has been explored using first-principle techniques [91,119–121] and the representative energetic parameters, $E_f^{V_1+V_1->V_2}$ and $E_f^{V_2->V_1+V_1}$ for instance, could serve as additional actions that vacancies/interstitials could taken given close proximity to a like atom. Moreover, the multi-vacancy/interstitial clusters have modified migration energies that can be applied from first-principle investigations [119].

Finally, one could physically describe the evolution of defect populations during irradiation damage in the presence of realistic dislocation microstructures. Damage introduced during irradiation via collision cascades is known to result in high concentrations of point defects distributed in a highly heterogeneous way, which invalidates continuum methods for their study.

Bibliography

[1] B. Bakó, E. Clouet, L. M. Dupuy, M. Blétry, Dislocation Dynamics Simulations with Climb: Kinetics of Dislocation Loop Coarsening Controlled by Bulk Diffusion, Philosophical Magazine 91 (23) (2011) 3173–3191.

[2] M. Hernández-Mayoral, Z. Yao, M. Jenkins, M. Kirk, Heavy-ion irradiations of fe and fe–cr model alloys part 2: Damage evolution in thin-foils at higher doses, Philosophical Magazine 88 (21) (2008) 2881–2897.

[3] P.-W. Ma, S. Dudarev, Effect of stress on vacancy formation and migration in body-centered-cubic metals, Physical Review Materials 3 (6) (2019) 063601.

[4] P.-W. Ma, S. Dudarev, Universality of point defect structure in body-centered cubic metals, Physical Review Materials 3 (1) (2019) 013605.

[5] J. Weertman, Theory of steady-state creep based on dislocation climb, Journal of Applied Physics 26 (10) (1955) 1213–1217.

[6] U. Messerschmidt, A model of the temperature dependent part of stage i work-hardening due to jog-dragging (i), physica status solidi (b) 41 (2) (1970) 549–563.

[7] F. A. Mohamed, T. G. Langdon, The transition from dislocation climb to viscous glide in creep of solid solution alloys, Acta metallurgica 22 (6) (1974) 779–788.

[8] H. Strunk, R. Frydman, Jog dragging in edge dislocations with application to plastic deformation and internal friction, Materials Science and Engineering 18 (1) (1975) 143–148.

[9] L. K. Mansur, Irradiation creep by climb-enabled glide of dislocations resulting from preferred absorption of point defects, Philosophical Magazine A 39 (4) (1979) 497–506.

[10] S. I. Hong, Influence of dynamic strain aging on the dislocation substructure in a uniaxial tension test, Materials Science and Engineering 79 (1) (1986) 1–7.

[11] F. Louchet, B. Viguier, Ordinary dislocations in γ-tial: cusp unzipping, jog dragging and stress anomaly, Philosophical Magazine A 80 (4) (2000) 765–779.

[12] J. Marian, W. Cai, V. V. Bulatov, Dynamic transitions from smooth to rough to twinning in dislocation motion, Nature materials 3 (3) (2004) 158.

[13] A. Stukowski, D. Cereceda, T. D. Swinburne, J. Marian, Thermally-activated non-schmid glide of screw dislocations in w using atomistically-informed kinetic monte carlo simulations, International Journal of Plasticity 65 (2015) 108–130.

[14] R. Bullough, M. Hayns, Irradiation-creep due to point defect absorption, Journal of Nuclear Materials 57 (3) (1975) 348–352.

[15] I. Rovelli, S. Dudarev, A. Sutton, Non-local Model for Diffusion-mediated Dislocation Climb and Cavity Growth, Journal of the Mechanics and Physics of Solids 103 (2017) 121–141.

[16] I. Rovelli, S. Dudarev, A. Sutton, Statistical Model for Diffusion-mediated Recovery of Dislocation and Point-defect Microstructure, Physical Review E 98 (4) (2018) 043002.

[17] R. Bullough, T. Quigley, Dislocation sink strengths for the rate theory of irradiation damage, Journal of Nuclear Materials 104 (1981) 1397–1401.

[18] R. Stoller, Modeling dislocation evolution in irradiated alloys, Metallurgical Transactions A 21 (7) (1990) 1829–1837.

[19] J. Wang, R. G. Hoagland, A. Misra, Room-temperature dislocation climb in metallic interfaces, Applied Physics Letters 94 (13) (2009) 131910.

[20] M. Kabir, T. T. Lau, D. Rodney, S. Yip, K. J. Van Vliet, Predicting Dislocation Climb and Creep from Explicit Atomistic Details, Physical Review Letters 105 (9) (2010) 095501.

[21] A. Sivak, V. Chernov, V. Romanov, P. Sivak, Kinetic monte-carlo simulation of self-point defect diffusion in dislocation elastic fields in bcc iron and vanadium, Journal of Nuclear Materials 417 (1-3) (2011) 1067–1070.

[22] J. Lothe, J. P. Hirth, Dislocation climb forces, Journal of Applied Physics 38 (2) (1967) 845–848.

[23] M. Turunen, A general equation of motion for dislocation climb, Acta Metallurgica 24 (5) (1976) 463–467.

[24] D. Raabe, On the consideration of climb in discrete dislocation dynamics, Philosophical Magazine A 77 (3) (1998) 751–759. arXiv:https://doi.org/10.1080/01418619808224081, doi:10.1080/01418619808224081.
URL https://doi.org/10.1080/01418619808224081

[25] D. Mordehai, E. Clouet, M. Fivel, M. Verdier, Introducing Dislocation Climb by Bulk Diffusion in Discrete Dislocation Dynamics, Philosophical Magazine 88 (6) (2008) 899–925.

[26] Y. Gu, Y. Xiang, S. S. Quek, D. J. Srolovitz, Three-dimensional Formulation of Dislocation Climb, Journal of the Mechanics and Physics of Solids 83 (2015) 319–337.

[27] D. Thompson, E. Tarleton, S. Roberts, S. Fitzgerald, Interstitial-mediated dislocation climb and the weakening of particle-reinforced alloys under irradiation, Physical Review Materials 2 (8) (2018) 080601.

[28] F. Fischer, J. Svoboda, Chemically and mechanically driven creep due to generation and annihilation of vacancies with non-ideal sources and sinks, International journal of plasticity 27 (9) (2011) 1384–1390.

[29] S. M. Keralavarma, T. Cagin, A. Arsenlis, A. A. Benzerga, Power-law Creep From Discrete Dislocation Dynamics, Physical Review Letters 109 (26) (2012) 265504.

[30] K. M. Davoudi, L. Nicola, J. J. Vlassak, Dislocation climb in two-dimensional discrete dislocation dynamics, Journal of Applied Physics 111 (10) (2012) 103522. arXiv:https://doi.org/10.1063/1.4718432, doi:10.1063/1.4718432.
URL https://doi.org/10.1063/1.4718432

[31] M. Rajaguru, S. Keralavarma, A Discrete Dislocation Dynamics Model of Creeping Single Crystals, Modelling and Simulation in Materials Science and Engineering 26 (3) (2018) 035007.

[32] F. Liu, A. C. Cocks, E. Tarleton, A new method to model dislocation self-climb dominated by core diffusion, Journal of the Mechanics and Physics of Solids (2019) 103783.

[33] W. Cai, V. V. Bulatov, Mobility laws in dislocation dynamics simulations, Materials Science and Engineering: A 387 (2004) 277–281.

[34] A. Arsenlis, W. Cai, M. Tang, M. Rhee, T. Oppelstrup, G. Hommes, T. G. Pierce, V. V. Bulatov, Enabling Strain Hardening Simulations with Dislocation Dynamics, Modelling and Simulation in Materials Science and Engineering 15 (6) (2007) 553.

[35] S. H. Haghighat, G. Eggeler, D. Raabe, Effect of climb on dislocation mechanisms and creep rates in γ?-strengthened ni base superalloy single crystals: A discrete dislocation dynamics study, Acta Materialia 61 (10) (2013) 3709–3723.

[36] T. Záležák, J. Svoboda, A. Dlouhỳ, High temperature dislocation processes in precipitation hardened crystals investigated by a 3d discrete dislocation dynamics, International Journal of Plasticity 97 (2017) 1–23.

[37] N. Ghoniem, M, S.-H. Tong, L. Sun, Parametric Dislocation Dynamics: A Thermodynamics-based Approach to Investigations of Mesoscopic Plastic Deformation, Physical Review B 61 (2) (2000) 913.

[38] D. Mordehai, E. Clouet, M. Fivel, M. Verdier, Annealing of Dislocation Loops in Dislocation Dynamics Simulations, in: IOP Conference Series: Materials Science and Engineering, Vol. 3, IOP Publishing, 2009, p. 012001.

[39] S. Roy, D. Mordehai, Annihilation of Edge Dislocation Loops via Climb During Nanoindentation, Acta Materialia 127 (2017) 351–358.

[40] D. Mordehai, G. Martin, Enhanced Annealing of the Dislocation Network Under Irradiation, Physical Review B 84 (1) (2011) 014115.

[41] S. Gao, M. Fivel, A. Ma, A. Hartmaier, 3D Discrete Dislocation Dynamics Study of Creep Behavior in Ni-base Single Crystal Superalloys by a Combined Dislocation Climb and Vacancy Diffusion Model, Journal of the Mechanics and Physics of Solids 102 (2017) 209–223.

[42] X. Niu, T. Luo, J. Lu, Y. Xiang, Dislocation Climb Models from Atomistic Scheme to Dislocation Dynamics, Journal of the Mechanics and Physics of Solids 99 (2017) 242–258.

[43] X. Niu, Y. Gu, Y. Xiang, Dislocation Dynamics Formulation for Self-climb of Dislocation Loops by Vacancy Pipe Diffusion, International Journal of Plasticity 120 (2019) 262–277.

[44] F. Liu, A. C. Cocks, E. Tarleton, A New Method to Model Dislocation Self-climb Dominated by Core Diffusion, Journal of the Mechanics and Physics of Solids 135 (2020) 103783.

[45] F. Liu, A. C. Cocks, S. P. Gill, E. Tarleton, An Improved Method to Model Dislocation Self-climb, Modelling and Simulation in Materials Science and Engineering 28 (5) (2020) 055012.

[46] A. Breidi, S. Dudarev, Dislocation Dynamics Simulation of Thermal Annealing of a Dislocation Loop Microstructure, Journal of Nuclear Materials (2022) 153552.

[47] A. Peeva, R. Kögler, W. Skorupa, J. S. Christensen, A. Y. Kuznetsov, Spatial Distribution of Cavities in Silicon Formed by Ion Implantation Generated Excess Vacancies, Journal of Applied Physics 95 (9) (2004) 4738–4741.

[48] K. Arakawa, M. Kiritani, Spatial Distribution of Nucleation of Point Defect Clusters in Irradiated Metals, Journal of Nuclear Materials 239 (1996) 1–6.

[49] J. P. Hirth, J. Lothe, T. Mura, Theory of Dislocations, Journal of Applied Mechanics 50 (2) (1983) 476.

[50] C. McElfresh, Y. Cui, S. L. Dudarev, G. Po, J. Marian, Discrete Stochastic Model of Point Defect-dislocation Interaction for Simulating Dislocation Climb, International Journal of Plasticity 136 (2021) 102848.

[51] G. H. Vineyard, Frequency factors and isotope effects in solid state rate processes, Journal of Physics and Chemistry of Solids 3 (1) (1957) 121 – 127.

[52] K. J. Laidler, M. C. King, Development of transition-state theory, The Journal of physical chemistry 87 (15) (1983) 2657–2664.

[53] P.-W. Ma, S. L. Dudarev, Effect of stress on vacancy formation and migration in body-centered-cubic metals, Phys. Rev. Materials 3 (2019) 063601. doi:10.1103/PhysRevMaterials.3.063601.
URL https://link.aps.org/doi/10.1103/PhysRevMaterials.3.063601

[54] P.-W. Ma, S. L. Dudarev, Universality of point defect structure in body-centered cubic metals, Phys. Rev. Materials 3 (2019) 013605. doi:10.1103/PhysRevMaterials.3.013605.
URL https://link.aps.org/doi/10.1103/PhysRevMaterials.3.013605

[55] B. Puchala, M. L. Falk, K. Garikipati, Elastic effects on relaxation volume tensor calculations, Phys. Rev. B 77 (2008) 174116. doi:10.1103/PhysRevB.77.174116.
URL https://journals.aps.org/prb/abstract/10.1103/PhysRevB.77.174116

[56] Y. Kraftmakher, Equilibrium vacancies and thermophysical properties of metals, Phys. Reports 299 (1998) 79–188.

[57] J. P. Hirth, J. Lothe, Theory of Dislocations, Krieger, Malabar, Florida, 1992.

[58] W. Hertz, W. Waidelich, H. Peisl, Lattice contraction due to quenching in vacancies in platinum and gold, Physics Letters A 43 (1973) 289–290.

[59] S. L. Dudarev, D. R. Mason, E. Tarleton, P.-W. Ma, A. E. Sand, A multi-scale model for stresses, strains and swelling of reactor components under irradiation, Nuclear Fusion 58 (2018) 126002. doi:10.1088/1741-4326/aadb48.
URL https://doi.org/10.1088/1741-4326/aadb48

[60] L. Landau, E. M. Lifshits, Theory of Elasticity, Pergamon Press, Oxford, England, 1970.

[61] P. Heald, M. Speight, Point defect behaviour in irradiated materials, Acta Metallurgica 23 (11) (1975) 1389–1399.

[62] R. Bullough, R. Newman, The kinetics of migration of point defects to dislocations, Reports on progress in physics 33 (1) (1970) 101.

[63] P. Dederichs, K. Schroeder, Anisotropic diffusion in stress fields, Physical Review B 17 (6) (1978) 2524.

[64] E. A. Codling, M. J. Plank, S. Benhamou, Random walk models in biology, Journal of the Royal Society Interface 5 (25) (2008) 813–834.

[65] G. Blaj, C. Kenney, J. Segal, G. Haller, Analytical solutions of transient drift-diffusion in pn junction pixel sensors, arXiv preprint arXiv:1706.01429 (2017).

[66] G. Leibfried, N. Breuer, Point Defects in Metals I: Introduction to the Theory, Springer-Verlag, Berlin, 1978.

[67] J. Friedel, M. Yoshida, On dislocation jogs as sources and sinks of vacancies, The Philosophical Magazine: A Journal of Theoretical Experimental and Applied Physics 31 (1) (1975) 229–231.

[68] R. Johnson, Interstitials and vacancies in α iron, Physical Review 134 (5A) (1964) A1329.

[69] S. Kim, W. Buyers, Vacancy formation energy in iron by positron annihilation, Journal of Physics F: Metal Physics 8 (5) (1978) L103.

[70] P. Söderlind, L. Yang, J. A. Moriarty, J. Wills, First-principles formation energies of monovacancies in bcc transition metals, Physical Review B 61 (4) (2000) 2579.

[71] C. Domain, C. Becquart, Ab initio calculations of defects in fe and dilute fe-cu alloys, Physical Review B 65 (2) (2001) 024103.

[72] M. Mendelev, S. Han, D. Srolovitz, G. Ackland, D. Sun, M. Asta, Development of new interatomic potentials appropriate for crystalline and liquid iron, Philosophical magazine 83 (35) (2003) 3977–3994.

[73] J. Marian, B. Wirth, G. Odette, J. Perlado, Cu diffusion in α-fe: determination of solute diffusivities using atomic-scale simulations, Computational materials science 31 (3-4) (2004) 347–367.

[74] C.-C. Fu, J. Dalla Torre, F. Willaime, J.-L. Bocquet, A. Barbu, Multiscale modelling of defect kinetics in irradiated iron, Nature materials 4 (1) (2005) 68.

[75] A. Souidi, C. S. Becquart, C. Domain, D. Terentyev, L. Malerba, A. Calder, D. Bacon, R. Stoller, Y. N. Osetsky, M. Hou, Dependence of radiation damage accumulation in iron on underlying models of displacement cascades and subsequent defect migration, Journal of nuclear materials 355 (1-3) (2006) 89–103.

[76] C. C. Fu, F. Willaime, First principles calculations in iron: structure and mobility of defect clusters and defect complexes for kinetic modelling, Comptes Rendus Physique 9 (3-4) (2008) 335–342.

[77] M. Snyder, A. Chatterjee, D. Vlachos, Net-event kinetic monte carlo for overcoming stiffness in spatially homogeneous and distributed systems, Computers & Chemical Engineering 29 (4) (2005) 701 – 712.

[78] E. Martínez, J. Marian, M. H. Kalos, J. M. Perlado, Synchronous Parallel kinetic Monte Carlo for Continuum Diffusion-reaction Systems, Journal of Computational Physics 227 (8) (2008) 3804–3823.

[79] M. Núñez, D. Vlachos, Steady state likelihood ratio sensitivity analysis for stiff kinetic monte carlo simulations, The Journal of chemical physics 142 (4) (2015) 044108.

[80] A. Savara, J. E. Sutton, Sqert-t: alleviating kinetic monte carlo (kmc)-stiffness in transient kmc simulations, Journal of Physics: Condensed Matter 30 (29) (2018) 295901.

[81] M. Gilbert, S. Queyreau, J. Marian, Stress and temperature dependence of screw dislocation mobility in α-fe by molecular dynamics, Physical Review B 84 (17) (2011) 174103.

[82] S. Queyreau, J. Marian, M. Gilbert, B. Wirth, Edge dislocation mobilities in bcc fe obtained by molecular dynamics, Physical Review B 84 (6) (2011) 064106.

[83] I. Ringdalen, S. Wenner, J. Friis, J. Marian, Dislocation dynamics study of precipitate hardening in al–mg–si alloys with input from experimental characterization, MRS Communications 7 (3) (2017) 626–633.

[84] N. Ghoniem, S. Tong, J. Huang, B. Singh, M. Wen, Mechanisms of dislocation-defect interactions in irradiated metals investigated by computer simulations, Journal of nuclear materials 307 (2002) 843–851.

[85] D. L. Olmsted, R. Phillips, W. Curtin, Modelling diffusion in crystals under high internal stress gradients, Modelling and Simulation in Materials Science and Engineering 12 (5) (2004) 781.

[86] H.-S. Nam, D. J. Srolovitz, Molecular dynamics simulation of ga penetration along grain boundaries in al: A dislocation climb mechanism, Physical review letters 99 (2) (2007) 025501.

[87] G. Love, Dislocation pipe diffusion, Acta Metallurgica 12 (6) (1964) 731–737.

[88] J. Mimkes, Pipe diffusion along isolated dislocations, Thin Solid Films 25 (1) (1975) 221–230.

[89] K. Miller, K. Ingle, A. Crocker, A computer simulation study of pipe diffusion in body centred cubic metals, Acta Metallurgica 29 (9) (1981) 1599–1606.

[90] Y. Gao, Z. Zhuang, Z. Liu, X. You, X. Zhao, Z. Zhang, Investigations of pipe-diffusion-based dislocation climb by discrete dislocation dynamics, International journal of plasticity 27 (7) (2011) 1055–1071.

[91] Y. N. Osetsky, D. Bacon, A. Serra, B. Singh, S. Golubov, Stability and mobility of defect clusters and dislocation loops in metals, Journal of nuclear materials 276 (1-3) (2000) 65–77.

[92] M. Kiritani, Similarity and difference between fcc, bcc and hcp metals from the view point of point defect cluster formation, Journal of nuclear materials 276 (1-3) (2000) 41–49.

[93] S. J. Zinkle, Y. Matsukawa, Observation and analysis of defect cluster production and interactions with dislocations, Journal of nuclear materials 329 (2004) 88–96.

[94] M. J. Turunen, V. K. Lindroos, Edge dislocation velocity in stress-induced climb, The Philosophical Magazine: A Journal of Theoretical Experimental and Applied Physics 27 (1) (1973) 81–86.

[95] W. D. Nix, R. Gasca-Neri, J. P. Hirth, A contribution to the theory of dislocation climb, The Philosophical Magazine: A Journal of Theoretical Experimental and Applied Physics 23 (186) (1971) 1339–1349.

[96] Z. Zhuang, Z. Liu, Y. Cui, Chapter 12 - glide-climb coupling model and temperature effect on microscale crystal plasticity,

in: Z. Zhuang, Z. Liu, Y. Cui (Eds.), Dislocation Mechanism-Based Crystal Plasticity, Academic Press, 2019, pp. 331 – 380. doi:https://doi.org/10.1016/B978-0-12-814591-3.00012-1.
URL http://www.sciencedirect.com/science/article/pii/B9780128145913000121

[97] E. Golder, J. Settle, The box-müller method for generating pseudo-random normal deviates, Journal of the Royal Statistical Society: Series C (Applied Statistics) 25 (1) (1976) 12–20.

[98] J. Friedbl, M. Yoshida, On Dislocation Jogs as Sources and Sinks of Vacancies, Philosophical Magazine 31 (1) (1975) 229–231.

[99] V. Bulatov, W. Cai, J. Fier, M. Hiratani, G. Hommes, T. Pierce, M. Tang, M. Rhee, K. Yates, T. Arsenlis, Scalable Line Dynamics in ParaDiS, in: SC'04: Proceedings of the 2004 ACM/IEEE Conference on Supercomputing, IEEE, 2004, pp. 19–19.

[100] Z. Wang, N. Ghoniem, S. Swaminarayan, R. LeSar, A Parallel Algorithm for 3D Dislocation Dynamics, Journal of Computational Physics 219 (2) (2006) 608–621.

[101] W. Cai, V. V. Bulatov, T. G. Pierce, M. Hiratani, M. Rhee, M. Bartelt, M. Tang, Massively-parallel Dislocation Dynamics Simulations, in: IUTAM Symposium on Mesoscopic Dynamics of Fracture Process and Materials Strength, Springer, 2004, pp. 1–11.

[102] A. M. Hussein, S. I. Rao, M. D. Uchic, D. M. Dimiduk, J. A. El-Awady, Microstructurally Based Cross-slip Mechanisms and their Effects on Dislocation Microstructure Evolution in FCC Crystals, Acta Materialia 85 (2015) 180–190.

[103] S. Rao, C. Woodward, B. Akdim, E. Antillon, T. Parthasarathy, J. El-Awady, D. Dimiduk, Large-scale Dislocation Dynamics Simulations of Strain Hardening of Ni Microcrystals Under Tensile Loading, Acta Materialia 164 (2019) 171–183.

[104] R. B. Sills, N. Bertin, A. Aghaei, W. Cai, Dislocation Networks and the Microstructural Origin of Strain Hardening, Physical Review Letters 121 (8) (2018) 085501.

[105] R. Friedberg, J. E. Cameron, Test of the Monte Carlo Method: Fast Simulation of a Small Ising Lattice, The Journal of Chemical Physics 52 (12) (1970) 6049–6058.

[106] R. H. Swendsen, J.-S. Wang, Replica Monte Carlo Simulation of Spin-glasses, Physical review letters 57 (21) (1986) 2607.

[107] E. Martínez, P. R. Monasterio, J. Marian, Billion-atom Synchronous Parallel kinetic Monte Carlo Simulations of Critical 3D Ising Systems, Journal of Computational Physics 230 (4) (2011) 1359–1369.

[108] R. B. Sills, A. Aghaei, W. Cai, Advanced Time Integration Algorithms for Dislocation Dynamics Simulations of Work Hardening, Modelling and Simulation in Materials Science and Engineering 24 (4) (2016) 045019.

[109] R. B. Sills, W. P. Kuykendall, A. Aghaei, W. Cai, Fundamentals of Dislocation Dynamics Simulations, in: Multiscale materials modeling for nanomechanics, Springer, 2016, pp. 53–87.

[110] Y. Gu, Dislocation Climb in Discrete Dislocation Dynamics and Its Applications, Hong Kong University of Science and Technology (Hong Kong), 2016.

[111] R. B. Sills, S. Aubry, Line Dislocation Dynamics Simulations with Complex Physics, Handbook of Materials Modeling: Methods: Theory and Modeling (2020) 1559–1581.

[112] N. Bertin, R. B. Sills, W. Cai, Frontiers in the Simulation of Dislocations, Annual Review of Materials Research 50 (2020) 437–464.

[113] J. Marian, B. Wirth, R. Schäublin, J. Perlado, T. D. de la Rubia, ¡ 100¿-loop characterization in α-fe: comparison between experiments and modeling, Journal of nuclear materials 307 (2002) 871–875.

[114] W. Cai, A. Arsenlis, C. R. Weinberger, V. V. Bulatov, A non-singular continuum theory of dislocations, Journal of the Mechanics and Physics of Solids 54 (3) (2006) 561–587.

[115] E. Martinez, J. Marian, A. Arsenlis, M. Victoria, J. M. Perlado, Atomistically informed dislocation dynamics in fcc crystals, Journal of the Mechanics and Physics of Solids 56 (3) (2008) 869–895.

[116] F. Kroupa, Annihilation of a dislocation dipole, Czechoslovak Journal of Physics B 17 (3) (1967) 220–226.

[117] Y. Li, M. Boleininger, C. Robertson, L. Dupuy, S. L. Dudarev, Diffusion and interaction of prismatic dislocation loops simulated by stochastic discrete dislocation dynamics, Physical Review Materials 3 (7) (2019) 073805.

[118] Y. Zhao, L. Dezerald, M. Pozuelo, X. Zhou, J. Marian, Simulating the mechanisms of serrated flow in interstitial alloys with atomic resolution over diffusive timescales, Nature communications 11 (1) (2020) 1–8.

[119] K. Heinola, F. Djurabekova, T. Ahlgren, On the stability and mobility of di-vacancies in tungsten, Nuclear Fusion 58 (2) (2017) 026004.

[120] B. Uberuaga, R. Hoagland, A. Voter, S. Valone, Direct transformation of vacancy voids to stacking fault tetrahedra, Physical review letters 99 (13) (2007) 135501.

[121] H. Wang, D. Rodney, D. Xu, R. Yang, P. Veyssiere, Pentavacancy as the key nucleus for vacancy clustering in aluminum, Physical Review B 84 (22) (2011) 220103.